INFORMATION TO USERS

This manuscript has been reproduced from the microfilm master. UMI films the text directly from the original or copy submitted. Thus, some thesis and dissertation copies are in typewriter face, while others may be from any type of computer printer.

The quality of this reproduction is dependent upon the quality of the copy submitted. Broken or indistinct print, colored or poor quality illustrations and photographs, print bleedthrough, substandard margins, and improper alignment can adversely affect reproduction.

In the unlikely event that the author did not send UMI a complete manuscript and there are missing pages, these will be noted. Also, if unauthorized copyright material had to be removed, a note will indicate the deletion.

Oversize materials (e.g., maps, drawings, charts) are reproduced by sectioning the original, beginning at the upper left-hand corner and continuing from left to right in equal sections with small overlaps. Each original is also photographed in one exposure and is included in reduced form at the back of the book.

Photographs included in the original manuscript have been reproduced xerographically in this copy. Higher quality 6" x 9" black and white photographic prints are available for any photographs or illustrations appearing in this copy for an additional charge. Contact UMI directly to order.

UMI

A Bell & Howell Information Company
300 North Zeeb Road, Ann Arbor MI 48106-1346 USA
313/761-4700 800/521-0600

Université d'Ottawa · University of Ottawa

MILLIMETER-WAVE NOISE CHARACTERIZATION OF PHEMT DEVICES

by

Paul Béland, B.A.Sc.

A thesis submitted to the

School of Graduate Studies and Research

In partial fulfillment of the requirements for the degree of

Master of Applied Science

in Electrical and Computer Engineering

Ottawa-Carleton Institute for Electrical and Computer Engineering

School of Information Technology and Engineering (Electrical & Computer Engineering)

Faculty of Engineering
University of Ottawa

July, 1997

© 1997, Paul Béland, Ottawa, Canada

National Library of Canada

Acquisitions and Bibliographic Services

395 Wellington Street
Ottawa ON K1A 0N4
Canada

Bibliothèque nationale du Canada

Acquisitions et services bibliographiques

395, rue Wellington
Ottawa ON K1A 0N4
Canada

Your file Votre référence

Our file Notre référence

The author has granted a non-exclusive licence allowing the National Library of Canada to reproduce, loan, distribute or sell copies of this thesis in microform, paper or electronic formats.

L'auteur a accordé une licence non exclusive permettant à la Bibliothèque nationale du Canada de reproduire, prêter, distribuer ou vendre des copies de cette thèse sous la forme de microfiche/film, de reproduction sur papier ou sur format électronique.

The author retains ownership of the copyright in this thesis. Neither the thesis nor substantial extracts from it may be printed or otherwise reproduced without the author's permission.

L'auteur conserve la propriété du droit d'auteur qui protège cette thèse. Ni la thèse ni des extraits substantiels de celle-ci ne doivent être imprimés ou autrement reproduits sans son autorisation.

0-612-26300-2

ABSTRACT

The theoretical background of thermal noise representation in two-port networks is presented. From this theory, the existing measurement techniques to characterize the noise of pseudomorphic high electron mobility transistors (PHEMTs) at millimeter-wave frequencies are described. The techniques are applied to the now popular on-wafer measurement. A novel on-wafer resistive noise source (ORNS) which provides noise measurement capability at all frequencies from a single calibrated frequency is presented. Demonstration of the noise source capability is made by comparing the measurement of receiver noise figure and two-port noise parameter extraction with those of a coaxial noise source. A custom design of an on-wafer probing station featuring an adapter to directly connect an automated mechanical tuner to the on-wafer probe, and featuring double input and output probes, is evaluated for measurement of noise parameters from 26 to 40 GHz. The results obtained with two 150 μm parallel finger PHEMTs are presented and compared with the general trend of noise models and measurement on an independent system at 26 GHz. Uncertainty analysis is performed for the measurements made at 30 GHz using a commercial microwave computer aided design (CAD) software.

ACKNOWLEDGMENT

All my gratitude to my thesis supervisors, Dr. S. Labonté and Dr. L. Roy, who provided me with beneficial advice, supervision, and encouragement at all stages of this thesis. A very sincere thank you to the Communications Research Center team for a most enjoyable working environment and in particular to Dr. M. Stubbs, H. Do-ky, C. Glaser, B. Clark, and C. Verver, for their time and patience in answering my numerous questions. I am also grateful to Dr. A. Boudiaf , Dr R. Mieirer, Dr. C. Tsironis, and D. Dubouil for their support with regard to noise parameter measurement.

To my friend Manon Thériault and to my family, I wish to express my love by dedicating to them this work.

CONTRIBUTIONS OF THIS THESIS

This thesis is an investigation of noise characterization of active devices, using an automated on-wafer technique, at millimeter wave frequencies. Four main contributions to this field of research have been accomplished.

1. The design and demonstration of the first on-wafer system using a mechanical tuner and operating up to 40 GHz.
2. Improvement to the method of S-parameter calibration by the introduction of 2 sets of probes in the measurement setup.
3. The invention of a novel on-wafer resistive noise source which may result in simpler noise characterization.
4. Presentation for the first time of measured on-wafer noise data of a PHEMT device from 26 to 40 GHz.
5. Identification of the most significant sources of uncertainty.

TABLE OF CONTENTS

Abstract ii

Acknowledgement iii

Contributions of this Thesis iv

1. Introduction 1

1.1 General Introduction 1

1.2 Thesis Objectives 2

1.3 Thesis Outline 2

2. Background 4

2.1 Electronic Noise 4

2.1.1 Thermal Noise 5

2.1.2 Quantifying Electronic Noise 6

2.2 Electronic Noise in Linear Two-Port Networks 9

2.2.1 Representation of Noise in Linear Two-Port Networks 10

2.2.2 Noise Signal Computation with Linear Two-Port Networks 12

2.2.3 Relation Between Noise Figure and Two-Port Noise Signals 13

2.3 The Pseudomorphic High Electron Mobility Transistor 15

2.3.1 The PHEMT Device 15

2.3.2 Noise Models for PHEMT Devices 16

2.4 Conclusion 17

3. Measurement Techniques 19

3.1 Noise Figure Measurement of a Two-Port Network 19

3.1.1 The Y-Factor Measurement Technique 19

3.1.2 The Y-Factor Technique at Microwave Frequencies 22

3.2 Noise Parameter Measurement Techniques 23

3.2.1 IRE Standard Technique 23
3.2.2 Noise Parameter Extraction Techniques 24
3.2.3 Selection of the Impedance Constellation 25
3.3 Common Measurement Setup 27
3.3.1.1 Hot/Cold Technique 27
3.3.1.2 Cold Technique 28
3.3.2 Conclusion 31
3.4 On-Wafer Probing 32
3.5 Conclusion 33
4. On-Wafer Resistive Noise Source 35
4.1 Description 35
4.2 Calibration of the ORNS 38
4.2.1 Setup Calibration Procedure 39
4.2.2 Discussion on Measured Temperature for the ORNS 41
4.3 Receiver Noise Figure Measurements 41
4.4 Conclusion 44
5. Development of a Microwave Noise Parameter Measurement Setup 46
5.1 Selection of the Measurement Methodology 46
5.2 Description of the Measurement Setup 47
5.2.1 The Source Impedance Tuning Sub-assembly 48
5.2.2 Custom On-Wafer Probing Station Sub-Assembly 49
5.2.3 Noise Figure Measurement Sub-Assembly 52
5.2.4 S-parameter Measurement Sub-Assembly 54
5.2.5 DC Biasing Circuits 54
5.3 Calibration Procedure 55
5.3.1 Bias Circuit Resistance Measurement 56
5.3.2 Frequency Alignment of VNA and Receiver 56
5.3.3 On-Wafer S-Parameter Calibration 58

5.3.4 The 3-Termination Calibration for Input Block Characterization 58
5.3.5 Receiver Reflection Coefficient Measurement 61
5.3.6 Tuner Calibration 61
5.3.7 DUT S-Parameter Measurement 62
5.3.8 Receiver Calibration 62
5.3.9 DUT Cold Power Measurements 64
5.4 Selection of Source Impedance Constellation **65**
5.5 Conclusion **67**
6. Noise Parameter Measurements 68
6.1 Intermediate Parameters **68**
6.1.1 Bias 69
6.1.2 S-Parameters 69
6.1.3 Noise Power 72
6.2 PHEMT Noise Parameters as a Function of Bias **73**
6.2.1 Method 74
6.2.2 Results for a PHEMT Device at 26 GHz 75
6.2.3 Discussion 75
6.2.4 Conclusion 77
6.3 Noise Parameters as a Function of Frequency **78**
6.3.1 Method 78
6.3.2 Results from 26 to 40 GHz 79
6.3.3 Discussion 80
6.4 Confirmation of Noise Parameters at 26 GHz **82**
6.5 Conclusion **84**
7. Uncertainty Analysis 86
7.1 The Uncertainty Analysis Technique **86**
7.2 Parameters Measured and their Uncertainties **87**
7.2.1 Reflection Coefficients and S-Parameters Uncertainties 87
7.2.2 Noise Power Measurement Uncertainties 89

7.2.3 Temperature Measurements 90

7.3 Calculated Parameter Uncertainties for Noise Parameter Extraction 91

7.3.1 Uncertainty on Input Block S-Parameters 91

7.3.2 Uncertainties on the Coaxial Available Noise Temperature (T_h) 92

7.3.3 Uncertainties Caused by the Noise Source Change of Impedance. 92

7.3.4 Uncertainty on the Gain-Bandwidth Constant (kG_aB) and the (kBG_0) term 95

7.3.5 Uncertainty on Receiver Noise Parameters 96

7.4 Uncertainty Yield Analysis on the DUT Noise Parameters 98

7.4.1 Results for DUT X at Ids=10 mA 98

7.4.2 Theoretical Limit on Noise Parameters. 100

7.4.3 Consideration of the Receiver Linearity 101

7.5 Sensitivity of Selected Parameters on the DUT Noise Parameters 104

7.6 Conclusion 107

8. Conclusion 109

Appendices 111

Bibliography 129

LIST OF FIGURES

Figure 2.1: Thevenin equivalent circuit 7

Figure 2.2: Seperation of a two-port with internal sources into a source free two-port and external input current and voltages sources 10

Figure 2.3: Resistive two-port network 13

Figure 2.4: Noise free two-port network with source impedance 13

Figure 2.5: Noise circles for the resistive network of Figure 2.3 14

Figure 2.6 Typical cross section of a PHEMT 15

Figure 3.1: Noise figure calculation using Y factor [11 p. 11] 20

Figure 3.2: Y factor noise figure measurement set up 22

Figure 3.3 The Cross and O'Callaghan's optimum constellation 26

Figure 3.4: Hot/cold noise figure parameter measurement setup 28

Figure 3.5: Cold power noise parameter measurement technique 30

Figure 3.6 Layout of a 150 um parallel finger PHEMT with TRL transmission line and probing pad 32

Figure 4.1: On-wafer resistive noise source (ORNS)) 35

Figure 4.2 Setup for ORNS calibration 39

Figure 4.3 Receiver noise figure with a)ORNS biased at 103.36 mA b) Coaxial noise source corrected to on-wafer reference plane c) Uncorrected coaxial noise source 43

Figure 4.4 Receiver noise figure with a)ORNS biased at 124.68 mA b) Coaxial noise source corrected to on-wafer reference plane c) Uncorrected coaxial noise source 43

Figure 5.1 Block diagram of the noise parameter measurement setup 48

Figure 5.2 The Source Impedance Tuning Sub-Assembly. 49

Figure 5.3 Custom on-wafer probing station 50

Figure 5.4 Smith Chart Coverage at 40 GHz....................51

Figure 5.5 Block Diagram of the noise figure measurement sub-assembly....................52

Figure 5.6 DC Bias diagram....................54

Figure 5.7 HP346C noise source reflection coefficient in cold state for A) and B) and hot state for C) . A) measurement at the on-wafer reference plane (A-A') with de-embedding of the input block S-parameters found using the 3 termination calibration, B) measurement at the 2.4 mm coaxial reference plane (B-B'), C) measurement at the 2.4 mm coaxial reference plane (B-B')....................60

Figure 6.1 S-parameters from 26 to 40 GHz of DUT Xi and Yi where i is the drain current (Ids) in mA....................71

Figure 6.2 Cold noise power for 314 impedance points at 30 GHz with DUT X biased at Vds=2 V, Ids=10mA....................73

Figure 6.3 Minimum noise figure of DUT Y as a function of drain current....................76

Figure 6.4: NPAR with Coaxial noise source....................80

Figure 6.5: Difference between measured and calculated noise figure for each constellation of 9 source impedances (Γ_{Si}). A coaxial noise source was used here....................80

Figure 6.6: NPAR with ORNS (T_h=550 Kelvin)....................80

Figure 6.7 DUT X and DUT Y Noise Parameter from 18 to 27 GHz....................82

Figure 6.8 Comparaison of noise parameter between the independent system (BX, BY), our measurement (X, Y) at 26 GHz, and our measurement using the DUT S-parameter measured on the independent system (SX, SY)....................84

Figure 7.1 Uncertainty on DUT X Noise Parameters....................99

Figure 7.2 Noise Figure measurement considering a non-linear receiver....................102

LIST OF TABLES

Table 1: ORNS extracted temperature (T_h) for specific DC bias current 41

Table 2 Bias circuit measured resistance....56

Table 3: PHEMT bias conditions. 69

Table 4 Constellation of Source impedance 74

Table 5: TWIN calculated NPAR at 26 GHz....75

Table 6 MMICAD calculated NPAR at 26 GHz using measured terminations for the 3-termination calibration procedure of the input block. 75

Table 7 MMICAD calculated NPAR at 26 GHz using the Hewlett Packard table of standard coefficients for the 3-termination calibration procedure of the input block. 75

Table 8: Calculated parameters from basic measurement....87

Table 9 Uncertainty on input block S-parameters at 30 GHz....91

Table 10 Uncertainty on parameters required to compute the kBG_0 term....96

Table 11 Relative Cold Noise Power associated with a constellation of nine source impedance for receiver calibration at 30 GHz 97

Table 12 Uncertainty on receiver noise parameters at 30 GHz 98

Table 13 Difference between my S-parameter and Dr Boudiaf's for 100

Table 14 Impact of varied parameters on DUT X10 extracted Noise Parameters at 30 GHz. 105

1. Introduction

1.1 General Introduction

Pioneering work on the characterization of electronic noise started after the first World War. 75 years later, the topic is still an active field of research. The area of electronic device noise characterization is critical for the design of sensitive radio receivers operating at high frequency. The impact of this topic on our lives is becoming more significant in the 1990's with society's request for more rapid digital communications wherever people may be. Electronic noise is an important parameter in the design of solutions for this requirement in particular and of any communication system in general. It determines the achievable data rates for specified signal levels and bandwidth. By reducing a radio receiver's generated noise, power requirements are reduced or, conversely communication over longer distances is made possible.

The sensitivity of a radio receiver is determined by its ability to amplify an electronic signal without deteriorating it. Electronic noise is a signal that exists in the receiver and thus is added to all signals being amplified. Hence, small signals can only be amplified without significant deterioration if the noise added by the receiver is much smaller. The requirement for small signal amplification is critical in radio astronomy, satellite communications, remote sensing, radar, and terrestrial communications systems.

Sensitive radio receivers rely on low-noise amplifiers (LNA) built from semiconductor transistors. The selection of one semiconductor technology over another depends on system requirements. At millimeter-wave frequencies (above 30 GHz), the pseudomorphic high-electron-mobility transistor (PHEMT) is one of the few good candidates, MESFETs and HBTs

being limited to lower frequencies. It is also a relatively young device technology for which the variation of performance may be significant from one manufacturer (foundry) to an other. Variations also exist between different wafers coming out of the same process, and between different transistors laid out on the same wafer. Transistor noise characterization is used to evaluate the quality of devices, to evaluate the performance of semiconductor technologies, to optimize the design and fabrication of devices, and lastly to optimize the design of LNA's. Unfortunately, existing characterization techniques require a significant investment in test equipment, they are fairly complicated, and they are often inaccurate.

The motivation of this thesis is to provide the necessary means to accurately characterize the noise behavior of transistors up to millimeter waves, and to do so while the transistor is still part of the original wafer, i.e. "on-chip" or "on-wafer".

1.2 Thesis Objectives

The main objective of this thesis is to perform on-wafer noise parameter measurements up to 40 GHz. This requires the determination of an appropriate test setup, calibration methodology, choice of parameters to be measured and finally noise parameter extraction technique. It is also desired to perform an uncertainty analysis so as to allow the evaluation of the technique and the identification of its limitations. Since no other measurements between 26 and 40 GHz are available for comparaison, the validity of our results is established by considering an independant characterization at 26 GHz in a different laboratory and by comparing the obtained value to PHEMT noise models.

1.3 Thesis Outline

Chapter 2 of this thesis presents background on thermal noise. We introduce fundamental notions and we briefly discuss statistical representation which leads to the one- and two-port

network representations. The PHEMT device is presented along with some comments about its expected noise behavior.

In Chapter 3, existing measurement techniques are reviewed. Mainly, the Y-factor technique, the hot/cold technique and the cold power technique are explained. The advantages and present limitations of on-wafer probing techniques are also discussed.

In Chapter 4, a novel on-wafer resistive noise source is presented. The benefits of using this type of noise source are discussed and a comparative measurement against a coaxial noise source is made.

In Chapter 5, the on-wafer noise parameter measurement setup developed in this work is presented. Each sub-assembly of the setup is described in detail. The measurement procedure is also explained.

In Chapter 6, the measured noise parameters of two PHEMT devices are presented. Verification of the general trend predicted by models is made. Noise parameter measurements as a function of bias and as a function of frequency are plotted. The measurement of the same devices on an independent system is also presented.

In Chapter 7, the uncertainty analysis of our measurements is presented. A number of assumptions are made to evaluate the uncertainty on the extracted noise parameters at 30 GHz. Verification of these assumptions is done. A sensitivity analysis to evaluate the impact of certain parameters is also presented.

Finally, Chapter 8 summarizes the work done and presents possible directions for future work.

2. Background

The goal of this chapter is to present the theoretical foundation for millimeter-wave noise characterization. We focus on the representation of electronic noise, which is required to measure and characterize the behavior of transistors. We introduce fundamental notions, we briefly discuss statistical representation to make use of one- and two-port network equivalencies, and finally we touch upon PHEMT noise models. Of all the topics covered, the mathematical formulation of noise in two-port networks is the cornerstone of this thesis.

2.1 Electronic Noise

The random internal motion of carriers (electrons or holes) in conducting materials induces a voltage signal that is referred to as electronic noise. Sources of electronic noise in solid-state devices are characterized as low- and high-frequency. Examples of low-frequency sources are flicker noise ($1/f^{\alpha}$), generation-recombination noise (G-R), partition noise [1], and Lorentz noise [2, p.7]. Above 100 MHz, thermal noise generally dominates over the low-frequency noise[1, p.250]. Another significant high-frequency source of noise in field effect transistors (FETs) and high electron mobility transistors (HEMTs) is the channel noise from the conducting channel between the source and the drain [2, p.10], [3], [4]. Shot noise is another type of high-frequency noise, which is most significant in bipolar junction transistors (BJTs) and heterojunction bipolar transistors (HBTs) [1]. One common characteristic of high-frequency noise sources in semiconductor devices is their power spectrum, which can be approximated by a constant between 1 and 100 GHz. This is convenient because we can now describe semiconductor device noise sources as equivalent thermal noise sources.

2.1.1 Thermal Noise

Thermal noise is generated by the random motion of free electrons in a conducting material. Thermal noise causes a noise voltage $e_n(t)$ to be generated between two points of the material. The resulting power spectrum of the noise voltage is [5] [6]:

$$S_e(f) = 2R\left[\frac{h|f|}{2} + \frac{h|f|}{e^{(h|f|/kT_s)} - 1}\right] \quad [V^2 \cdot s] \tag{2.1}$$

where

R [Ω]	is the resistance value of the material,
T_s [K]	is the temperature of the system (or resistor),
$h = 6.624\text{x}10^{-34}$ [J·s]	is Planck's constant,
$k = 1.38\text{x}10^{-23}$ [J·K^{-1}]	is Boltzman's constant.

For $|f| < 1000$ GHz, we have $\left(h|f|/kT_s\right) < 0.15$, and $e^{(h|f|/kT_s)} \approx 1 + h|f|/kT_s$, and therefore (2.1) reduces to:

$$S_e(f) \approx 2RkT_s \quad [V^2 \cdot s]. \tag{2.2}$$

The power spectrum expressed in (2.2) is independent of frequency (f) and is commonly referred to as "white noise". The thermal noise voltage generated in a resistor R [Ω] over a bandwidth B [Hz] is obtained from:

$$\overline{e_n^2(t)} = 4RkT_sB \quad [V^2] \tag{2.3}$$

where $\overline{e_n^2(t)}$ is the mean square thermal voltage. We want to emphasize the fact that the noise voltage signal ($e_n(t)$) is not a periodic signal but rather a random signal. In fact, $e_n(t)$ is stationary (independent of time origin), ergodic (a process which has the same properties whether it is averaged over time on one function or averaged at one time over an ensemble of

functions), and Gaussian (or Normal). Such random processes are totally determined by their mean (μ) and standard deviation (σ) or variance (σ^2) [7]. In the case of thermal electronic noise, we find that $\mu=0$ and $\sigma^2=\overline{e_n^2(t)}$ [8, p.761]. Note that Eq. (2.3) is valid because white noise remains Gaussian after passing through linear filters [9].

2.1.2 Quantifying Electronic Noise

The impact of electronic noise is most significant in the fields of radio astronomy and satellite communications where the achievable sensitivity of the radio receiver limits system performance. Quantifying the impact of noise when performing both system design and radio receiver design is therefore very important. The properties of Gaussian processes combined with circuit theory allow us to represent electronic noise in familiar terms. Definitions such as voltage noise source, noise temperature and noise figure are most common to quantify the electronic noise for system and circuit analysis. We report here the most common expressions used to quantify noise from the usual voltage, current, power and gain definitions [8] [10] [11].

Voltage and Current Equivalent Noise Sources

By using circuit theory, the thermal noise voltage of Eq. (2.3) can be modeled with a resistor and a voltage noise source ($V_n^2 = \overline{e_n^2(t)}$) as shown in Figure 2.1. The available noise power (P_n) of this source is given by the power delivered to a conjugate matched load R_L at 0 K. We can express the available noise power in the frequency band B as:

$$P_n = kT_sB \quad [\mathrm{W}]. \tag{2.4}$$

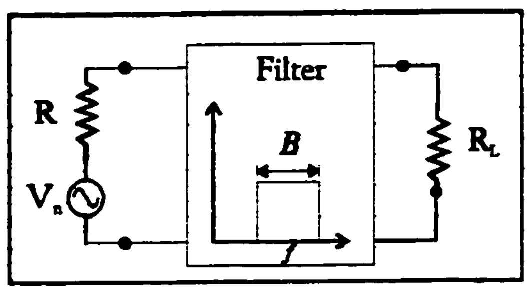

Figure 2.1: Thevenin equivalent circuit

The Norton equivalent, which uses a current noise source in parallel with the resistor R also, applies. Hence

$$I_n^2 = \overline{i_n^2(t)} = 4kT_sB/R \quad [A^2]. \tag{2.5}$$

The current and voltage equivalent noise sources used here represent stationary Gaussian processes. Therefore if two noisy resistors were connected in series, they could be replaced by an equivalent resistor $R_e=R_1+R_2$. This relation holds since for two independent Gaussian processes, the variance of the sum is equal to the sum of the variances of the individual processes [7, p.35] [12].

Noise Temperature

If an arbitrary one-port source of noise is white, it can be modeled as an equivalent thermal noise source satisfying (2.4). This available noise power can be quantified in terms of a noise temperature (T_n) given by:

$$T_n = {}^{P_n}\!/_{kB} \quad [K]. \tag{2.6}$$

Note that unlike T_s, T_n can be different from the ambient temperature of the system. For example, if we know that an avalanche diode activated with a DC current generates a noise power P_n, then the noise temperature of the diode is given by (2.6). Since the noise power is generated by a different physical phenomenon than thermal agitation, the noise temperature T_n is different from T_s , the physical temperature of the diode.

Noise Factor and Noise Figure

A common way of quantifying noise along a signal transmission path is to determine the *noise factor* from the input to the output of the path. Since signals can undergo frequency translation, noise factor (F) is defined for specific input and output frequencies f_{in} and f_{out}. Noise factor is the ratio of the total noise power per hertz at f_{out} available at the output port, when the noise temperature at the input termination is standard (T_0=290K) at all frequencies, over the portion of the output noise power generated by the input termination. It should be understood from this definition that noise factor is only meaningful when specifying the input termination (Γ_s). For a linear network, the output noise generated by the input termination is calculated from the amplified standard available input noise power (kT_0G_aB). Therefore, the noise factor is given by [10]:

$$F = \left. \frac{N_a + kT_0G_aB}{kT_0G_aB} \right|_{T_0=290K,\ \Gamma_s} \tag{2.7}$$

where N_a is the added noise from the input to the output. The noise factor definition is particularly useful to communication systems engineers working in terms of signal to noise ratio (S/N). It can easily be shown that noise factor quantifies the degradation of S/N of a transmission path by [10]

$$F = \left. \frac{(S/N)_{in}}{(S/N)_{out}} \right|_{T_s=T_0,\ \Gamma_s} \tag{2.8}$$

which is sometimes misleadingly referred to as the definition for noise factor. Another misleading practice is to interchange the terms noise factor and *noise figure*. Here we differentiate the two using:

$$F_{dB} = 10\log(F) \tag{2.9}$$

where noise figure (F_{dB}) is the decibel representation of the noise factor (F).

By making use of noise temperature representation for the added noise power ($N_a = T_a k G_a B$), we can simplify (2.7) to:

$$F = \frac{T_a + T_0}{T_0} \qquad (2.10)$$

and equivalently

$$T_a = (F - 1)T_0 \quad [K]. \qquad (2.11)$$

We want to point out that the noise temperature T_a is also called the effective input noise temperature in the context of two-port networks and therefore it provides the same information as noise factor but on a different scale. We conclude from this that the noise figure of a receiver provides the same information as the receiver's effective input noise temperature. Unfortunately both only provide part of the information about the noise behavior of the receiver. We saw that noise figure is meaningful for a specific source impedance presented to the receiver. In practice this means that a change in source impedance will result in a different noise figure for the same receiver. We therefore need to look at a representation for receiver noise behavior which will account for a varying source impedance.

2.2 Electronic Noise in Linear Two-Port Networks

In this section, we review the theory that allows a complete characterization of two-port networks with undefined input and output matching conditions. We also relate this theory to two-port S-parameters. This relation is very useful to microwave circuit designers who make use of the two-port network S-parameters to define gain, stability and power matching conditions of transistors.

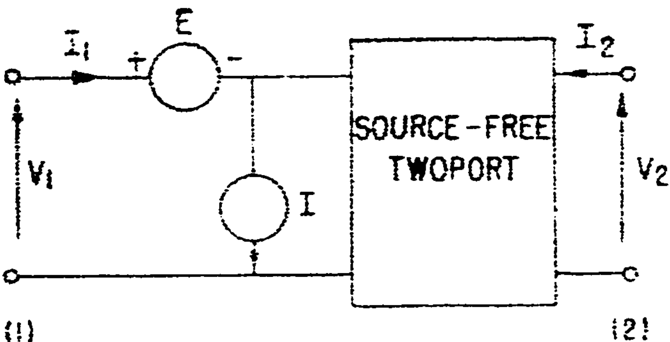

Figure 2.2: Seperation of a two-port with internal sources into a source free two-port and external input current and voltages sources

2.2.1 Representation of Noise in Linear Two-Port Networks

From circuit theory, we know that either port of a linear two-port is completely characterized by the time-dependent voltage *e(t)* and current *i(t)*. Common practice is to transform these signals to the frequency domain voltage (*E*) and current (*I*) and to make use of network parameters such as impedance [Z], admittance [Y], transfer [A] or scattering [S], in order to characterize the two-port. For example, the transfer representation of a two-port with an internal voltage source *E* and current source *I* as shown in Figure 2.2 is given by [13]:

$$\begin{aligned} V_1 &= a_{11}V_2 + a_{12}I_2 + E \\ I_1 &= a_{21}V_2 + a_{22}I_2 + I \end{aligned} \tag{2.12}$$

where $\begin{bmatrix} a_{11} & a_{12} \\ a_{21} & a_{22} \end{bmatrix} = [A]$ is the transfer matrix (or ABCD matrix) of the two-port.

Rothe-Dahlke [14] showed that a noisy two-port network can be represented by a noiseless network (source free two-port) with two correlated noise sources ($e_n(t)$ and $i_n(t)$) replacing *E* and *I* respectively (Figure 2.2). A significant difference here compared to normal circuit analysis is that $e_n(t)$ and $i_n(t)$ are correlated. In the same way that the spectral density of Eq. (2.2) can be quantified in terms of power voltage by Eq. (2.3), $e_n(t)$ and $i_n(t)$ will have self power spectral densities given by [8]:

$$S_e(\omega) = 4kTR_e \quad \text{for } e_n(t) \quad [V^2/Hz]$$
$$S_i(\omega) = 4kTG_i \quad \text{for } i_n(t) \quad [A^2/Hz] \quad (2.13)$$

where R_e is an equivalent noise resistance, and G_i is an equivalent noise conductance. For our representation to be complete, we must define a complex correlation coefficient. We can compute the cross spectral power density, S_x, between $e_n(t)$ and $i_n(t)$, and then represent it by a complex equivalent noise impedance $\gamma_r + j\gamma_i$ which is given by [15]

$$2\left[S_{xr}(\omega) + jS_{xi}(\omega)\right] = 4kT\left(\gamma_r + j\gamma_i\right) \quad [V^2 / Hz] \quad (2.14)$$

Note that the self- and cross-power spectral densities are defined as the Fourier transform of the auto- and cross-correlation of the Gaussian process, respectively. This is applicable to stationary random processes. Re-arranging these spectral densities in a 2x2 matrix leads to the so-called noise correlation matrices [15]. The noise correlation matrices have to be Hermitian and non-negative [16]. The four parameters making up the matrix are referred to as the *noise parameters* (NPAR). Many representations of the noise parameters exist. There is the Π- and T-Matrix of Rothe and Daklke [14], the wave representation (a_n, b_n, Z_v) [17], the IRE standard representation (F_0, R_n, $Y_0=G_0+jB_0$) [13], Lange's representation (F_{op}, N, Y_{op}) [18], the Hillbrand correlation matrix associated with electrical network representation (C_A with chain, C_Z with impedance, and C_Y with admittance) [15], the representation in terms of noise temperature (T_{min}, N, Y_{opt}) or (T_{min}, N, Z_{opt}) [16], the microwave representation (F_{min}, R_n, Γ_{opt}), and other combinations of the above. We prefer to use the microwave representation expressed in terms of a minimum noise figure (F_{min}), a complex optimum reflection coefficient (Γ_{opt} magnitude and phase), and noise resistance (R_n). More details about these representations can be found in Appendix Appendix A.

2.2.2 Noise Signal Computation with Linear Two-Port Networks

An efficient computational technique was presented by Hillbrand and Russer in [15] which makes use of the correlation matrix representation ($\mathbf{C_A}$, $\mathbf{C_Z}$, and $\mathbf{C_Y}$). The technique uses the two-port network as a unit cell to compute bigger (or smaller) linear two-ports electrical and noise parameters. For example, if we cascade network #1 and network #2 to create network #3, we can compute the electrical parameters of network #3 by multiplying the transfer matrix [A] of networks #1 and #2. We can also get the new noise correlation matrix from [15]

$$\mathbf{C}_{A3} = \mathbf{A}_1\mathbf{C}_{A2}\mathbf{A}_1^{+} + \mathbf{C}_{A1} \qquad (2.15)$$

where $\mathbf{A}_i$ is the transfer matrix of network i, $\mathbf{C}_{Ai}$ is the associated transfer correlation matrix, and + denotes Hermitian conjugation. For the series connection of two-port networks, impedance correlation matrices are simply added together (ie. $\mathbf{C}_{Z3} = \mathbf{C}_{Z1} + \mathbf{C}_{Z2}$) and similarly, for parallel connection the admittance correlation matrices are added (ie. $\mathbf{C}_{Y3} = \mathbf{C}_{Y1} + \mathbf{C}_{Y2}$) These relations are even more useful when we know that for passive networks in thermal equilibrium, the impedance and admittance correlation matrices are simply given by [15]

$$\begin{aligned}\mathbf{C_Z} &= 2kT_s\,\mathrm{Re}\{\mathbf{Z}\}\\ \mathbf{C_Y} &= 2kT_s\,\mathrm{Re}\{\mathbf{Y}\}^{*}\end{aligned} \qquad (2.16)$$

For example, if we apply nodal analysis to determine the admittance matrix of the passive network shown in Figure 2.3, we can then state that this network is completely characterized by:

$$\mathbf{Y} = \begin{bmatrix} 0.06 & -0.04 \\ -0.04 & 0.04 \end{bmatrix} \text{and } \mathbf{C_Y} = 2kT_s\begin{bmatrix} 0.06 & -0.04 \\ -0.04 & 0.04 \end{bmatrix}. \qquad (2.17)$$

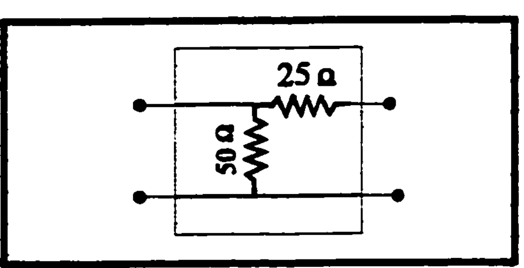

Figure 2.3: Resistive two-port network

We can now transform the admittance representation just obtained for this specific network to any other representation using relations given in Appendix Appendix A. When expressed as F_{min}, Γ_{opt}, and R_n we have $F_{min(dB)}=5.72$dB, $\Gamma_{opt}=0.268\angle 180$ and $R_n=25\ \Omega$.

2.2.3 Relation Between Noise Figure and Two-Port Noise Signals

The main goal in designing a low noise amplifier is to present to the input of the transistor the optimum impedance (Γ_{opt}) to achieve the minimum noise factor (F_{min}). Although we showed in the previous section how to compute the noise parameters we have not yet shown how the noise figure of the amplifier (or network) is affected by the source and load impedance presented to it. Let us derive this relation.

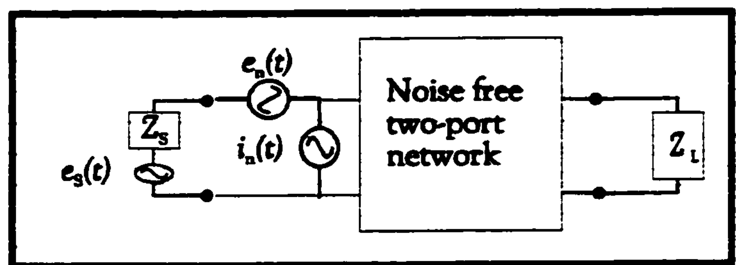

Figure 2.4: Noise free two-port network with source impedance

The power transferred from one network to another is easily computed with S-parameters. Definitions of available power (P_a), delivered power (P_d), and mismatch factor ($M=P_d/P_a$) describe well how the power transfer occurs [8 p.334]. By applying such computation techniques to the specific case of Figure 2.4, it can be shown that the total noise delivered to the noise free two-port is [8 p.764]

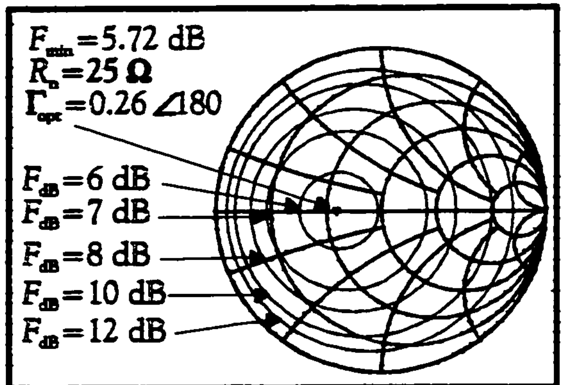

Figure 2.5: Noise circles for the resistive network of Figure 2.3

$$P_n = B\left\{ S_e(\omega)\frac{M}{4R_s} + S_i(\omega)\frac{M}{4G_s} + \frac{4\left[S_{xr}(\omega)R_s + S_{xi}(\omega)X_s\right]}{\left|Z_s + Z_{in}\right|^2} R_{in} \right\} \tag{2.18}$$

where $Z_s=R_s+jX_s$ is the source impedance, $Z_{in}=R_{in}+jX_{in}$ is the input impedance of the network, and $G_s=R_s/|Z_s|^2$. From the definition of noise factor, and by replacing the power spectral densities in (2.18) with the equivalence of (2.13) and (2.14) we obtain

$$F = 1 + \frac{R_e}{R_s} + \frac{G_i}{G_s} + 2\frac{R_s\gamma_r + X_s\gamma_i}{R_s}. \tag{2.19}$$

The optimum noise factor is obtained by taking the partial derivative of (2.19) with respect to R_s and X_s. Then, after a number of manipulations, we obtain the following expression for the noise factor of two-port networks as a function of the input source impedance (Γ_s):

$$F = F_{min} + 4\left(\frac{R_n}{Z_0}\right)\frac{\left|\Gamma_s - \Gamma_{opt}\right|^2}{(1 - \left|\Gamma_s\right|^2)(\left|1 + \Gamma_{opt}\right|^2)} \tag{2.20}$$

where Z_0 is the characteristic impedance used. By using Eq. (2.20), it can be shown that, for the specific case calculated in Section 2.2.2, the noise figure maps as circles over the Smith chart representation of the input impedance as shown in Figure 2.5 [8 p. 772].

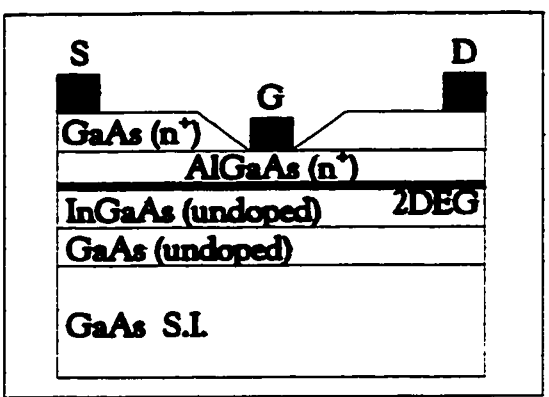

Figure 2.6 Typical cross section of a PHEMT

2.3 The Pseudomorphic High Electron Mobility Transistor

The fundamental operation of the pseudomorphic high electron mobility transistor (PHEMT) is based on the field effect transistor (FET). As such, the noise behavior of HEMTs and PHEMTs is often considered an extension of the theory of noise in FETs. Our interest for noise models in this thesis is limited to finding general governing rules, which will help us in validating measurements made on a PHEMTs. Before we go into some of the details in noise modeling, let us first briefly describe the PHEMT device.

2.3.1 The PHEMT Device

The technology of Molecular-Beam Epitaxy (MBE) made possible the creation of heterojunctions such as $Al_xGa_{1-x}As/GaAs$ in semiconductors which in turn gave birth to a new type of transistor known as the HEMT (also called MODFET or 2DEGFET or SDHT) [19] [20]. In the case of the PHEMT, a layer introducing different types of atoms (ie AlGaAs/InGaAs/GaAs) is brought into the equation. A typical cross section of these transistors is shown in Figure 2.6 [21]. This new atom (indium in this example) will produce a misfit dislocation, which arises from a lattice mismatched pair of semiconductor layers. It was found that if a lattice mismatched layer was grown sufficiently thin, then the mismatch could

be accommodated entirely as elastic strain. The operation of the FET structure is significantly enhanced through the use of the heterostructure, which creates a region refered to as a two dimensional electron gas (2DEG). The 2DEG was shown to have improved the low-field electron mobility [22] [23].

Our interest in this device comes from its ability to provide higher gain and lower noise figure at millimeter waves. Tan et *al*. reported the successful fabrication of a 0.1 um gate length PHEMT achieving a noise figure of 2.1 dB at 93.5 GHz [24]. This record breaking reports of low noise figure and unity frequency gain of PHEMT still goes on today. The noise modeling of these devices at millimeter wave frequencies was previously performed and therefore should provide us with some valuable information.

2.3.2 Noise Models for PHEMT Devices

Noise models for devices can be broken up into two categories: physical models and empirical models. Physical models are derived from actual material properties and are therefore more useful in aiding the design of a device and improvement to foundry processe. Generally speaking, most papers published may be viewed as progressively more sophisticated treatments of the problems originally tackled by Van der Ziel for FETs. Empirical models, on the other hand, are derived from measurements of specific device parameters to provide the circuit designer with an effective model, which will take noise into account in CAD tools. In both cases, the final representation in a noise model is generally done through an equivalent lumped voltage noise source, current noise source, or equivalent noisy resistor.

Although the HEMT structure is different from that of the MESFET, the methods employed in noise studies are basically the same. In [25], Brookes presents a simple analytical model for a HEMT by modifying the FET noise model reported by Van der Ziel [26] and Pucel et *al* [3]. The Brookes model takes into account only the thermal noise in the channel and expresses it in terms of the intrinsic transistor noise coefficient parameters P, R and C which were

originally defined by Van der Ziel in 1962 and reused by Statz and Pucel in a more complete model for the FET [3]. Cappy et *al.* also presented a model for a submicrometer-gate two dimensional electron-gas field effect transistor (2DEGFET) in [27]. Other model and noise analysis for HEMTs includes Joshin 1989 [28], Pospieszalski 1989 [29] [30], Ando 1990 [31], Hickson 1992 [32], Anwar 1993 and 1994 [33] [34], Felgentreff 1994 [35].

After looking at the resulting relations derived from the above model list, we can make a number of comments with regards to the general trend of the noise parameters for a PHEMT (or HEMT) in our frequency band of interest (26 to 40 GHz). We identified that:

- the minimum noise figure (F_{mindB}) increases with frequency,
- the noise resistance (R_n,) decreases with frequency,
- the optimum reflection coefficient (Γ_{opt}) rotates counter-clockwise with frequency on the Smith chart,
- starting with a drain current Ids ≈15% of Idss, the minimum noise figure (F_{mindB}) gradually increases with drain current (Ids). Note that for Ids< 15 % of Idss, F_{mindB} rapidly increases with Ids.

These comments conclude our discussion on the noise model for a PHEMT. Providing more details on specific models to relate it to our measurement was considered for this thesis but had to be discarded. The main reason for this was the lack of information provided by the foundry about the device being measured.

2.4 Conclusion

This chapter presented the theoretical foundations required for the millimeter-wave noise characterization of PHEMT devices. The focus was placed on the representation of thermal electronic noise, which can be used at millimeter-waves to represent PHEMT devices. Actual

noise modeling of the PHEMT from physical parameters or lumped element equivalence was briefly studied to determine the expected trends of the noise parameters.

3. Measurement Techniques

The most commonly used techniques for measuring the noise parameters are presented in this chapter. The details of noise figure measurement are presented before explaining a number of noise parameters measurement and extraction techniques. We also introduce the advantages and difficulties of on-wafer probing at the end of this chapter.

3.1 Noise Figure Measurement of a Two-Port Network

3.1.1 The Y-Factor Measurement Technique

By taking a closer look at Eq. (2.7), we see that noise factor is not measured directly but must be derived from available gain (G_a), added noise (N_a) and bandwidth (B) of the DUT. We now refer to Figure 3.1 where we show a linear DUT and a graph representing the output available noise power as a function of input noise temperature (or noise power). Since the DUT is linear, the relation between input noise temperature and output noise power is a straight line of slope $m=kG_aB$ and y-intercept=N_a. Two measured noise powers corresponding to two known input noise temperatures are required to determine the gain-bandwidth product (kG_aB), and the added noise N_a.

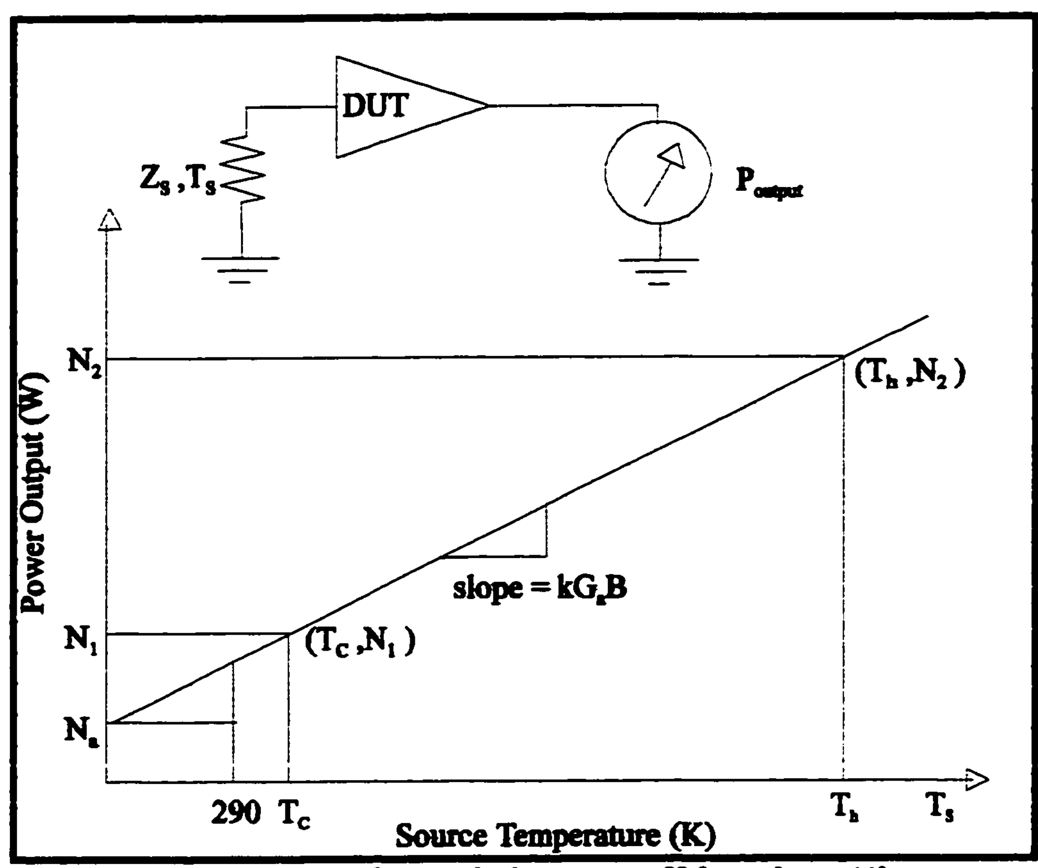

Figure 3.1: Noise figure calculation using Y factor [11 p. 11].

To generate the two noise powers at two known noise temperatures, a physically heated and cooled termination is used and these constitute the fundamental physical standards. A termination placed in liquid nitrogen at a temperature of about 77 K is commonly referred to as a cold noise source. The hot noise source is usually a termination kept in an oven regulated to 373 K. The fundamental noise source standards are primarily used to calibrate other types of noise source, which are more practical and faster for day-to-day measurements. The most common of which is certainly the solid-state avalanche diode. The avalanche diode generates hot and cold noise power by applying to it a bias of +28 and 0 V respectively. Noise diodes have to be calibrated to determine their equivalent hot noise temperature (T_h) at every frequency. The calibration table will generally be given in the form of excess noise ratio (*ENR*) expressed in dB and related to T_h by [10]:

$$ENR(dB) = 10\log_{10}\left(\frac{T_h\left(1-|\Gamma_{NSh}|^2\right)-290}{290}\right) \qquad (3.1)$$

where Γ_{NSh} is the noise source hot state reflection coefficient. The definition presented here is what is calibrated by the United States National Bureau of Standards. A common simplification is to assume that $\Gamma_{NSh}=0$ in (3.1). We note that this simplification is sometimes used as the *ENR* definition.

A means of measuring the noise power is also required. An accurate power detector is needed for that purpose. The requirement for extremely accurate power measurements can be reduced by using the *Y-factor* technique. The Y-factor is the ratio of the hot noise power (N_2) over the cold noise power (N_1). After algebraic manipulation, Eq. (2.7) is written as [10]:

$$F = \frac{\left(\frac{T_h}{T_0}-1\right)-Y\left(\frac{T_c}{T_0}-1\right)}{Y-1} \qquad (3.2)$$

where

$$Y = \frac{N_2}{N_1} = \frac{N_a + kT_hG_aB}{N_a + kT_cG_aB} = \frac{kT_aG_aB + kT_hG_aB}{kT_aG_aB + kT_cG_aB} = \frac{(T_h + T_a)}{(T_c + T_a)} \qquad (3.3)$$

The Y factor is more accurately measured than absolute noise power by making use of an accurate variable attenuator to keep an equal power reading for both noise source states. The change in attenuation setting between the hot and the cold states of the noise source is equal to the Y-factor. A block diagram of a typical lab setup using the Y-factor technique is shown in Figure 3.2 [11]. This diagram doesn't show the attenuator since the digitization of the measurements eliminates this function by providing accurate relative power readings.

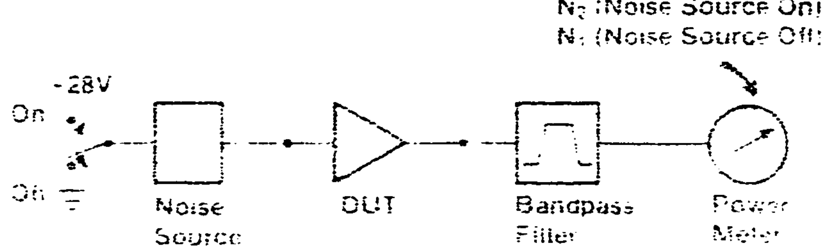

Figure 3.2: Y factor noise figure measurement set up

The accuracy of the Y-factor measurement is closely related to the uncertainties in T_h and the quality of the input and output match. As well, the uncertainty is increased by the fact that the output impedance for the avalanche diode is not nominal and varies between the hot and cold states. A general uncertainty analysis in noise measurement systems was made by Pradell and is reported in [36]. His analysis provides an expression which allows the identification of errors for systems that use the Y-factor method. This expression can then be used to determine the error limits on the noise figure measurement of microwave low-noise amplifiers. As well, Hessen-Schmidt [37], showed how the noise figure measurement accuracy depends on the properties of the noise source and how newer types of noise sources improve the measurement accuracy.

3.1.2 The Y-Factor Technique at Microwave Frequencies

The measurement of noise figure at microwave frequencies involves the insertion of a receiver (typically an LNA with a single sideband filter and a down-converter) between the DUT and the bandpass filter of Figure 3.2. The receiver not only amplifies noise power at the output of a DUT, but it also adds internally generated noise. We must therefore account for these two factors which we call the second stage effects. In order to de-embed noise generated by the receiver from the noise of the DUT, we make use of the Friss equation [38]:

$$F_T = F_{DUT} + \frac{F_{rcvr} - 1}{G_{DUT}} \tag{3.4}$$

where F_T is the total measured noise factor, F_{rcvr} is the receiver noise factor, and F_{DUT}, G_{DUT} are the noise factor and gain of the DUT respectively.

We should point out that it is possible to evaluate the noise factor of the DUT without using the single sideband filter in front of the downconverter by assuming that the noise power in both sidebands of the DUT are equal. If we do, then we know from mixer theory that both sidebands will be down-converted into the same bandwidth and therefore, we should correct by dividing our power reading by two. This technique is referred to as a double side-band (DSB) noise figure measurement. The DSB technique is frequently used for LNA noise figure measurements. Unfortunately, for device characterization, the DSB technique introduces a large errors in the noise parameter measurement due mainly to the variations of source impedance with frequency [39]. We therefore limit ourselves to the SSB noise figure measurement method.

3.2 Noise Parameter Measurement Techniques

Although system engineers rely exclusively on the noise factor to compute system performance, complete noise characterization of two-port networks requires the measurement of all four noise parameters (Section 2.2). We will see in this section how measurement techniques have evolved from a tedious experimental search into automated noise parameter measurement systems.

3.2.1 IRE Standard Technique

A technique approved by the IRE Standards Committee in 1959 [40] for the measurement of noise parameters (F_{min}, R_n, $Y_{opt}=G_{opt}+jB_{opt}$) consists of experimentally tuning the input impedance until the minimum noise figure F_{min} and the corresponding source admittance are found. The equivalent noise resistance, R_n, is then determined by a measurement at a different source impedance, Y_s. This practice is unsatisfactory for two main reasons [41]:

- It is tedious and inaccurate to determine Y_{opt} since the partial derivative of the noise figure with respect to source impedance is zero at the minimum; and
- transformation-dependent losses in the input matching network, which is not accounted for, bias the obtained value of Y_{opt}. Note that at millimeter waves, the transformation dependent input matching losses are even more significant.

For these two reasons, Lane proposed a simple technique, which directly extracts the noise parameters from a least-square fit optimization [41].

3.2.2 Noise Parameter Extraction Techniques

The technique proposed by Q.Lane in 1969 [41] is called the multiple impedance noise measurement technique. In principle, measurement of noise factor at four different source impedances Y_S is sufficient to determine the four noise parameters. Since uncertainties corrupt the measurements, a larger number of measurements (seven was proposed by Lane) allows statistical smoothing of the noise figure surface when computed using the least square fitting procedure. A shortcoming of Lane's algorithm is high error sensitivity caused by ill-conditioned matrices, which occurs with a bad selection of input impedances [42]. Other algorithms, which include totally new formulations or a simple variation on the original algorithm, have since been developed to achieve better accuracy [43]. We would like to emphasize O'Callaghan's technique [44], detailed in Appendix Appendix C, which makes use of a vector formulation. By arranging Eq. (2.20) in the form of a linear combination of vectors, O'Callaghan was able to extract the noise parameters. The formulation is composed of five N-dimensional vectors generated from the source impedances and associated noise factor. N is the number of selected source impedances. The N source impedances are referred to as the *constellation* of impedances used for the extraction of the noise parameters.

3.2.3 Selection of the Impedance Constellation

The proper selection of a set of impedances to compose a constellation is often presented as a way to average out the errors on the measured parameters. The opposite is far more striking in that a bad selection of the constellation may totally destroy the validity of the extracted parameters. Lane himself pointed out a similar shortcoming with his original fitting routine [41]. It should be noted as well that changing the extraction algorithm could give different results for the same constellation. We justify this statement by pointing out that the main difference between extraction algorithms is in the formulation of the error function being minimized to extract the noise parameters. Although at least 7 extraction algorithms exist [41][45][46][47][48][49][44], we limit our study on the selection of the impedance constellation to Lane's [41] and O'Callaghan's [44] extraction algorithms.

For Lane`s technique, we learn from Sannino [42] that a bad selection of the constellation may cause matrix ill-conditioning when the admittances (or impedances) all lie in the neighborhoods of some singular loci. Eleven admittance loci conditions that produce ill conditioning were determined. To avoid ill conditioning, it is suggested to simply compose a constellation by selecting impedances from two different loci. However, this doesn't guarantee that none of the eleven conditions is satisfied and all have to be verified individually. The method doesn't provide any indication that the selection is an optimum constellation.

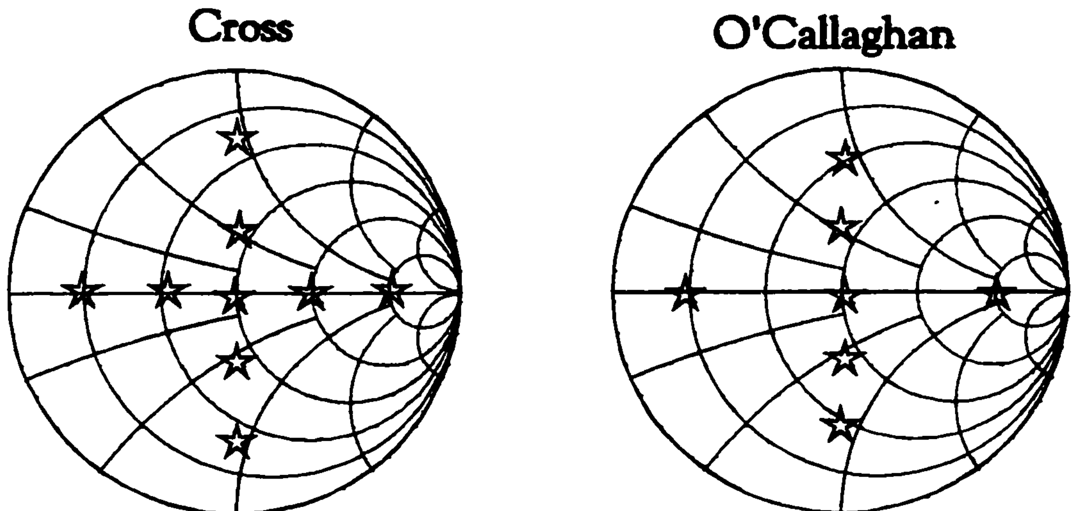

Figure 3.3 The Cross and O'Callaghan's optimum constellation

The problem of selecting the number and location of source impedances to form the best constellation was dealt with in [50]. Simulated measurement conditions were generated from the known noise parameters (F_{mindb}=1.5 dB, $\Gamma_{opt}=0.75\angle 0$, $R_n=103\ \Omega$) of a device. Arguments to select a constellation of nine points as shown in Figure 3.3 were presented. Unfortunately, the specificity of the simulation raises some questions about the generality of the conclusion of that study. In fact, it is shown in [51] that for the case where the real part of the optimum impedance (R_{opt}) is not enclosed by the constellation, the uncertainty on the extracted noise parameters is greater. It is also pointed out that unless this is the case, an excellent fit of the noise parameters to the noise data is not a proof of the correctness of the noise parameters.

O'Callaghan's algorithm has a definite advantage over Lane's for the selection of the impedance constellation. The advantage comes from the vector formulation, which provides a quantifying parameter (obtained from the calculation of the orthogonality between each vector) used to evaluate matrix conditioning. Minimizing the condition number resulted in a

constellation of seven impedances presented in Figure 3.3. Note that Smith chart coverage was limited to the maximum radius of 0.7.

Unfortunately none of the papers found in the literature suggest a way to take all factors into account in order to determine the best constellation for a specific measurement. Indeed, the parameters of the DUT being measured play a large role in defining the accuracy of the various parameters being measured. Hence, it is extremely valuable to be capable of generating impedances everywhere around the Smith chart to determine the optimum constellation for specific noise parameters.

3.3 Common Measurement Setup

Several investigators proposed so-called *automated noise parameter measurement setup* since Lane published his parameter extraction algorithm [41]. We classify these setups in two categories. The first one uses the Y-factor technique to measure the noise figure for all impedances of the constellation [52] [45] [53] [16] [54] [48] [55] [56] [57]. We refer to it as the *hot/cold* technique. The second one uses the *cold power* technique originally introduced by Adamian and Uhlir [58] [50] [59]. A presentation of typical setup and procedure used in both techniques is made in this section.

3.3.1.1 Hot/Cold Technique

For the hot/cold technique, the setups make use of an input tuner in front of a DUT to generate multiple input impedances as shown in Figure 3.4. The noise factor of the combined input tuner and DUT is then measured using the Y-factor technique. Since we are interested in the DUT noise parameters only, the tuner and receiver noise parameters must first be measured in order to de-embed them from the measured noise factor. The noise parameters of the tuner are determined from the measurement of its available gain (or equivalently its S-Parameters) at each point of the constellation. The receiver noise parameters are obtained by

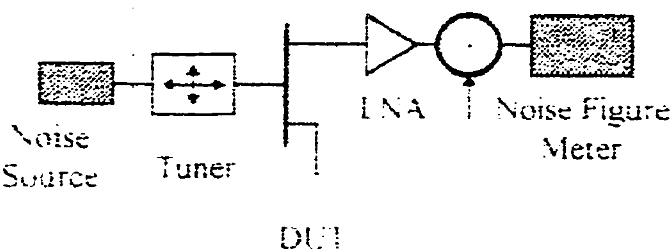

Figure 3.4: Hot/cold noise figure parameter measurement setup

removing the DUT from the setup and performing a complete noise parameter extraction. Having characterised the receiver noise figure and the tuner available gain for each point of the constellation, the DUT noise factor is determined from Friss Eq. (3.4) and the ENR correction given by Eq. (4.1). Using the set of noise factors obtained for the constellation of input impedances, the DUT noise parameters are extracted using one of the mathematical algorithms discussed in Section 3.2.2.

3.3.1.2 Cold Technique

The rationale of the cold power technique consists of first fully characterizing the receiver so that subsequently only one measurement of noise power is needed to characterize a DUT instead of two (one hot, one cold) as in the hot/cold technique. For simplicity, this measurement is performed with a passive noise source at room temperature, a so-called "cold" source. The "receiver" is the one-port network consisting of the chain of amplifiers, mixers, and filters terminated by the power meter (Figure 3.5). Obviously, the cold technique requires a receiver that is very stable over time.

This being said let us explains how cold power measurements can be sufficient to determine the DUT noise parameters. We recall from Figure 3.1 that for a specified source impedance connected at the receiver reference plane, the power meter reading can be computed from the source impedance available noise power (P_a), the gain-bandwidth constant (kG_aB), and the

noise added (N_a) by the receiver. Generalization of this relation for any source impedance (Z_s) connected to the receiver is possible by knowing the receiver noise parameters, the receiver reflection coefficient, and by introducing the kBG_0 term. The kBG_0 term is a characteristic of the receiver, which is independent of source impedance and from which the gain bandwidth constant (kG_aB) can by computed as explained in Appendix Appendix B. Thus, by using the receiver noise parameters, reflection coefficient and kBG_0 term, the power meter reading can be related to the available noise power at the input of the receiver. We see from Eq. (2.7) that the DUT noise factor can be obtained from the output noise power ($N_a+kT_0G_aB$) divided by the available input noise power amplified by the DUT (kT_0G_aB). Hence, the DUT noise factor can be obtained by measuring the output noise power with a characterized receiver and by computing the DUT available gain G_a from measured S-parameters. The DUT noise parameters are then obtained by measuring the DUT noise factor for a constellation of at least 4 source impedances as required by the mathematical algorithms discussed in Section 3.2.2.

To better understand the receiver characterization, we now review the formulation introduced by Adamian and Uhlir [58], which relates source impedance available noise power to the power reading of a receiver. If we replace the load impedance (Z_L) in Figure 2.4 by a power meter and we assume that the noise free two-port is a linear receiver, we can state that the power meter reading will be proportional to the power absorbed by the receiver input admittance Y_{in}. The power reading for a particular source ($Y_s=1/Z_s$) is [58]:

$$P_s = \frac{4kT_0BKG_{in}}{|Y_{in} + Y_s|^2}\left\{|Y_s + Y_{cor}|^2 R_n + G_n + t_{ns}\,\mathrm{Re}[Y_s]\right\} \qquad (3.5)$$

where Y_{cor}, R_n, G_n are the receiver noise parameters (Π representation of Rothe and Dahlke), G_{in} is the receiver available gain, $t_{ns}=T_{ns}/T_0$ is the source available noise temperature over the standard temperature ratio, and K is a proportionality constant. Considering that the

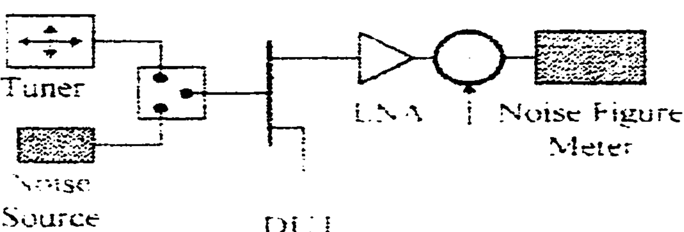

Figure 3.5: Cold power noise parameter measurement technique

receiver input impedance and the source impedance can be measured, the formulation to compute the noise parameters of any receiver identifies five unknowns which can be determined from the measurement of five output powers for five known source impedances, each with a known excess noise temperature (t_s). The five unknowns are the four noise parameters plus the *BK* term. The *BK* term can be related to the kBG_0 term previously introduced by looking at the relations in Appendix Appendix B. Hence, we can consider the receiver kBG_0 term to be the fifth unknown. Solving the set of equations obtained from Eq. (3.5) to determine the five unknowns requires that we select at least one of the available noise temperatures (t_{ns}) to be different from the others. The requirement for hot noise power measurement is therefore reduced to one measurement only with the cold technique.

The measurement procedure for the cold power technique may be performed by using the setup presented in Figure 3.5. First, we replace the DUT with a thru line and switch to the noise source to measure the gain bandwidth constant (from which the kBG_0 term is computed) of the receiver from a hot and cold noise power measure. We then switch to the tuner and present a minimum of four source impedances to determine the noise parameters of the receiver. Second, we measure the S-parameters of the DUT and the reflection coefficient of the receiver from which the available gain of the DUT is determined. Third, we measure at least four output noise powers of the combined DUT and receiver. All required measurements

are now complete and the DUT noise parameters can be computed in two steps. First, the computation of the noise factor of the DUT associated with each measured impedance is made. Second, the DUT noise parameters are extracted using one of the mathematical algorithms discussed in Section 3.2.2. Note that alternative computation sequences are also possible [50].

At millimeter waves, the cold technique has an important advantage over the hot/cold technique. The advantage has to do with the S-parameter characterization of the tuner for the various states it is placed in. We learn from [60] that when the tuner presents a high reflection coefficient (e.g. $|\Gamma_s|=0.7$) then the uncertainty on the available gain measured is ±0.1 dB for an uncertainty of ±0.01 (1.5 %) on $|S_{22}|$ only. Note that the typical reflection coefficient uncertainty of a vector network analyzer is ±0.015 at 18 GHz [61]. In addition, more uncertainty is introduced in our case since the S-parameter measurement of the tuner needs to be performed from a coaxial transmission line (noise source reference plane) to an on-wafer transmission line (DUT reference plane). We conclude that the hot/cold technique introduces a serious accuracy limitation. This may not be the case for the cold power technique since the tuner needs only to be characterized for reflection coefficients presented to the DUT. In this work we use the cold technique

3.3.2 Conclusion

In conclusion, we may say that the noise parameter extraction has evolved from a tedious and slow procedure to being a sophisticated technique requiring the use of computers and a network analyzer. Although the new procedures promise to be more users friendly by their automation, they remain highly complex to implement due to the large number of interacting measurements made and due to the mathematical extraction algorithms used. Hence, the

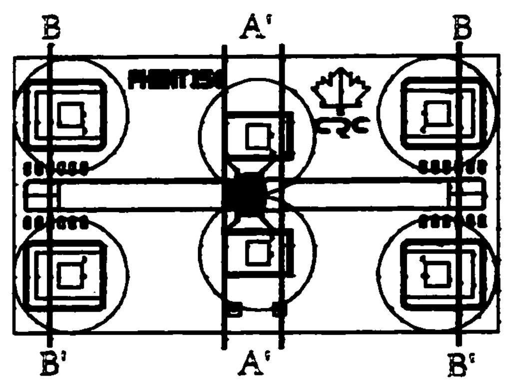

Figure 3.6 Layout of a 150 um parallel finger PHEMT with TRL transmission line and probing pad.

impact of test equipment deviation from assumed behavior is difficult to detect and can often lead to unexplained results.

3.4 On-Wafer Probing

The characterization of a new device is most efficient using on-wafer probing since a newly produced wafer can be tested without the need for scribing, die attaching and wire bounding to a test jig. Although no verification standard exists for on-wafer S-parameter calibration [62], techniques such as the thru-reflect-line (TRL), the line-reflect-match (LRM) and others are considered sufficiently accurate and are commonly used in the industry. Unfortunately, the various calibration techniques can give significantly different noise parameter mesurements at microwave frequencies [63]. Despite this fact, on-wafer probing is preferred over coaxial systems for its good probing repeatability and for the direct measurement of device parameters. The divergence between the various calibration techniques is still an active topic of research and NIST is presently developing a verification standard for on-wafer probing at millimeter waves [62].

For our experimental investigation, we limit ourselves to using the TRL microstrip calibration standards on GaAs. The calibration standards are optimized for 1 to 40 GHz and

are commonly used by the Communications Research Centre[1]. The layout of a PHEMT with TRL microstrip transmission lines and with two reference planes (AA' and BB') is shown in Figure 3.6. Measurements at the DUT at reference plane (AA') is preferred over measurement at the probing pad reference plane (BB') for two reasons: First, a reference plane at the DUT defined via a TRL calibration will eliminate the effects of the transition from the probe to the planar transmission lines. Second, when the DUT is used in an amplifier design, the transition from the transmission line to the transistor is often that of a microstrip line to the transistor. This implies that the DUT to be tested should be provided with an integrated transmission lines between the DUT and the probing pads. This may not always be possible due to space limitation asssociated with the fabrication of wafers. Probing of devices without the TRL calibration transmission lines is not prohibited but a greater uncertainty on the S-parameter measurements should be expected. The main reasons are the ambiguity in the definition of the reference plane and the possible generation of unwanted electromagnetic modes due to the transition from the probe (coplanar transmisison line in air) to the probing pads. The layout of the device measured in this thesis is as shown in Figure 3.6.

3.5 Conclusion

The measurement techniques used for noise figure measurements and noise parameter measurements were presented in this chapter. We recall that the hot/cold technique is based on the Y-factor technique, which requires the complete characterization of the input block from S-parameter measurements. The cold technique on the other hand is based on a more general formulation of the problem, which eliminates the requirement for hot power measurements at all source impedance except one. On-wafer probing was introduced as a

---

[1] This work was done in the labs of the CRC of the Government of Canada.

more efficient way of getting the information required from new devices. A good portion of the challenge in on-wafer noise parameter measurements is to become familiar with all the details of the test equipment used. As well, the level of the signal being measured requires the operators to always be careful about interfering signals which can be picked up from many sources. A word of caution about noise parameter measurements is that when an unexpected behavior arises, it often means that something important needs to be looked at before valid measurements can be made.

4. On-Wafer Resistive Noise Source

Calibrated noise sources are presently only available for coaxial and waveguide transmission lines. There exists no noise source standard for planar transmission line structures such as the microstrip line or the coplanar waveguide. The main reason is that these transmission line structures cannot easily be connected and disconnected to a planar DUT in order to perform hot/cold noise figure measurements. Fortunately, this limitation does not apply when the noise parameters are determined from S parameters and the cold measurement technique. The calibration of an on-wafer noise source, which consists of a simple noise diode connected on a coplanar structure, was proposed by Hughes and Tasker in [64]. In the course of this research we developed a different type of on-wafer noise source. We present here the novel on-wafer noise source which we believe to be promising by its simplicity and ease of use.

4.1 Description

Figure 4.1: On-wafer resistive noise source (ORNS))

The proposed on-wafer resistive noise source (ORNS) is shown in Figure 4.1. It consists of a thin film 50-ohm resistor embedded in a coplanar structure. Figure 4.1 actually shows one of Cascade Microtech's Tantalum Nitride (TaN) load standards found on their alumina impedance standard substrate (ISS) which is normally used for on-wafer S-parameter calibration. We learned from Figure 3.1 and Eq. (3.5) that to be useful, the ORNS needs to provide two known available noise temperatures, T_c and T_h, or equivalently t_{n1} and t_{n2}.

When at room temperature, the resistor is equivalent to a noise source in its cold state. That is it generates a noise power determined by $P_c=kT_cB$ which is naturally calibrated to the ambient temperature T_c. The hot state of this noise resistor is obtained by forcing a DC current through it which effectively heats up the resistor. The resistor will now generate the hot noise power state $P_h=kT_hB$ where T_h is defined as the averaged hot temperature. Due to the small size of the on-wafer resistive noise source (ORNS), the transition time between a cold state ($T_c \approx 296K$) and a hot state ($T_h \approx 500K$) is estimated from laboratory power measurements to be less then 2 seconds. This transition time is valid for both T_c to T_h and T_h to T_c.

Obviously, the transition time is not the only parameter to evaluate in order to sanction the ORNS as a usable noise calibration standard. The critical parameter is the averaged hot temperature of the ORNS when exposed to a specific biasing current. The simple approach to this problem is to measure the hot power P_h for a specific current and, by using the calibration procedure described in the next section, to extract the averaged hot temperature T_h.

Let us take a closer look at what is happening. Laws of physics tell us that thermal vibrations in materials randomly interact with electrons to create thermal electronic noise. By flowing a DC current (I) through a resistive material, we force the dissipation of thermal power ($P_{th}=RI^2$) into the resistor. The dissipated power increases the temperature distribution of the material until a new thermal equilibrium is reached. Thermal equilibrium that is characterized by constant heat transfer from the resistor to its environment results in the temperature staying constant at all locations in the material. As we have not studied the generation of electronic noise in materials with temperature gradients, and since we don't know what it will be in our case, we *assume that the ORNS is generating thermal electronic noise power which can be represented by an averaged hot noise temperature* (T_h). If this is the case, we can state that the available electronic noise power at all frequencies is given by $P_h=kT_hB$. To determine the

relation between T_h and the physical temperature of the resistor would require a themal analysis, which is beyond the scope of this thesis.

Another point of concern is the change in the resistance of material with increasing temperature. The Tantalum Nitride (TaN) resistor temperature coefficient of resistance (TCR) is specified as -125 ppm/°C by Cascade Microtech [65]. This means that a 50 Ω resistor with a temperature increase of 200K will become a 48.75 Ω resistor. The change in resistance doesn't change the available noise power, which is determined by kT_hB but it will change the delivered noise power to the receiver. Here, the change represents a change in the reflection coefficient of 0.0127=-38dB. We can therefore safely make the approximation that the delivered power in a 50-ohm system is approximately the same for both states. This change of impedance is known to affect all types of noise sources. By comparison, the avalanche noise diode used in some of our experiments suffers from reflection coefficient change as high as 0.05=-26 dB. We can therefore consider this as a minor concern at this point.

Resistors are also known to degrade with time and usage. High temperature of operation accelerates the degradation. This phenomenon is minimized by keeping the operating temperature below the annealing temperature of the resistor used [66]. We are careful during our experiment not to exceed the annealing temperature (~700 K) and to also monitor the resistor value from time to time.

Finally, our intent here is to demonstrate the performance of an ORNS when it is calibrated with a coaxial noise diode as explained in Section 4.2. Our demonstrations include the calibration of the ORNS and the measurement of the receiver noise figure. In addition, comparison of extracted noise parameters from 26 to 40 GHz, by making use of a Hewlett Packard coaxial noise source and the ORNS, is made in Chapter 5.

4.2 Calibration of the ORNS

We saw in Section 2.1.2 that the available noise power of one-port noise sources can be modeled by an equivalent noise temperature. A common assumption with noise sources is that their available noise power equals the delivered noise power. This assumption can also be made in our case since we make use of a resistor connected to a 50-ohm transmission line with a nominal value between 47 to 50 ohms for both hot and cold states. Since the cold noise temperature is equal to the ambient room temperature, we need only to determine the hot temperature (T_h) of the ORNS for a specific environment. We emphasize that the hot temperature to be extracted is valid for a specific environment, which is described by bias current, room temperature, and the material surrounding the ORNS. Material surrounding the ORNS is important because putting a piece of insulating material between the ORNS and the chuck holding it would affect the hot temperature by altering the heat flow from the ORNS to the chuck.

A practical way to determine T_h of the ORNS is to measure it using a receiver calibrated with a known noise source. The setup shown in Figure 4.2 may be used for that purpose. Due to the nature of the ORNS, a significant advantage over a noise diode is that the determination of T_h at a single frequency is also valid for all other frequencies for the following reasons. First, we saw in Section 2.1.1 that thermal noise is constant for frequencies below 1000 GHz. Since the electronic noise generating mechanism in a resistor can only be thermal, it implies that we generate a constant available noise power spectrum up to 1000 GHz. Second, the small size of the resistor used (30x60 μm) allows us to consider it as a lumped circuit element and hence, it has a constant input reflection coefficient in the frequency band of interest (26 to 40 GHz). The calibration procedure is performed only at $f = 1$ GHz, which is the lowest calibrated frequency on the coaxial noise source available to us. Calibration at other frequencies is also possible but would result in a higher uncertainty due

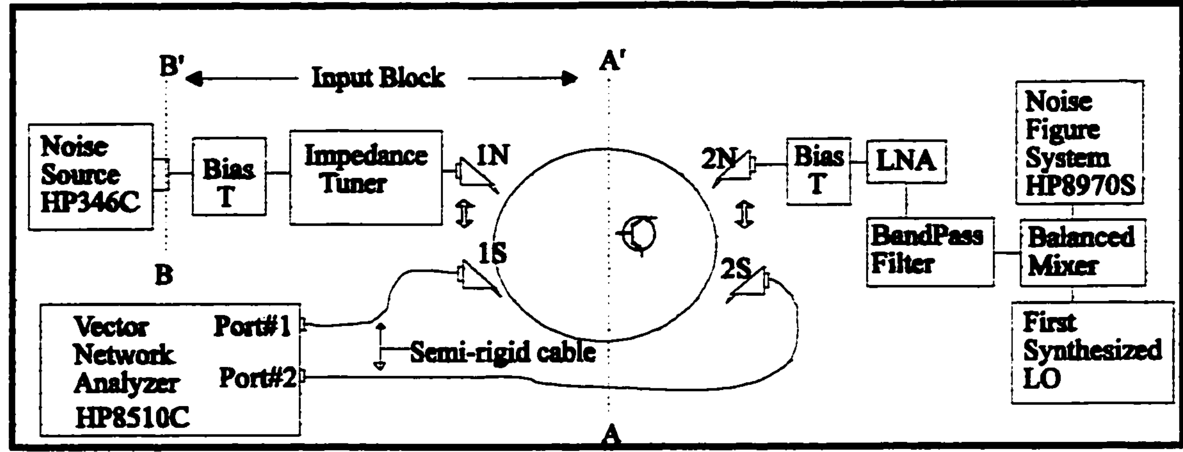

Figure 4.2 Setup for ORNS calibration

to the increasing uncertainty of S-parameter measurement with frequency. Note that better accuracy can be achieved if an isolator is used at the input of the receiver in order to reduce its sensitivity to the small input impedance changes.

4.2.1 Setup Calibration Procedure

The procedure used to determine the ORNS averaged hot noise temperature is divided into 4 steps: the characterization of the input block, the computation of the on-wafer excess noise ratio (ENR) from the calibrated coaxial noise source ENR, the measurement of the receiver noise figure, and the measurement of the averaged noise temperature of the ORNS.

We first characterize the input block between the coaxial noise source reference plane (B-B') and the on-wafer reference plane (A-A'). A 3 terminations procedure is used to determine the S-parameters of the input block by measuring the reflection coefficient at A-A' with three known standards at B-B' [67]. The mathematical foundation of this procedure can be found in Appendix Appendix D and more is said about this procedure in Section 5.3.4. We thus obtain the S-parameters of the input block (S_{in11}, S_{in21}, S_{in12}, S_{in22}) which we use to correct the value of the coaxial noise source excess noise ratio (ENR). We simplify the problem by making the approximation that T_{amb} =290K, Γ_{NS}=0, and Γ_s=0. T_{amb} is the ambient temperature, Γ_{NS} is the noise source reflection coefficient, and Γ_s is the source reflection

coefficient at reference plane AA'. From these assumptions, the ENR of the coaxial noise source is transformed to the on-wafer reference plane using [68] [11]:

$$ENR_{on-wafer(dB)} = ENR_{coaxial(dB)} - 10\log_{10}\left(\frac{\left(1 - |S_{in22}|^2\right)}{|S_{in21}|^2}\right). \quad (4.1)$$

Using the definition of ENR given in Eq. (3.1), we can now compute the corrected on-wafer hot noise temperature (T_{hco}) with the assumption that $\Gamma_{NSh}=0$. We then simply have to measure the noise powers (N_2 and N_1) for both states of the coaxial noise source. The receiver noise factor at the on-wafer reference plane (F_{rcvr}) is obtained using Eq. (3.2) with $Y=N_2 / N_1$ and $T_h=T_{hco}$.

Once the receiver noise factor is known, we simply need to probe the ORNS, and measure its Y-factor ($Y_{ORNS}=N_{2ORNS} / N_{1ORNS}$) for some specific bias condition. The hot noise temperature of the ORNS is then given by:

$$T_{h(ORNS)} = T_0 + T_0 \cdot (F_{rcvr} \cdot (Y_{ORNS} - 1)). \quad (4.2)$$

Once $T_{h(ORNS)}$ is known, we can use it to measure the receiver noise factor for any other frequency at the on-wafer reference plane. Table 1 presents measured hot temperatures at 1 GHz for six different DC bias currents. The ORNS is a standard Cascade Microtech calibration resistance. Note that we did not select a DC trimmed resistor since they present a non uniform surface which would increase current density in some areas of the resistor. Although the DC trimmed resistor produces the desired phenomenon, the higher current density may cause accelerated degradation and even failure of the resistor. The selected thin film resistor had a value of 49Ω and was estimated to drop to 48Ω for a DC current of 124.68 mA.

DC Current (mA)	20.45	40.90	61.56	82.33	103.36	124.68
T_{hORNS} (K)	293	313	343	396	466	572

Table 1: ORNS extracted temperature (T_h) for specific DC bias current

4.2.2 Discussion on Measured Temperature for the ORNS

Although the hot noise temperature achievable with the ORNS is about 10 times smaller in magnitude than that of coaxial noise diode, the difference between the hot and cold state temperatures of the ORNS is in the same order of magnitude as that of the primary standards used to calibrate the coaxial noise diodes.

At a single frequency, the relative accuracy of the hot temperature extracted with this method cannot be better than that of an on-wafer referenced coaxial noise source. From the specified relative accuracy of the coaxial noise source and an estimate of the 3 termination calibration procedure at $f = 1$ GHz, we estimate that the relative accuracy of the available hot noise temperature is ±5% (or 0.2 dB on the ENR). Substantial improvements to the accuracy is believed possible through a complete thermal analysis of the ORNS. This analysis is not within the scope of this thesis.

The reader may notice that we measured the change in resistance caused by the applied DC voltage to be approximately 1Ω for a current of 125 mA. It may be possible, through the thermal analysis, to relate the temperature coefficient of resistance, the applied DC bias, the change in resistance, and the equivalent hot temperature. By obtaining such a relation, the hot temperature for a resistor could be directly obtained from a simple measurement of the change in resistance.

4.3 Receiver Noise Figure Measurements

To demonstrate the usage of the ORNS, we performed noise figure measurements of the receiver with a calibrated coaxial noise diode and with the ORNS. The setup of Figure 4.2 is

used. The receiver noise figure is measured 4 times. First we measure it at the coaxial noise source reference plane (i.e. no de-embedding of the input block). Second, we make use of Eq. (4.1) to get the receiver noise figure at the on-wafer reference plane with the coaxial noise diode. Third, we measure the receiver noise figure with the ORNS at the on-wafer reference plane with a DC bias of 125 mA. Fourth, we measure the receiver noise figure with the ORNS at the on-wafer reference plane with a DC bias of 103 mA. With the ORNS, the hot noise temperature obtained in Section 4.2.1 is used. All these measurements are performed from 8 to 18 GHz and then from 26 to 40 GHz. The availability of test equipment dictated the selection of these frequencies.

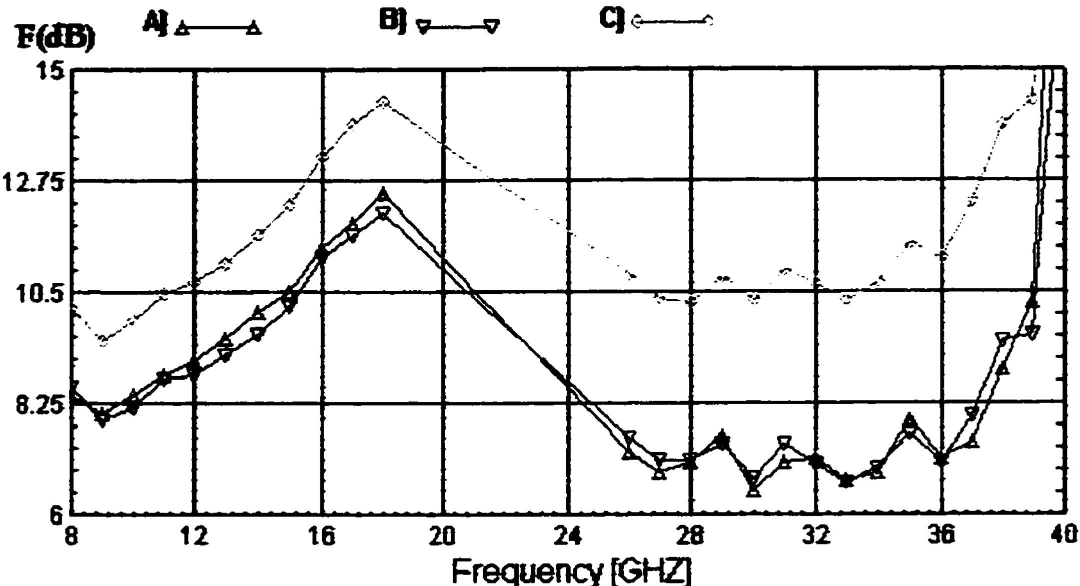

Figure 4.3 Receiver noise figure with a)ORNS biased at 103.36 mA b) Coaxial noise source corrected to on-wafer reference plane c) Uncorrected coaxial noise source

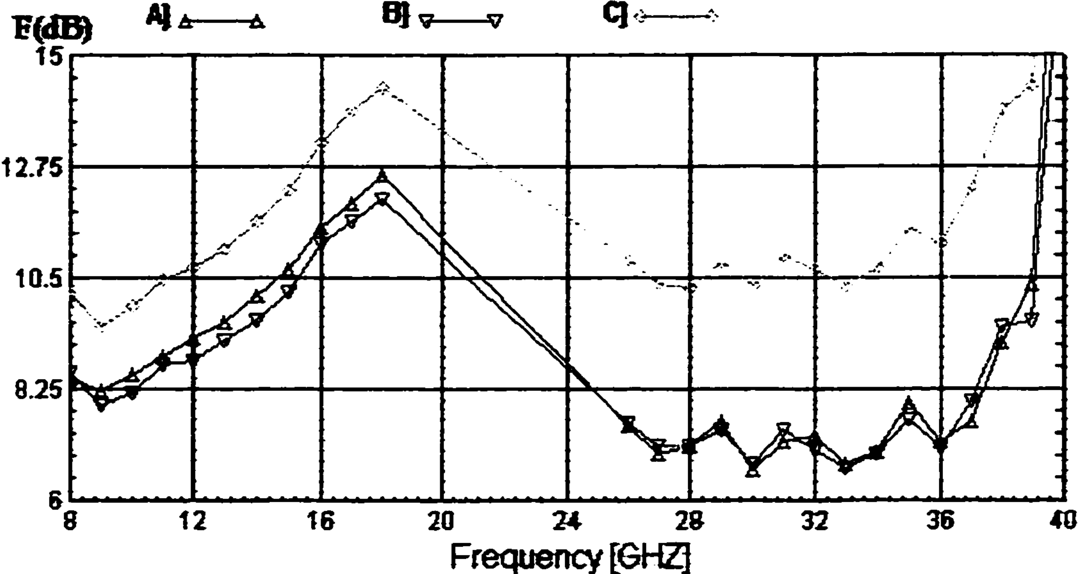

Figure 4.4 Receiver noise figure with a)ORNS biased at 124.68 mA b) Coaxial noise source corrected to on-wafer reference plane c) Uncorrected coaxial noise source

All the results are presented in Figure 4.3 and Figure 4.4. In both graphs, curves B) and C) are obtained from the same data. Curve A) of Figure 4.4 shows the result for the ORNS biased with a DC current of 125 mA and curve A) of Figure 4.3 shows the result for the ORNS biased with a DC current of 103 mA.

In both graphs, the measurement with the ORNS (curve A)) and the coaxial noise source de-embedded to the on-wafer reference plane (curve B)) track each other very well. The difference between the two never exceeds 0.5 dB but what is most outstanding is the fact that the difference between the measured noise figure with the ORNS biased at 125 mA and biased at 103 mA is always less then 0.1 dB (or 2 %) at all frequencies. Also, as expected from the increase of available loss of the tuner with frequency, we can distinguish a small increase in the gap between the noise figure at the coaxial noise source reference plane (curve C)) and the on-wafer reference plane (curve A)and B)) with increasing frequency.

The difference between the receiver noise figure measured with the ORNS and measured with the coaxial noise source corrected to the on-wafer reference plane are mainly attributed to the uncertainty on the calculated on-wafer ENR. More details on uncertainties are given in Chapter 7. The potential of the suggested noise source is therefore demonstrated. The apability of the ORNS to completely replace the coaxial noise source in the measurement of receiver and DUT noise parameters is demonstated in Section 6.3.2.

4.4 Conclusion

A novel on-wafer resistive noise source (ORNS) was presented in this chapter. Demonstration that it could be used for receiver noise figure measurements was made. This noise source has a tremendous potential to enhance and simplify on-wafer noise parameter measurements. The practicalities of the noise source are:

- its simplicity,
- the need for calibration at only one frequency,
- unlimited number of calibrated frequency,
- extremely wide band of operation,
- generation of more then one hot noise temperature, and

- elimination of the requirement for tuner de-embedding at millimeter waves.

Finally, further investigations of the noise source by performing thermal analysis may reveal that increased accuracy may be easily obtained at a very minimal cost.

5. Development of a Microwave Noise Parameter Measurement Setup

The goal of this chapter is to present the development of our custom noise parameter measurement setup. This setup is one of the original contributions of this thesis. The selection of a measurement methodology and the design of a custom on-wafer probing station are explained. The calibration techniques and procedures used are detailed. Since many things can go wrong when performing noise measurements, we also propose some verification steps and many cautions to eliminate sources of errors as much as possible. The main challenge here is to develop a setup which can provide sufficient accuracy from 26 to 40 GHz.

5.1 Selection of the Measurement Methodology

In Section 3.3, we presented two measurement techniques, the cold power technique and the hot/cold technique. A brief discussion of these two techniques follows.

We recall that a limitation on the accuracy with the hot/cold technique involves the characterization of the input block noise parameters (or available gain) for the tuner when it is presenting a high reflection coefficients. An error of at least ±0.1 dB on the available gain measurement with the tuner presenting a reflection coefficient of magnitude 0.7 [60] was mentioned. This error translates to an additional uncertainty of ±0.1 dB on the noise source ENR as can be computed from Eq. (4.1). The final impact on the extracted noise parameters of the DUT is difficult to predict since it is influenced by the DUT, the frequency and more importantly the constellation selected. We emphasize that this is not a limitation with the cold power technique. The cold power technique requires only one measurement with the noise

source in its hot state. Hence, the available loss of the input block (approximately equal to its noise figure) needs to be characterized at only one state of the tuner. To obtain better accuracy, the logical choice is to select the tuner state that resembles a low loss transmission line.

On the other hand, the cold power technique requires the noise receiver to provide a very stable gain bandwidth for the duration of the measurement. This is not a limiting requirement for the hot/cold technique since measurement of the hot and cold power for every impedance used includes the measurement of the receiver gain bandwidth. Increased accuracy relating to the receiver stability is possible by controlling the ambient temperature, or by correcting for the drift [69]. Limiting the duration of the measurement can also minimize the effect of receiver drift.

In addition to the above, other arguments such as simplicity of the measurement procedure, the total number of connections and disconnections required during the measurements, the availability of equipment, and the possible future use of on-wafer resistive noise sources make the cold power technique more suitable than the hot/cold technique at millimeter waves. The custom setup developed is therefore specific to the cold power technique from 26 to 40 GHz. However, the probing station developed for our setup can also accommodate the use of the hot/cold technique. A description of the setup and selection of its components is presented in detail in the following section.

5.2 Description of the Measurement Setup

A block diagram of the noise parameter measurement setup is shown in Figure 5.1. A collection of pictures showing the complete system and the custom probing station is presented in Appendix Appendix F. We can break up this setup into the following functional sub-assemblies:

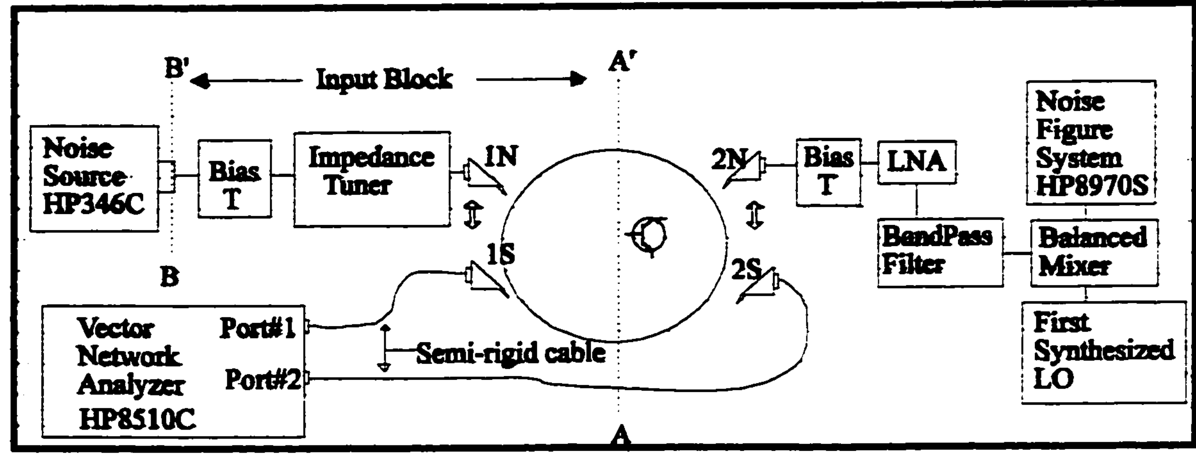

Figure 5.1 Block diagram of the noise parameter measurement setup

- the source impedance tuning sub-assembly,
- the custom on-wafer probing station sub-assembly,
- the noise figure measurement sub-assembly,
- the S-parameters measurement sub-assembly, and
- the DC bias circuit sub-assembly.

Details of each sub-assembly are presented in the following sub-sections.

5.2.1 The Source Impedance Tuning Sub-assembly

A major component of the setup is the impedance tuner. Two classes of tuner are generally used. They are the electronic impedance tuner and the mechanical slide-screw tuner. The first class is generally built from PIN diode switching impedance transformers. They provide fast switching between impedances, a limited number of tunable impedances, small size and significant losses above 26 GHz. The second class provides a very large number of tunable impedances, low loss, slow tuning between impedances and a large physical size. Our choice for this component is dictated by the availability of the computer controlled microwave tuner (CCMT) developed by Focus Microwave Inc. . The CCMT, shown in Figure 5.2, is built from a slab line and a specially developed plunger to provide a tuning bandwidth from 6 to 40 GHz. The plunger is controlled by two accurate stepper motors to provide two degrees of

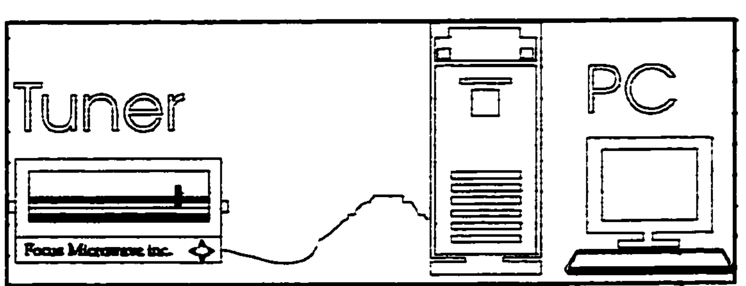

Figure 5.2 The Source Impedance Tuning Sub-Assembly.

freedom. The generated impedance increases in magnitude as the plunger approaches the center conductor of the slab line and changes in phase by laterally moving it along the transmission line. The maximum magnitude of the generated reflection coefficient is greater than 0.8 over the complete bandwidth. The repeatability of the reflection coefficient generated is specified to be better than 40 dB (1 %). Virtually any impedance can be generated inside the radius of 0.8 by properly selecting the plunger position. Standard calibration constellations of 101, 202 or 404 impedances uniformly distributed over the Smith chart are generated by the software [70]. Smaller constellations can then be selected from the original calibrations.

This sub-assembly also includes the tuner controlling software and interfaces which run on the Windows® operating system. The Tuner for Windows (TWIN[2]) software is the user interface to control the tuner and acquire data from the general-purpose interface bus (GPIB) of remotely controlled test equipment. Data analysis and display routines are also available with TWIN.

5.2.2 Custom On-Wafer Probing Station Sub-Assembly

We saw in Section 3.4 reasons for using on-wafer probing over test jigs. Unfortunately, the bulkiness of the CCMT tuner doesn't allow direct connection of the tuner to commercially available on-wafer probing stations. A flexible cable would normally be used to interconnect

---

[2] TWIN was developped by Focus Microwave Inc.

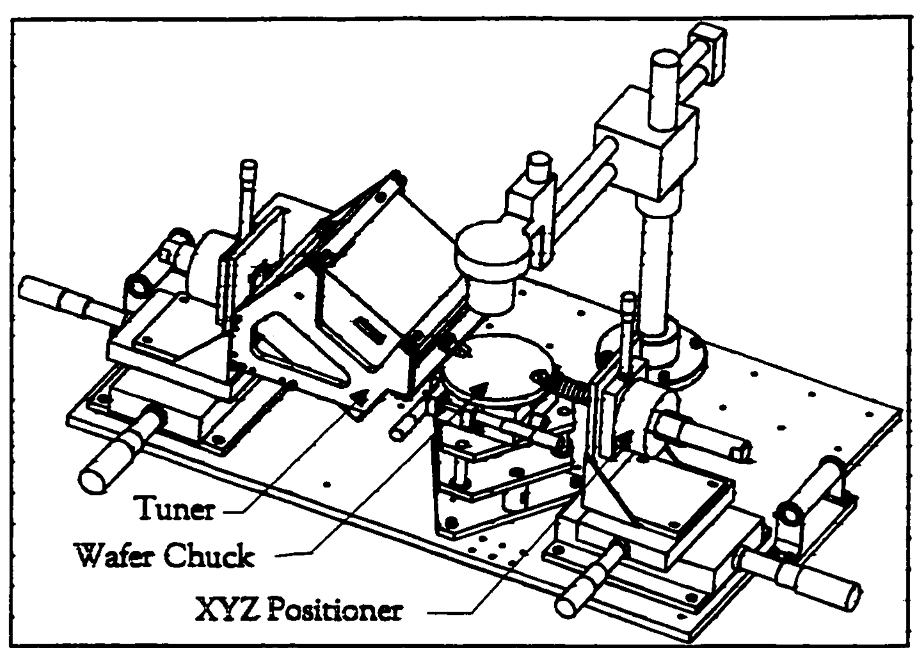

Figure 5.3 Custom on-wafer probing station

the tuner to the probe. However, the associated loss considerably diminishes the Smith chart coverage of the tuner already limited to a maximum magnitude of 0.8 at 40 GHz. For example, 2 dB of loss would limit the coverage from magnitude 0.8 to 0.65. For noise parameters measurements, this may result in a significant lack of accuracy. In addition, motion of the probe is required to perform the on-wafer S-parameters calibration. A solution to both these requirements was analyzed. We chose to design a custom on-wafer probing station. The design which optimizes the achievable Smith chart coverage is an achievement of this thesis. A drawing of the probing station built at the Communication Research Centre is shown in Figure 5.3.

The probing station features an adapter between the input XYZ micro-positioner and the tuner. A Cascade Microtech ultra low loss Air Coplanar Probe (ACP 40-L) is directly connected to the tuner with a K-male to female adapter. The tuner is connected upside down to clear the field of view of the microscope. A microscope with 100X magnification and 10 cm focal length is required for the alignment of the probe with the devices probing pads. The

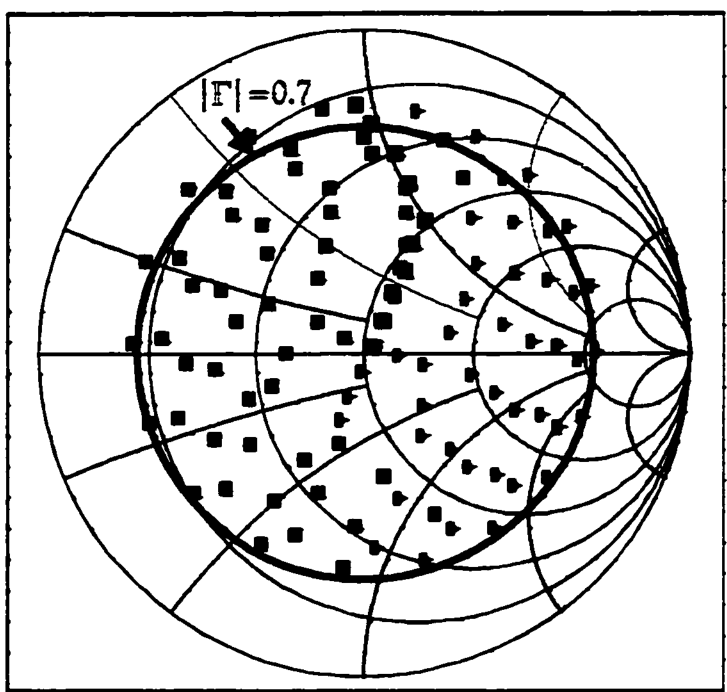

Figure 5.4 Smith Chart Coverage at 40 GHz

wafer chuck is built with three degrees of freedom to give more flexibility with the device alignment procedure.

Another feature of the probing station is the capability to support two parallel probes at the input and at the output. We number these probes as port 1S, 2S, 1N, and 2N which correspond to ports 1 and 2 of the S-parameter circuit (1S, 2S) and ports 1 and 2 of the noise parameter circuit (1N, 2N) respectively. Making use of four probes eliminates the need for RF switches or connecting and disconnecting components. We thus improve the repeatability of the system since only the probing contact is changed during our measurement procedure. Note that our chuck doesn't have a vacuum to hold the devices in place. We also use a small spacing plate of 2x4x0.25 mm to raise the probing pads from the level of the chuck. This was the easiest way we found to safely make electrical contact when using two probes on the same XYZ positioner.

The main advantages of using our custom probing setup are enhanced repeatability and a better Smith chart coverage. The Smith chart coverage achieved at 40GHz is shown in Figure

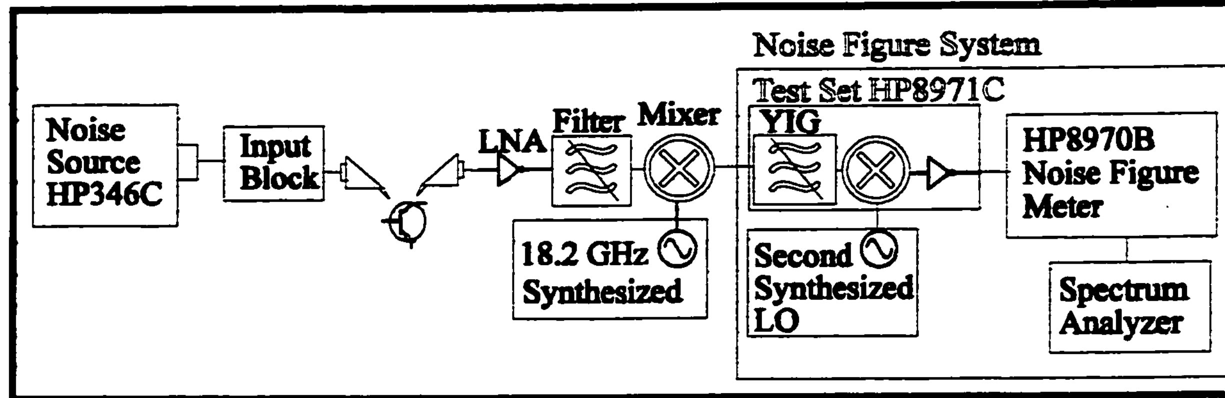

Figure 5.5 Block Diagram of the noise figure measurement sub-assembly

5.4. We can observe that the impedance constellation provides a greater coverage magnitude on one side of the Smith chart than the other. The location of the maximum is rotating as a function of the frequency of calibration for this specific setup. This phenomenon is expected for a non ideal slide screw tuner [18].

5.2.3 Noise Figure Measurement Sub-Assembly

A block diagram of the noise figure circuit is shown in Figure 5.5. This circuit is capable of on-wafer single side band noise figure measurements from 26 to 40 GHz. The noise figure measurement circuit is composed, at the input, of the HP346C K01 noise source which has calibrated ENR at every frequency from 1 to 50 GHz. On the receiver side we first have a 26 to 40 GHz low noise amplifier (MITEQ AMF-5D-260400-10-10P), a waveguide bandpass filter from 26 to 40 GHz, a double balanced mixer (WJ-SMC1844) driven by a synthesized local oscillator at 18.2 GHz, the Hewlett Packard 2-26 GHz noise figure measurement system which is composed of the HP8971C, the HP8970B and synthesized local oscillator source. A spectrum analyzer is also connected to the noise figure meter to monitor spurious signals.

Let us discuss some important considerations when selecting the components of the noise figure sub-assembly. First of all, a good noise source is one that provides sufficient ENR at the DUT reference plane, has a very small change in reflection coefficient from the cold to the hot states, and is accuratelly calibrated.

Next, the noise figure of the receiver must be kept small or the DUT gain must be kept high. We saw in Section 3.1.2 that the noise figure of a DUT is obtained from the Friss equation. The Friss equation relies on the subtraction of the receiver noise figure divided by the gain of the DUT from the total noise figure measured. Hence, relative uncertainties are dramatically increased when the receiver noise figure is high compared to the DUT noise figure and when the gain of the DUT is small. The requirement for low receiver noise figure is especially challenging above 26 GHz since every microwave component inserted between the output of the DUT and the receiver low noise amplifier has significant loss which degrades the receiver noise figure. Also the DUT's gain above 26 GHz is on a decreasing slope as a function of frequency. Guidelines are provided in [38] to determine if the receiver noise figure is low enough to provide sufficient accuracy. In our case, slightly better accuracy could be achieved by reducing the receiver noise figure.

A band pass filter with sufficient out of band attenuation is inserted before the balanced mixer for single side-band measurement. A balanced mixer is used because it provides better isolation from the local oscillator noise, which is converted into the measurement band. The first local oscillator is selected as a synthesized source to provide good frequency stability and low noise floor. A 2 to 26 GHz noise figure measurement system is then used to provide more filtering, frequency conversion, and power measurement. It is also useful to have a spectrum analyzer in order to detect any spurious signal which may fall in the noise power measurement band. In fact, the spectrum analyzer is essential for the frequency alignment procedure described later.

Finally, care must also be taken not to saturate any of the amplifiers in the receiver chain. Small non-linearities in the noise receiver would introduce errors in noise power measurements which could not be easily detected.

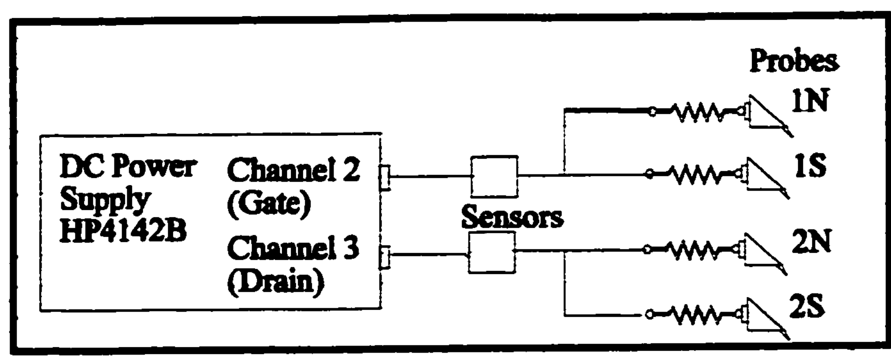

Figure 5.6 DC Bias diagram

5.2.4 S-parameter Measurement Sub-Assembly

The S-parameter measurement circuit is composed of the Hewlett Packard HP8510C vector network analyzer (VNA) capable of on-wafer TRL calibration and capable of transferring measured data through its GPIB interconnect. The VNA port #1 and #2 are connected via two 3-foot semi-rigid K cables to probe 1S and probe 2S respectively. Semi-rigid cables were found to provide the best accuracy for S-parameter measurements while keeping sufficient flexibility to move the probes. We should point out that the use of the VNA directly connected to the probes provides better calibration accuracy than if it was connected through two switches. Although the improvement may seem insignificant when comparing the S-parameters, it can result in a significant improvement when looking at the noise parameters. This statement is confirmed by the uncertainty analysis performed in Chapter 7.

5.2.5 DC Biasing Circuits

DC biasing to the on-wafer device is accomplished by using two channels from the HP4142 power supply. The DUT gate bias voltage is applied to the on-wafer probe 1S and 1N from the HP4142 channel 2. The DUT drain bias voltage is applied to the on-wafer probe 2S and 2N from the HP4142 channel 3. The VNA HP8510C internal bias tees are used to feed the bias through the RF cables to probe 1S and 2S. Two other bias tees are inserted in the noise

figure measurement circuit to feed the bias trough probe 1N and 2N. The bias to probe 1S and 1N, as well as 2S and 2N are connected in parallel as shown in Figure 5.6.

5.3 Calibration Procedure

Defining and assembling the setup is just the first step to take in making noise parameter measurements. This section describes the measurement procedure partitioned in 9 steps. The actual operation of the test equipment is not covered here since it can easily be found in the operation manual of each system component. The procedure and associated parameters obtained from each part are:

- the bias circuit resistance measurement which yields: R_{1N}, R_{2N}, R_{1S}, and R_{2S} (Figure 5.6),
- the frequency alignment of the VNA and receiver which yields (f),
- the on-wafer S-parameter calibration which yields the DUT S-parameters (S_{D11}, S_{D21}, S_{D12}, S_{D22}) (Figure 3.6, reference plane AA'),
- the 3-termination calibration which yields the S-parameter of the input block (S_{in11}, S_{in21}, S_{in12}, S_{in22}) (Figure 5.1, input block),
- the receiver reflection coefficient measurement which yields the receiver reflection coefficient (Γ_L) (Figure 5.1, from ref.plane AA' and looking towards probe 2N),
- the tuner calibration which yields the constellation of source reflection coefficients (Γ_{Si} , i=1..N), (Figure 5.1, from ref.plane AA' and loking towards probe 1N),
- the receiver calibration which yields the noise power (P_{nj} j=1..m) associated with each Γ_{Si}, the hot noise power (P_{nh}), and the room temperature (T_c),
- the DUT cold power measurements which yields the noise power (P_{nj} j=1..N) associated with each Γ_{Si} when probing the DUT, and the last step being
- the selection of source impedance constellation.

The parameters of the above list are used to compute intermediate parameters such as DUT available gain, input block available gain, receiver gain bandwidth constant, and receiver noise parameters. Lastly, the DUT noise parameters can be extracted for a selected constellation. Almost every parameter in the above list may have a significant impact on the extracted noise parameters of the DUT if it is not properly measured. The procedure is detailed in the following sub-section to provide one approach to the measurement. Some cautions and verification steps are also included to avoid common pitfalls.

5.3.1 Bias Circuit Resistance Measurement

Our goal here is to verify the proper operation of the DC biasing circuit and to correct for changes in resistance between the S-parameter circuit and the noise measurement circuit when required. The procedure consists in probing on short circuit elements to measure the resistance from the sensor to the tip of the probe. The internal DC resistance of each probe circuit is then calculated from R=V/ I and is reported in Table 2.

	Voltage (V)	Current(mA)	Resistance (Ω)
Probe 1N (R_{1N})	0.010	17.33	0.577
Probe 1S (R_{1S})	0.010	3.75	2.67
Probe 2N (R_{2N})	0.010	14.27	0.701
Probe 2S (R_{2S})	0.010	2.93	3.41

Table 2 Bias circuit measured resistance

5.3.2 Frequency Alignment of VNA and Receiver

The goal of this procedure is to minimize the difference that exists between the frequency reading of the VNA and that of the noise figure measurement circuit. The frequency accuracy of the noise figure meter is specified to be ±6 MHz [71]. With this procedure, we make sure that the S-parameters and the noise power are measured at the same frequency within ±0.5 MHz. The procedure is as follows:

- Connect a spectrum analyzer at the IF output of the HP8971B and center it at 20 MHz with scale of 1 MHz/division. You should distinguish the 4 MHz measurement band of the HP8970B noise figure meter. Perform a fine alignment of the noise figure system internal YIG filter with probe 1N and 2N sitting on a through line.
- Set the VNA to CW mode at the frequency of measurement,
- Set the noise figure system at the same frequency. Make sure that the first local oscillator frequency is configured in the HP8970B noise figure meter.
- Keep the four probes lifted in the air, radiation from the S-parameter probes are picked up by the noise receiver, and down-converted to 20 MHz. If the frequency of the VNA and the noise circuit are identical, you will see a sharp single frequency signal appearing in the center of the 4 MHz measurement band.
- Most likely, the signal will not be centered. We take advantage of the fact that we manually control the first LO to adjust the noise figure measurement system frequency. We offset the noise circuit frequency by varying the first LO frequency without changing the software configuration set in the noise figure measurement system.
- Gradually (in steps of 1 MHz) vary the relative first LO frequency until the VNA signal appears on the spectrum analyzer and center it in the middle of the 4 MHz band.
- If you have trouble finding the VNA signal, you can always put probe 1S and 2N on a through line and repeat the previous step.

This procedure is essential because Valk & *al* showed in [72] that if frequency discrepancies between the VNA and the noise figure meter are allowed to occur, they can cause significant error in the noise power measurement of highly mismatched devices such as HEMT and FET's. We limit our explanation to this comment for now, as we will further investigate the impact of frequency discrepancies and measurement bandwidth in Chapter 7.

Caution: this procedure clearly demonstrates that the VNA output signal can be picked up by the noise receiver and thus affect the noise power measurement. Hence, care must be taken to avoid this by turning off the VNA output signal.

5.3.3 On-Wafer S-Parameter Calibration

Details of a TRL on-wafer calibration are not covered here. We just want to point out that microstrip TRL calibration standards on GaAs substrate were used to provide a measurement reference plane at the DUT (AA') rather then at the probe tips (BB') as shown in Figure 3.6. The quality of the calibration was verified by making measurements of the thru line standard before and after the measurement. The S-parameters obtained had to satisfy $|S_{11}| = |S_{22}| < -40$ dB, $|S_{21}| = |S_{21}| < \pm 0.03$ dB. If these conditions are satisfied both before and after the S-parameter measurement above 26 GHz, we consider the calibration made as being of very good quality. Since all S-parameter measurements could not be made during the same day, the VNA was sometimes re-calibrated at the beginning of important S-parameter measurements. This is a good practice to follow which limits the error caused by the continual drift of the VNA components.

5.3.4 The 3-Termination Calibration for Input Block Characterization

Non-insertable two-port networks require special calibration techniques to measure their S-parameters [73]. The input block of our setup (Figure 5.1) is a non-insertable two-port because it features a coaxial 2.4 mm connector at port #1 (BB') and an on-wafer microstrip transmission line at port #2 (AA'). We recall that we need the S-parameters of the input block to precisely determine its available gain. As in Section 4.2.1, the input block is composed of passive elements, which are assumed reciprocal. Hence, we let $S_{in21} = S_{in12}$ and we make use of the 3 terminations calibration technique.

The three male terminations (i.e. the open, the short and the load) found in Hewlett Packard's 2.4 mm economy calibration kit are used to perform this procedure. All Hewlett Packard calibration kits come with a table of standard coefficients describing the termination. The reflection coefficient of the termination can thus be obtained by making use of a circuit simulator. Note that electrical models for the termination and the table of standard coefficient are explained in [74]. Any other means of getting the reflection coefficient of the 3 terminations could also be used. For example, S-parameter measurements of the three terminations could be performed. In our case, this approach provides less accuracy since we only have a 2.4 mm economy calibration kit.

After characterizing the 3 terminations, the steps to follow are:

- set the tuner as a low loss 50 Ω transmission line.
- disconnect the noise source at the 2.4 mm reference plane (B-B') (Figure 5.1),
- connect the first standard (either the open, the short or the load),
- probe on the on-wafer calibration through line with probe 1N and 2S,
- measure the reflection coefficient of the standard combined with the input block at the on-wafer reference plane (A-A') using port 2 (probe 2S) of the calibrated VNA.
- repeat the 3 previous steps for the two remaining standards.

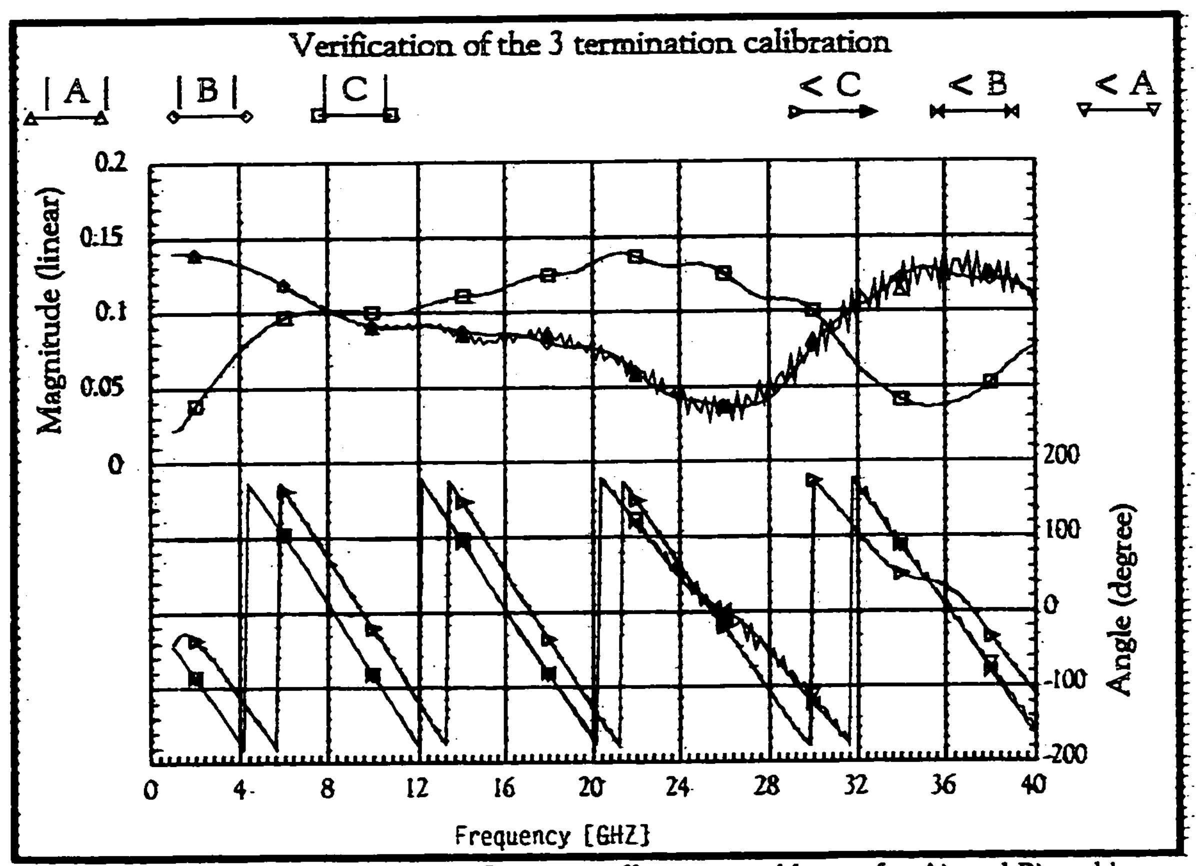

Figure 5.7 HP346C noise source reflection coefficient in cold state for A) and B) and hot state for C) . A) measurement at the on-wafer reference plane (A-A') with de-embedding of the input block S-parameters found using the 3 termination calibration, B) measurement at the 2.4 mm coaxial reference plane (B-B'), C) measurement at the 2.4 mm coaxial reference plane (B-B').

After completing this procedure, the S-parameters of the input block are computed using the equations found in appendix Appendix D. To verify that the S-parameters obtained are valid, we measure the reflection coefficient of the noise source at the 2.4 mm reference plane (B-B') (Figure 5.1, p. 48), and at the on-wafer reference plane (A-A') when it is combined with the input block. By de-embedding the input block from the on-wafer measurement (A-A'), we should obtain the same reflection coefficient as the one measured in the 2.4 mm reference plane (B-B'). This verification step was performed and the comparisons of the de-embedded and measured noise source reflection coefficient are shown in Figure 5.7. Curves A) and B) overlap which indicates good characterization of the input block. Note that this verification is being performed last. Hence the noise source remains connected to the setup until the end of

our measurements. We consider this verification step essential since any bad connection performed during the procedure could result in a wrong extraction of the input block S-parameters. It can be shown from Eq. (4.1) that the error on the input block available gain is directly added to the uncertainty of the noise source excess noise ratio (ENR). This error increases with frequency as deduced from Figure 5.7, which shows an increasing difference between curve A) and B). The use of an on-wafer noise source (ORNS) like the one presented in Chapter 4 eliminates the requirement for this procedure. Hence, the additional error introduced by increasing uncertainty with frequency is eliminated by the use of the novel ORNS.

5.3.5 Receiver Reflection Coefficient Measurement

The measurement of the receiver reflection coefficient is made by making contact with probe 1S and 2N to the on-wafer thru line. Port #1 of the calibrated VNA at the on-wafer reference plane (A-A') is used to make this reflection coefficient measurement. The measured data is then transferred to the personal computer via the GPIB interconnect.

5.3.6 Tuner Calibration

The tuner calibration is an automated procedure performed by the TWIN software. We connect probe 2S and probe 1N with the on-wafer thru line and then initiate the tuner calibration procedure. The software then steps the tuner through a set of impedances and measures the reflection coefficient presented at the on-wafer reference plane (A-A'). Port #2 of the on-wafer calibrated VNA is used here. Initially, the software measures a constellation of impedances uniformly distributed over the Smith chart. This initial constellation can have 101, 202, or 404 impedances. Other specific constellations of impedance can then be selected from this initial calibration. More is said about the selection of a specific constellation in Section 5.4.

5.3.7 DUT S-Parameter Measurement

At this point, we measure the S-parameters of the DUT for the desired bias conditions. This is achieved by probing on the DUT pads with probe 1S and 2S. The desired biasing conditions are then applied with the HP4142 power supply which is controlled via a GPIB interconnect. The bias conditions given with our results are the actual voltage and current corrected at the tip of the on-wafer probes.

5.3.8 Receiver Calibration

The receiver calibration consists in computing the four noise parameters of the receiver and the available gain-bandwidth constant (kG_aB) from measurements of the noise power (P_{ni}) for a constellation of at least four impedances and one measurement of the hot noise power (P_{nh}). Automation of noise power measurements by the use of a noise figure meter greatly simplifies this procedure. Comments on the noise figure meter linearity, on possible pick up of undesired signals and on software configuration is necessary to eliminate many pitfalls

To use the cold power technique, we use a noise figure meter as a bandwidth limited accurate power meter. In fact, the noise figure meter always provides measurements of power at a specific frequency over a bandwidth of 4 MHz. Hence, if we measure a noise signal at frequency f, then the noise figure meter will measure the relative noise power over a bandwidth of 4 MHz with f being the centre. Over short period, the noise powers fluctuate due to the random nature of the signal. We know that the signal measured is described by a truncated stationary ergodic Gaussian process. Thus, increased accuracy of noise power measurement is achieved by increasing the measurement time or by making N successive measurements. Because we have a Gaussian process, taking N measurements results in an increase of accuracy by a factor equal to $\sqrt{N}$. Therefore, time and accuracy are a trade off to consider when making noise power measurements.

Accuracy is also affected by the linearity of the receiver used. We previously mentioned that it was important not to saturate any amplifier in the noise receiver chain. This is true for the internal amplifier of the noise figure meter also. The HP8970B has three internal RF attenuators, one RF amplifier, one IF amplifier, and seven settings for IF attenuators which are automatically switched in and out of the signal path. The noise power meter must be calibrated for every possible attenuator setting in order to give valid relative noise power. Verification that this is the case should be made before making cold noise power measurements in the automatic mode. If the calibration is not valid, it is possible to still obtain valid results by manually selecting and keeping track of the internal attenuators and amplifiers settings. This is the approach we took for our measurements.

Erroneous noise power measurements are sometimes made due to the high probability of picking up unwanted signals. The power meter cannot distinguish between the noise signals you want to measure and other signals you may receive. The spectrum analyzer used in 5.3.2 is very helpful in detecting such unwanted signals and therefore we recommend its use for every noise power measurement.

Proper operation of the test equipment is complicated by the large number of possible configurations it can support. Guidelines for setting the software parameters and properly using many of the features of the Hewlett Packard microwave noise figure measurement system can be found in [75]. The main parameters we had to set are: variable IF, fixed frequency LO (SF 1.7), single side band, upper single side band, less resolution on gain, arithmetic averaging and smoothing factor=64.

Finally, the noise power measurements are made using TWIN [67]. A description of the setup used must first be configured in TWIN to allow remote control of test equipment through the GPIB interconnects.

After considering all of the above, the hot power and the cold power measurements for the complete constellation of impedances can be automatically performed. TWIN then computes the receiver noise parameters and the gain bandwidth constant from the raw data measured. The raw data is also available in ASCII file which we use later for some of our calculations.

The receiver being characterized, the setup is ready to measure noise parameters of two port circuits. The use of a pasive components, for which noise parameter can be computed from S-parameter measurement only, is useful at this point to verify the operation of the measurement setup. The on-wafer calibration thru line was used for that purpose in our case. The use of the thru line over other passsive two ports is convinient since it is available from the on-wafer calibration kit.

5.3.9 DUT Cold Power Measurements

After calibrating the receiver, and saving the information in an ASCII file, we are ready to probe a DUT and measure the set of cold powers associated with the selected constellation. This procedure is performed immediately after the receiver calibration to limit the possible drift of the gain bandwidth. With a constellation having at least four impedances, we can compute the noise parameters of the DUT. TWIN automates the measurement of a complete constellation and saves the raw data as well as the extracted noise parameters in an ASCII file. If we have the time we make the measurement for all calibrated (101, 202 or 404) source impedances. The extracted noise parameters are seldom valid in these cases due to the unstable behavior of the DUT at some of the impedances presented. Unfortunately, the impedances causing instabilities are not detected by the software and must be manually identified. Nevertheless, making the measurement for all calibrated impedances provides more flexibility for impedance selection as will be discussed in the next section.

5.4 Selection of Source Impedance Constellation

Selection guidelines that we introduced in Section 3.2.3 are gathered here as a number of criteria to consider. Our criteria can be summarized in three words: ill conditioning, instability and uncertainty. Each criterion is presented and explained in the following paragraphs.

The first criterion to consider is ill conditioning of the matrices. We saw in 3.2.3 that a bad selection of impedances can cause ill conditioning of the matrices to be solved for the extraction of the noise parameters. O'Callaghan makes a significant contribution in [44] by presenting a simplification in handling the ill condition problem and by quantifying the degree of ill condition of a specific constellation. His technique was therefore partially implemented to make a more in depth analysis of our noise parameters than by just looking at results provided by TWIN which implements Lane's algorithm.

Instability at specific impedances is our second criterion: A specific tuner position may cause oscillation of the DUT. Careful monitoring of power measurement is required to detect impedances that cause the DUT to oscillate. Oscillation will commonly drive the DUT into saturation and therefore change its characteristics. In those cases the measured noise power will have no meaning for us. Even if the DUT is known to be unconditionally stable at the measurement frequency from its S-parameters, oscillation could still be caused by out of band oscillation. We systematically eliminate impedances from our constellation showing signs of invalid cold power measurement. Some signs of oscillations are:

- a change in the bias applied to the DUT caused by sudden saturation of the DUT, it is easily detected by a drain current change (Ids),
- an unexpected drop of the cold noise power measured, this is caused by the oscillation signal, usually at a different frequency then the measurement frequency,

saturating the noise receiver and thus reducing its gain-bandwidth constant. Reductions by as much as 10 dB was observed.

- detection of a spurious signal on the spectrum analyzer display connected to the HP8970B 20 MHz IF output.

Uncertainty on measured parameters is our last criterion. Accuracy of many measured parameters is a function of the source impedance. This is a topic which is not completely covered in this thesis due to the complexity of the problem. Discussion about uncertainties are made in Chapter 7 and could be a starting point to evaluate the impact it may have on the selection of the source impedances.

We try to benefit from the capability of our measurement system to generate a large number of source impedances in the following way. We recall that 404 source impedances can be generated for a single constellation at one frequency. In reality, measuring 404 points takes approximately 30 minutes to first calibrate the system and then approximately 60 minutes to measure the associated cold powers for each frequency of interest. Our limited access to the test equipment constrained us to limit ourselves to 101 impedances at most frequencies measured except at 30 GHz were we measured the complete set of 404 impedances.

During our measurements, the extraction of noise parameters is performed more than once. We first use TWIN to measure all 101 source impedances. If there is no oscillation, we may be able to compute the noise parameters from Lane's algorithm implemented in TWIN. Next we re-measure a constellation of 9 points arranged in a well spread cross similar to that of Figure 3.3. The cross varies from frequency to frequency because we make use of the specific set of 101 impedances calibrated at each frequency. If there is no oscillation, we may again be able to extract valid noise parameters from Lane's algorithm. Finally, we analyze all this data using

our implementation of O'Callaghan's algorithm in MMICAD[3]. The selection of a new set of 9 impedances is again made before performing the extraction of the noise parameters. Of all extracted parameters, the last set provides the best continuity over the frequency band. It also provides the smallest difference between the measured noise figure and the computed one from the noise parameters extracted. A good fit between measured and extracted noise figure for all source impedances indicates a better result when the constellation encloses the optimum impedance (Γ_{opt}). Only the noise parameters obtained from the last extraction are presented in Chapter 6. Details about O'Callaghan's algorithm can be found in Appendix Appendix C.

5.5 Conclusion

This concludes the presentation of the millimeter wave noise parameter measurement setup developed. The original contributions introduced here are: the mechanical tuner directly mounted on an ultra low loss air-coplanar probe, the use of four probes instead of switches, and the actual millimeter wave frequency band covered. From these improvements over other existing systems, we expect to provide measurement capability from 26 to 40 GHz with at least the same accuracy as that commonly achieved at lower frequencies.

---

[3] MMICAD is a microwave circuit simulator developped by Optotek Inc.

6. Noise Parameter Measurements

The aim of this chapter is to present noise parameters measured with the procedure and setup described in Chapter 5. We first present typical values of S-parameter and noise power measurements since they are the basis for the extraction of noise parameters. The availability of PHEMT devices with a potential for LNA design at 30 GHz determined our selection of the DUT. We characterized the DUTs for their noise behavior as a function of bias and frequency to relate the measured noise behavior to the general trend expected from noise models. A certain degree of confidence in the measurements can thus be obtained if the measured data follows the trend predicted from theory. Further confidence is also obtained by measuring the same DUT on an independent measurement system at the cross over frequency of 26 GHz. Finally, a comparison of the noise parameters extracted with the noise diode and the ORNS are also made to further demonstrate the potential of the ORNS.

6.1 Intermediate Parameters

We refer to bias, S-parameters and noise power as intermediate parameters. These parameters are specific to the device being measured. Changes in these parameters for different devices can have a different impact on the accuracy of the noise parameter measurement setup. We therefore select one type of device and limit the scope of our study to this specific case. The selection of two PHEMT devices located in reticule R4C20 and R1C14 of the COMSAT wafer run number 6053152803 (CRC M951C) was made. We refer to these devices as DUT X (R4C20) and DUT Y (R1C14). The intermediate parameters measured for DUT X and DUT Y are presented in the following sub-sections.

6.1.1 Bias

The biasing conditions of FET devices are given by the drain to source voltage (Vds), the gate to source voltage (Vgs) and the drain current (Ids). Values for gate current are not given since the devices have a very small input current (about $1x10^{-6}$A for PHEMTs) which is difficult to measure. Table 3 provides the biasing conditions of DUT X and Y. The column X5 indicates DUT X biased at 5 mA. Biasing is first applied to the gate and then to the drain. The value of Vgs is then gradually adjusted to obtained the desired drain current. We note a difference of ~0.1 Volt on Vgs which is caused by the channel depth variation from device to device on the same wafer. Take note that the drain to source voltage (Vds) is corrected for voltage drop caused by the series resistance in the biasing circuit as explained in Section 5.3.1.

	X5	X10	X15	X20	Y5	Y10	Y15	Y20
Ids(mA)	5.0	10.0	15.0	20.0	5.0	10.0	15.0	20.0
Vgs (V)	-0.3053	-0.2142	-0.1395	-0.0715	-0.4364	-0.3305	-0.2416	-0.1580
Vds (V)	2.0	2.0	2.0	2.0	2.0	2.0	2.0	2.0

Table 3: PHEMT bias conditions.

6.1.2 S-Parameters

DUT X and Y are embedded with a microstrip transmission line as shown in Figure 3.6, p. 32. The S-parameters for each bias condition are measured using the TRL calibration technique. Results for both DUTs at each bias condition are presented in Figure 6.1. We observe that the input reflection coefficient (S_{D11}) suffers from a variation with frequency having changes in magnitude in the order of 0.01 (1.5%). This kind of response is common with VNA. The amplitude of this variation is governed by the VNA's accuracy specification, the quality of the calibration standard used, the ability of the operator, and the magnitude of the reflection coefficient measured. You may see from the result for S_{D22} in Figure 6.1 that the variation is not apparent in this case. Establishing the accuracy of a specific S-parameter measurement is very complex and out of the scope of this thesis. We note as well a remarkable resemblance between all the curves for the two devices at all biasing conditions. This is an indication of

excellent measurement repeatability, which should not be confused with the measurement accuracy. Finally, the difference between DUT X and Y can be attributed to process variation during the production of the wafer.

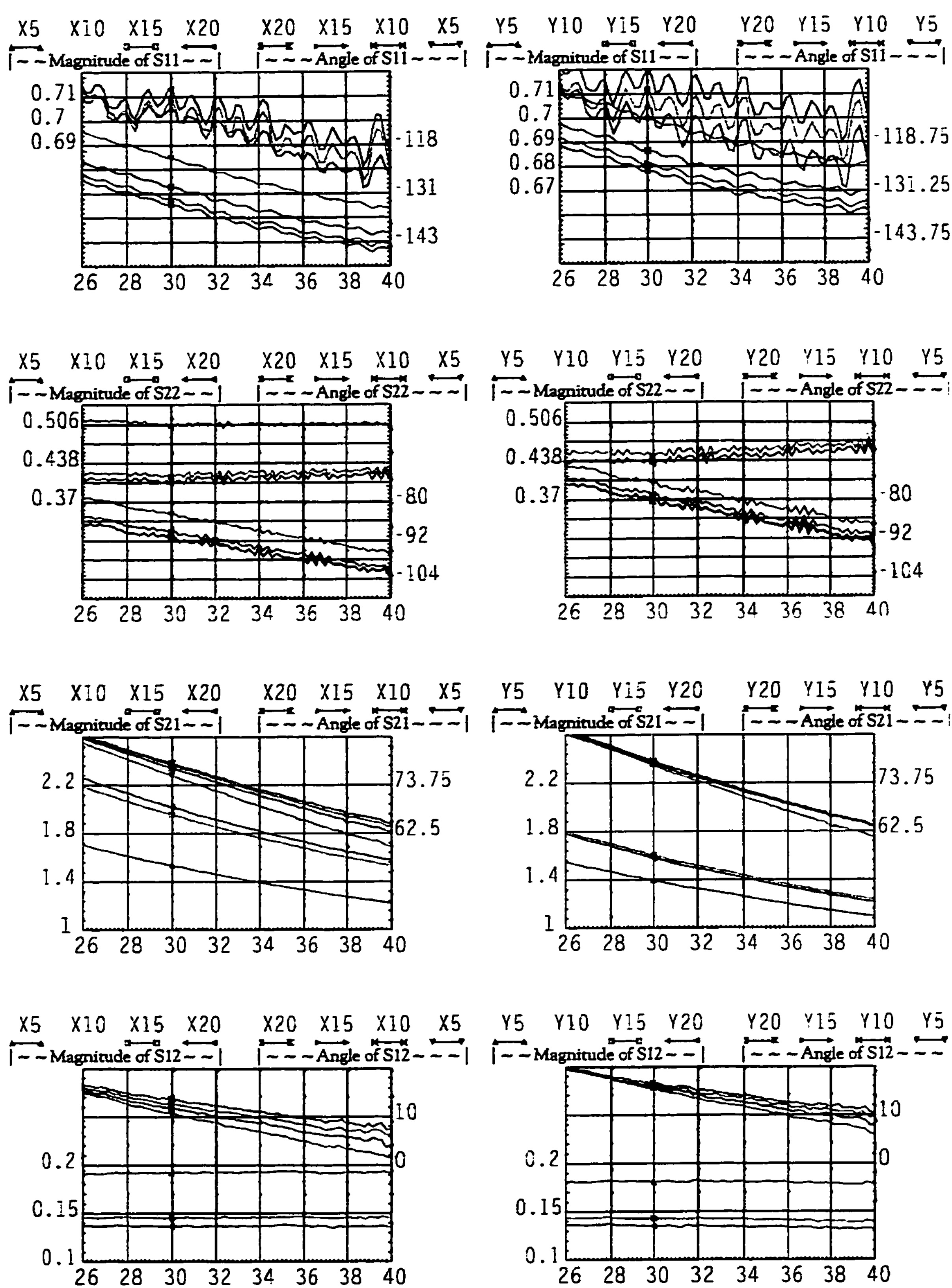

Figure 6.1 S-parameters from 26 to 40 GHz of DUT Xi and Yi where i is the drain current (Ids) in mA

6.1.3 Noise Power

Noise power measurements of the DUT/receiver chain as a function of source impedance are presented here to evaluate the required dynamic range of the receiver and to show a typical variation of noise power as a function of source impedance.

As we have explained in Chapter 5, the extraction of noise parameters is achieved by the measurement of relative cold noise power associated with specific input impedances. We have also explained how internal settings of the noise measurement system must be selected to preserve the linearity of the receiver. In addition, the specific DUT being measured may have an important impact on the specification of the receiver with regards to the linearity requirement. For example, changes in impedance presented to a DUT can cause variation in the DUT's gain as high as 10 dB. The change in gain causes a change in available noise power at the output of the DUT since the DUT amplifies the available noise at its input. Although we cannot predict the actual change in available noise power without knowing the DUT noise parameters, there is a potential for the available output noise power to vary by the same order of magnitude as the gain of the DUT. Thus, the receiver must preserve linear amplification over a sufficient dynamic range. To better evaluate what is our specific requirement, we have plotted level curves of the measured noise power at 30 GHz in Figure 6.2. In this figure, the diamonds represent the source impedances at which measurements were made. The measured cold noise powers are presented by logarithmic level curves. The value of the noise power measured at each impedance results from the DUT gain, the DUT noise figure, the receiver gain and the receiver noise figure. Hence, this data is rarely presented since the noise parameters extracted from them provide information that is more meaningful. Nevertheless, this data is very important since we may be able to spot regions of instability and other unexpected phenomena from it. In fact, instability caused by the outer ring of source

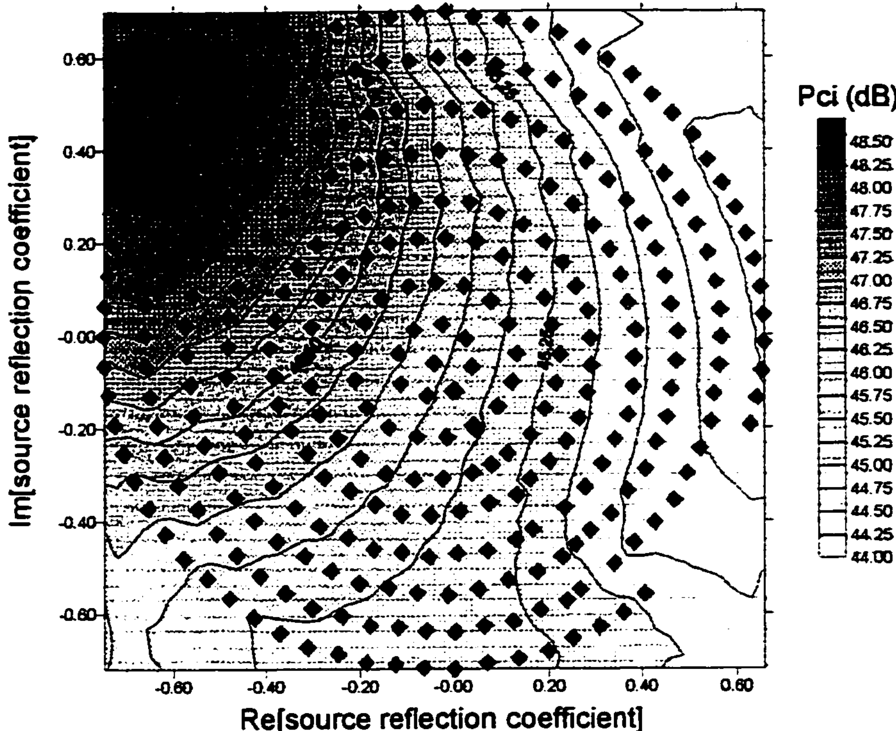

Figure 6.2 Cold noise power for 314 impedance points at 30 GHz with DUT X biased at Vds=2 V, Ids=10mA

impedance reduced the number of source impedance point plotted in figure Figure 6.2 from 404 to 314 source impedances. Note that the impedances causing instability, given by $|\Gamma_s| > 0.7$ and $0.65\angle{-45} < \Gamma_s < 0.65\angle{-45}$, are not shown in Figure 6.2. We can observe a rapid increase of the noise power on the top left corner of Figure 6.2. This region corresponds to the region of maximum available gain for this DUT.

6.2 PHEMT Noise Parameters as a Function of Bias

The minimum noise figure of PHEMTs (or FETs in general) gradually increases with increasing drain current [30] [76]. The aim here is to confirm the ability of our test setup to determine this dependence. We measured this dependence at 26 GHz to provide data with our system, which will be compaired to the results obtained on an independent system in a subsequent section. The noise parameters (NPAR) are calculated in three ways: once with the TWIN extraction algorithm (i.e. Lane's algorithm), once with our implematation of O'Callaghan's

algorithm in MMICAD, and once with a variation of the input block calibration technique. This is done to provide an indication of the variation to expect on the extracted noise parameters for these casses.

6.2.1 Method

The methodology followed is:

- calibrate the measurement setup at 26 GHz and verify the equipment operation with a thru line,
- define a constellation of nine source impedances as presented in Table 4. This constellation was refered to as the "Cross" in Figure 3.3.

$\lvert\Gamma_{si}\rvert$	0.04	0.36	0.38	0.36	0.41	0.66	0.66	0.65	0.67
$\angle\Gamma_{si}$	142.9	89.0	-179.4	-2.9	-90.6	92.4	177.9	0.0	-88.8

Table 4 Constellation of Source impedance

- probe on the DUT and set desired biasing conditions,
- measure the cold noise power associated with each impedance of the constellation,
- extract the noise parameters using TWIN (Lane's extrapolation algorithm),
- using the same intermediate parameters, extract the noise parameters using O'Callaghan's technique (our MMICAD implementation),
- repeat the previous step using the Hewlett Packard standard table of coefficients to determine the S-parameters of the input block. The only difference between the results of Table 6 and Table 7 is in the characterization of the 3 coaxial terminations that were used to determined the input block S-parameters. The results presented in Table 5 and Table 6 made use of measured termination from a calibration (SOLT) with the 2.4 mm calibration kit to perform the 3 termination calibration procedure. Whereas in Table 7 we make use of Hewlett Packard's standard table of coefficients for the 3 coaxial terminations.

- compare the results obtained which are presented in Table 5 for TWIN's extraction, in Table 6 for our MMICAD extraction, and in Table 7 for the variation on the input block 3 termination calibration technique.

6.2.2 Results for a PHEMT Device at 26 GHz

The noise parameters for DUT X and Y at 26 GHz are presented in the 3 following tables.

DUT	Fmin(dB)	Rn(ohms)	|Γopt|	∠Γopt
X5	0.85	22	0.674	75.6
X20	1.39	18.3	0.508	84.4
Y5	1.46	30	0.544	68.8
Y10	1.79	25.4	0.492	76.3
Y15	2.16	25.9	0.468	84.5
Y20	2.57	28.0	0.472	92.0

Table 5: TWIN calculated NPAR at 26 GHz

DUT	Fmin(dB)	Rn(ohms)	|Γopt|	∠Γopt
X5	0.81	21.9	0.676	75.6
X10	0.93	18.1	0.585	76.1
X20	1.35	18.2	0.509	84.4
Y5	1.42	29.8	0.546	68.7
Y10	1.75	25.2	0.494	76.3
Y15	2.12	25.8	0.470	84.5
Y20	2.54	27.8	0.473	92.0

Table 6 MMICAD calculated NPAR at 26 GHz using measured terminations for the 3-termination calibration procedure of the input block.

DUT	Fmin(dB)	Rn(ohms)	|Γopt|	∠Γopt
X5	0.87	22.2	0.679	75.3
X10	0.99	18.4	0.587	75.9
X20	1.42	18.5	0.510	84.2
Y5	1.48	30.3	0.547	68.5
Y10	1.81	25.6	0.495	76.1
Y15	2.19	26.2	0.470	84.3
Y20	2.61	28.3	0.473	91.8

Table 7 MMICAD calculated NPAR at 26 GHz using the Hewlett Packard table of standard coefficients for the 3-termination calibration procedure of the input block.

6.2.3 Discussion

The results behave as expected. Using the result of F_{mindB} for DUT Y presented in Table 7, we plot F_{mindB} as a function of Ids in Figure 6.3. The curve obtained is as expected from the

general model of FET and PHEMT [30] [76]. A similar curve could also be plotted for DUT X. The dependence of F_{mindB} is very well predicted from our measurement setup.

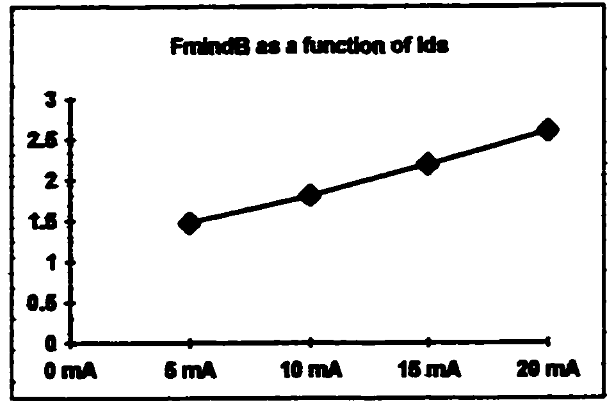

Figure 6.3 Minimum noise figure of DUT Y as a function of drain current

By looking closely at the value of F_{mindB} in Table 5 and Table 6 we observe a systematic difference on F_{mindB} of ~0.04 dB for all bias conditions. We recall that the same data is used in both cases to compute the noise parameters. We know as well that O'Callaghan and Lane's algorithms are optimizing the same error function. The difference on F_{mindB} is therefore attributed to the numerical precision used on measured parameters, which are required by the TWIN and the MMICAD implementation. We should emphasize that noise parameter extraction algorithms are optimization algorithms minimizing an error function. As such, knowledge about the sources of measurement error for a specific measurement system or methodology can be beneficial to properly select the best extraction algorithm. Unfortunately, such a study is too complex to be included in this thesis.

Although the methods used to extract the noise parameters presented in Table 6 and Table 7 are identical, we included both sets of data to illustrate the importance of characterizing the standards used for the 3 termination calibration procedure. As it can be seen, a difference of ~0.07 dB on the minimum noise figure can be observed. Hence, the characterization of the three coaxial terminations made using the Hewlett Packard standard table of coefficients or the measured reflection using a SOLT calibration have a small but significant impact.

We now address the difference in the noise parameters between two PHEMT devices located on the same wafer. It is of interest to determine if the difference is due to the actual fabrication process, which modifies the noise parameters or if it may be caused by the measurement setup. By looking at the DC biasing of DUT X and DUT Y, we observe a difference of 4 mA for the saturated drain current. More precisely, when Vds=2 V and Vgs=0.0 V then DUT X Idss=24.7 mA, and DUT Y Idss=28.7mA. Although FET models often make use of percentage of Idss to compare the performance from device to device, we made use of a fixed values of Ids for our measurement. This approach is usually taken for circuit design as it provides insight on the dispersion of the noise parameters from one device to the next for a specific circuit implementation. Nevertheless, variation of Idss indicates that device fabrication is not uniform across the wafer used. This is also confirmed by looking at the measurement of the S-parameters given in Figure 6.1. Thus, variation of noise parameters from device to device is expected. We feel that most of the variation from device to device at the same frequency comes from process variations since we have experienced a good repeatability with regard to S-parameter measurements and noise power measurements.

6.2.4 Conclusion

The noise parameters as a function of biasing were successfully measured at 26 GHz and were shown to behave as expected from noise models. It was also shown that two different extraction algorithm can yield different results from the same measured data due to the difference in their optimizing error function. Finally, selection of the characterizing technique for the three termination used during the 3-termination calibration procedure was shown to have a small but significant impact on the extraction of the noise parameters.

6.3 Noise Parameters as a Function of Frequency

A demonstration of the capability of our measurement system to extract noise parameters from 26 to 40 GHz is presented here. System calibration using a coaxial noise source and the ORNS are made and computed noise parameters for each case are presented.

6.3.1 Method

Due to the time required to calibrate and measure the noise parameters at 15 different frequency points, we measured only one device at one bias point over the complete frequency band. We selected DUT X10 for that purpose. All the data required at one frequency are measured before proceeding to the next frequency. The steps taken at each frequency are performed in the following order:

- perform a system calibration as described in Section 5.3 to 5.3.7 inclusively,
- probe on the TRL thru line and characterize the receiver according to Section 5.3.8. First perform a hot and cold noise power measurement with the coaxial noise source, then set the noise in its cold state and perform noise power measurements for a constellation of nine source impedances.
- Characterize the receiver again with the ORNS (i.e. Probe on the ORNS and perform a hot and cold noise power measurement),
- probe on DUT X and bias it at Vds-2.0 V, Ids=10.0mA, Vgs=-0.241 V,
- measure the cold noise power of the DUT/receiver chain for all source impedances previously calibrated. We generally have 101 impedances calibrated at each frequency which are uniformly spread over the Smith chart,
- eliminate all impedances where oscillation of the DUT was detected,
- select a set of nine impedances from which the noise parameters are extracted using O'Callaghan's algorithm. Note that the constellations used is slightly different at each

frequence but it always forms a large cross over the Smith chart like the one presented in Table 4.

- Compute the noise parameters for the coaxial noise source. See results in Figure 6.4.
- Use the computed noise parameters and calculate the difference between the noise figure calculated and the noise figure measured for each impedance used in the extraction of the noise parameters. See Figure 6.5.

6.3.2 Results from 26 to 40 GHz

The results presented here are the noise parameters with the coaxial noise source (Figure 6.4), the noise parameters with the ORNS (Figure 6.6), and the computed difference between noise figure measured at each impedance and calculated from the extracted noise parameters (Figure 6.5). We recall that when using the cold technique, the hot noise power measurement is required only once to compute the kBG_0 term. Thus, the only difference between the coaxial and ORNS results resides in the measured value of the kBG_0 term.

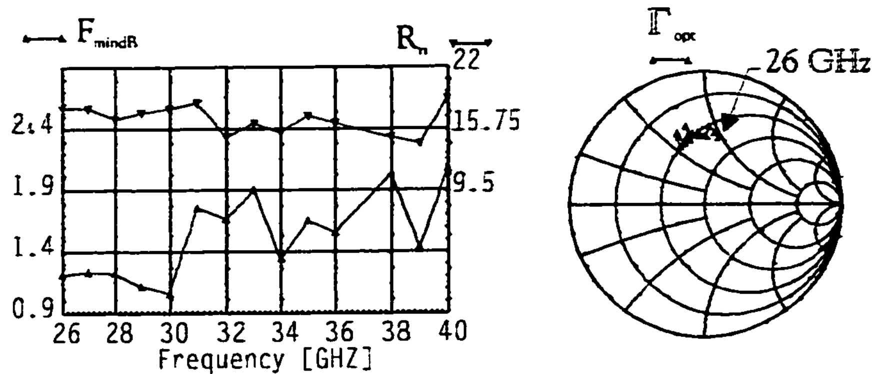

Figure 6.4: NPAR with Coaxial noise source

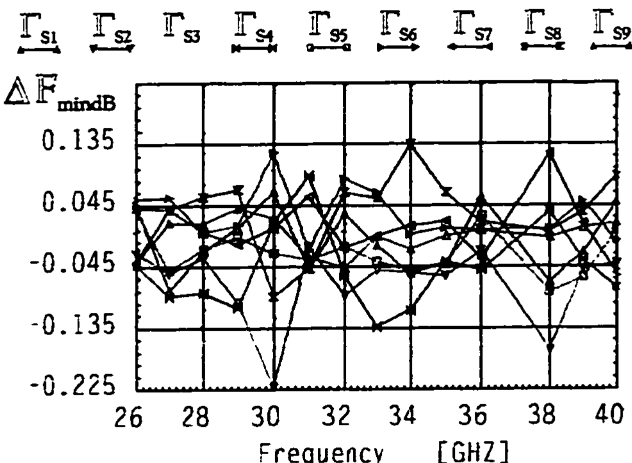

Figure 6.5: Difference between measured and calculated noise figure for each constellation of 9 source impedances (Γ_{Si}). A coaxial noise source was used here.

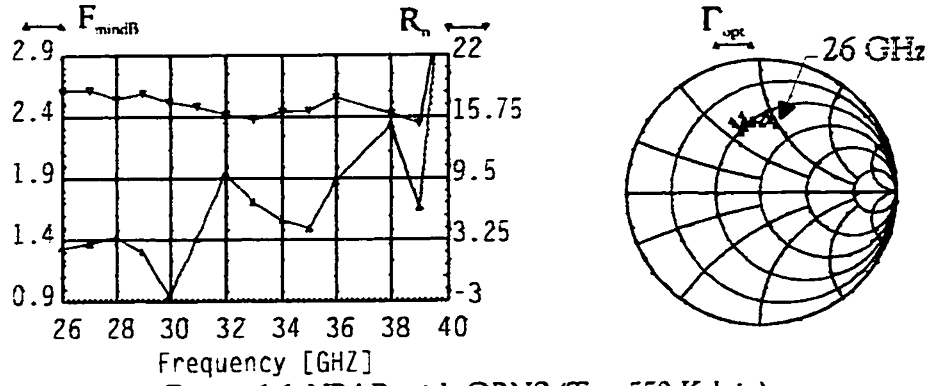

Figure 6.6: NPAR with ORNS (T_h=550 Kelvin)

6.3.3 Discussion

From the noise parameters shown in Figure 6.4 and Figure 6.6, we observe the following trends of the noise parameters as a function of frequency:

- F_{mindB} increases with frequency,
- R_n decreases with frequency,
- Γ_{opt} shows a counter clockwise rotation as a function of frequency.

The trends of the noise parameters we measured are in agreement with those presented in the literature over the years for HEMT and PHEMT devices.

Comparison between results shown in Figure 6.4 and Figure 6.6 demonstrate that both noise sources yield similar results. The potential of the ORNS is thus again demonstrated. By the same token, the 3-termination calibration procedure used for the results of Figure 6.4 is also verified.

By plotting the difference between the measured and the computed noise figure we gain confidence in the extraction algorithm used. We first observe from Figure 6.5 that the difference between the nine points at each frequency is centered on zero. Also, the difference rarely exceeds 0.14dB (3 %). Although such a difference is a sign of reasonable accuracy on the measured noise parameters, it cannot be used to state the accuracy of our measurement system.

You may have noticed that the value of F_{mindB} is 0.2 dB greater here than for the results shown in Table 7. The difference between the extraction of the two sets of parameters resides in the selection of the constellation. The selection of different constellations may therefore significantly influence the results obtained.

We limit our discussion here to these few points. A comparison with an independent laboratory and our uncertainty analysis will bring us more arguments to further explain the data presented.

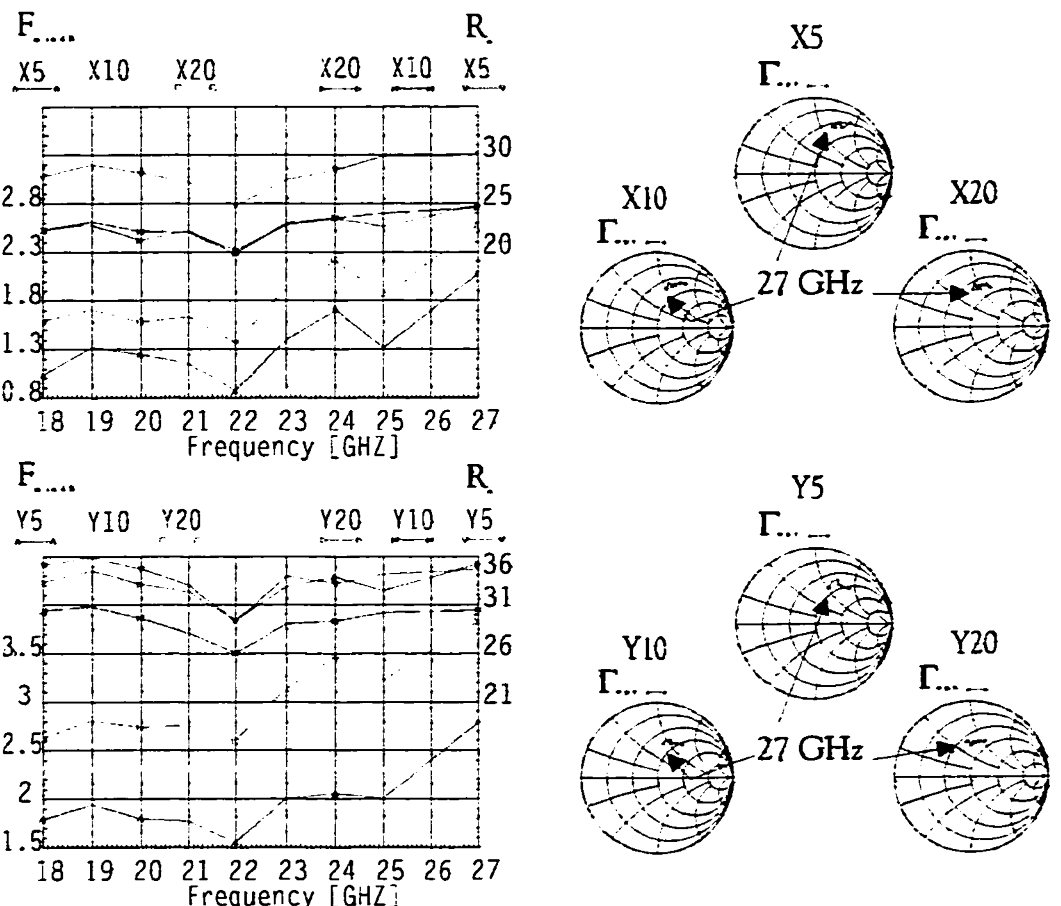

Figure 6.7 DUT X and DUT Y Noise Parameter from 18 to 27 GHz.

6.4 Confirmation of Noise Parameters at 26 GHz

After measuring the two devices, we sent them with the TRL calibration standards to Dr Ali Boudiaf at l'Université de Marne-la-Vallée in France. The devices were measured in a setup that he developed with CNET for measurements from 2 to 18 GHz and from 18 to 27 GHz. Results obtained from 18 to 27 GHz are presented in Figure 6.7 to confirm the validity of our measurements. We know that the cold power technique was used but unfortunately, the details of the extraction algorithm used were not made available to us. Take note that the results provided at 26 GHz were discarded as they were identified to be highly inaccurate. The cause of innacuracy was attributed to a bad selection of source impedance by Dr. Boudiaf. Hence, the results given at 26 GHz in Figure 6.8 are the average between 25 and 27 GHz.

These results (DUT BX, BY) are compared with our measurements (DUT X, Y) for Ids=5, 10, and 20 mA in Figure 6.8. At 26 GHz, the relative error between the two sets of S-parameters $((S_{Xij}-S_{BXij})/S_{Xij})$ was 9% for DUT X S_{11}, 6% for DUT X S_{21}, 2% for DUT Y S_{11}, and 3 % for DUT Y S_{21}.

A few comments are now made on the results just presented. First, we observe that the optimum reflection coefficient (Γ_{opt} of BX and BY) extracted by the independent laboratory matches well ours (Γ_{opt} of X and Y). This is not the case for the minimum noise figure (F_{mindB}), which is approximately 0.9 dB greater than ours, and for the noise resistance which is approximately 5Ω greater in most cases.

It is interesting to note from Figure 6.7 that, as in our case, the repeatability at a specific frequency is good but variation as a function of frequency still exists. The good repeatability of the two systems is also displayed by the error, which is similar for different devices and different bias conditions as shown in Figure 6.8.

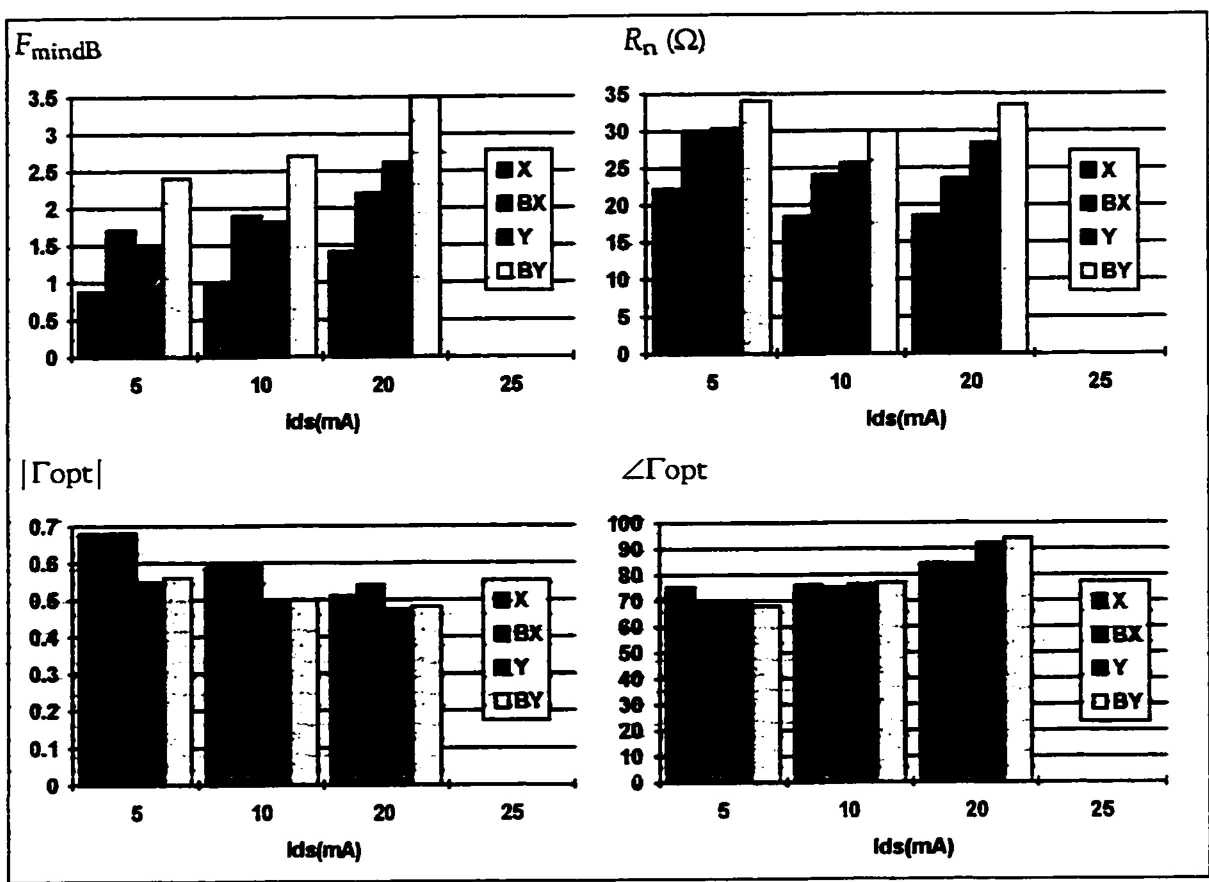

Figure 6.8 Comparaison of noise parameter between the independent system (BX, BY), our measurement (X, Y) at 26 GHz, and our measurement using the DUT S-parameter measured on the independent system (SX, SY)

The difficult question to answer is which of the two systems gives the most accurate answer for F_{mindB} and R_n. To address this question, we have to first determine the uncertainty on our measurement. The next chapter is therefore devoted to uncertainty analysis and to presenting possible explanation for the differences observed.

6.5 Conclusion

This chapter was devoted to present measurements of intermediate parameters (bias, S-parameters, noise power), DUT noise parameters as a function of bias, DUT noise parameters as a function of frequency (from 26 to 40 GHz), and an independent measurement of DUT X and Y from 18 to 27 GHz. Our measurement system showed it to be very repeatable at a specific frequency. Thus, the ability of the system to measure bias dependent noise parameters

was clearly demonstrated. The measurement as a function of frequency suffers from variations similar to those of other measurement systems. The verification of the noise parameters with the independent laboratory measurement matched well our extraction of Γ_{opt} well but presents a consistent difference of 0.9 dB on F_{mindB} and of 5 Ω on R_n. Finally, the use of an ORNS was again demonstrated to yield similar results to those of a coaxial noise source.

7. Uncertainty Analysis

The main goal here is to define the uncertainty of our measurements and, more importantly, to determine the areas where improvements would results in a significant enhancement of the accuracy. We proceed in 4 steps. First, we discuss the expected accuracy of the measured parameters by looking at the test equipment specifications and the measurement methodology used. We then look at uncertainties on the calculated parameters. Thirdly, we perform a yield analysis for the measurements made at 30 GHz and thus define the accuracy of the noise parameters at this frequency for the specific device used. Finally, we look at the sensitivity of the extracted noise parameters for a set of selected parameters.

7.1 The Uncertainty Analysis Technique

The complexities of measuring noise parameters at microwave frequencies makes uncertainty analysis very challenging. A recommended approach to evaluate uncertainties on noise factor is the measurement simulation method suggested in [38]. This method uses a computer to simulate probable measurement conditions. These conditions are then used to calculate measurement results such as noise factor and noise parameters. The more commonly used uncertainty analysis techniques based on partial derivatives are inappropriate here due to the oftenundefined dependence between the measured parameters. The presence of the optimization algorithm for the extraction of noise parameters also constrains us to use the simulation method.

The measurement simulation method is similar to the yield analysis technique commonly used in computer aided design software packages like MMICAD. Yield analysis is performed by first generating probable values of parameters, which satisfy a specified tolerance, and

which obey a probability distribution function such as Uniform or Gaussian. Secondly, we compute the results associated with the set of parameters generated. Thirdly, we repeat step one and two in order to create a large sample of results from randomly generated conditions. The yield of the experiment is then obtained as the percentage of the computed results meeting a specified tolerance. In our case, the measurement uncertainty is defined as the tolerance on the results required to achieve a 95% yield. The 95% confidence level is used by the Western European Calibration Cooperation (WECC) to define uncertainty in the case of Normal (Gaussian) distributions of parameters [77].

7.2 Parameters Measured and their Uncertainties

All parameters measured in our procedure are either temperature (T), relative noise power (P_n), or network parameters (Γ, S_{11}, S_{21}, S_{12}, S_{22}). We show in Table 8 that the basic parameters measured to compute the input block S-parameters (S_{inij}), the gain-bandwidth constant (kG_aB), the receiver noise parameters ($NPAR_{RCVR}$), and the DUT noise parameters ($NPAR_{DUT}$). Every basic parameters is looked at in the following sub-sections to define its worst case uncertainty and associated probability distribution function.

List of Parameters	S_{inij}	kG_aB	$NPAR_{RCVR}$	$NPAR_{DUT}$
T_C (room temperature)		X	X	X
Γ_{NS} (coaxial noise source cold)		X	X	X
Γ_{kterm} (coaxial terminations on-wafer)	X	X	X	X
Γ_{Si} (source impedance on-wafer)			X	X
Γ_L (receiver impedance on-wafer)		X	X	X
$SPAR_{DUT}$ (on-wafer)				X
P_C (cold noise power)		X	X	X
P_h (hot noise power)		X	X	X
P_{Ci} (associated noise power)			X	X
$P_{Ci\,DUT}$ (DUT associated noise power)				X

Table 8: Calculated parameters from basic measurement.

7.2.1 Reflection Coefficients and S-Parameters Uncertainties

To establish the uncertainty on the measurement of reflection coefficient and S-parameters is a very challenging task. The procedure proposed by the vendor consists in determining the

following parameters: system residuals, dynamic accuracy, noise, and repeatability [61]. This approach is valid when using coaxial standards but is insufficient for on-wafer probing. We recall that there exists a number of different on-wafer calibration techniques. Unfortunately, there is no existing technique that can be verified for their absolute accuracy. The absence of verification standards is due mainly to the difficulty in accurately defining the reference impedance of planar structures.

We avoid the problem by making use of typical VNA system measurement accuracy specifications [61] as a guide to define our worst case uncertainty. For reflection coefficients, we define an area of uncertainty as a fixed angle variation of $\Delta\angle\Gamma=\pm2°$ and a magnitude variation given by $\Delta|\Gamma|=\pm5\%$ of $|\Gamma|$. The area defined by this uncertainty has the shape of a truncated moon over the Smith chart. The probability distribution function of the uncertainty area also needs to be defined. As recommended in [77], we assume a rectangular distribution of values centered on the measured value. Thus, every reflection coefficient of our yield analysis is performed using the MMICAD uniform distribution defined by a centered value with minimum and maximum limits.

The typical system measurement accuracy specification for the transmission coefficient (i.e. S_{21} and S_{12}) are different from the reflection coefficient (i.e. Γ, S_{11} and S_{22}) and thus they have to be treated separately for uncertainty analysis purposes. The uncertainty on S_{21} and S_{12} is taken has $\Delta|S|=\pm3\%$ and $\Delta\angle S=\pm1°$. The uniform probability distribution function is selected here as well.

We recognize that the uncertainty we have attributed to reflection and transmission coefficients are not completely justified but we believe them to be the worst case for our measurement. We apply these definitions to our measured parameter Γ_{NS}, Γ_{3term}, Γ_{Si}, Γ_L, and $SPAR_{DUT}$ for the yield analysis performed in Section 7.4.

7.2.2 Noise Power Measurement Uncertainties

The accuracy on noise power measurements using our setup is defined in this section. The accuracy of these measurements is determined by the receiver linearity, receiver drift, averaging factor used, flatness of the noise signal over the measurement bandwidth, frequency discrepancies with the VNA and the elimination of unwanted signals which may fall in the measurement bandwidth.

Definition of the uncertainty caused by receiver non-linearity could not be evaluated due to the lack of information on the test equipment used. After having verified that we didn't exceed the maximum input power specified by the test equipment manufacturer, we assume that the non-linearities of our receiver are non-existent. Non-linearities are therefore not quantitatively considered.

We determined that receiver drift was not causing more then 0.01 dB change on the power reading over a typical measurement period of 30 minutes.

The averaging factor of the noise figure meter was selected to be 64 after experimentally finding that a repeatability of ±0.005 dB was achieved with this setting. The specification manual refers to a 0.02 dB accuracy on the measurement of the Y-Factor ($Y=N_2/N_1$) when using an averaging factor of 64 [78]. Hence, repeatability better then 0.02 dB is expected for a single noise power measurement.

Error caused by noise power flatness over the measurement bandwidth and the frequency discrepancy with the VNA were studied in [72]. It was observed that sudden and repetitive variation in the noise power reading by as much as 10 dB exists when the noise receiver and the noise source have highly mismatched, and frequency dependent, reflection coefficients. It is clearly shown in this paper that both the measurement bandwidth and frequency discrepancies can cause significant errors in some specific cases. Unfortunately, the evaluation of the errors with no simplification is extremely complicated and hence, closed-form solutions

can only be obtained after making a number of simplifications. The magnitude of the error was computed for only the specific case of two highly mismatched reflection coefficients. A calculated error of 5% caused by a measurement bandwidth of 4 MHz and a calculated error of 25 % caused by a 1 MHz frequency offset were obtained for one specific case where the source impedance and the receiver impedance are highly mismatched. For our measurements, no variation of power with frequency was observed in the measurement band. As well, we aligned the VNA frequency with the noise figure measurement system such that they are the same within ±0.5 MHz. We therefore assume that both errors can be neglected for the measurement of the PHEMT from 26 to 40 GHz.

We eliminate the requirement to define an uncertainty caused by picking up unwanted signals. We are confident that the unwanted signals, which can come from electromagnetic interferences, oscillation of the DUT and other external sources, can be detected by continuously monitoring the measured noise signal on a spectrum analyzer.

After having considered all the above possible sources of error, we define our uncertainty on noise power measurement as ΔP_n = 0.5 % (0.02dB). We consider this uncertainty to have a uniform probability distribution function. This uncertainty definition is used for the measured parameters P_c, P_h, P_{ci}, and $P_{ci\ DUT}$ used in the yield analysis performed in Section 7.4.

7.2.3 Temperature Measurements

The ambient room temperature is continuously monitored with a thermometer. This is required for two reasons. First we need to know the ambient temperature T_C for our calculation and second we want to keep the room temperature constant in order to eliminate electronic drift caused by temperature changes. We define our accuracy on the ambient temperature as $\Delta T_C = \pm 1K$ with a uniform distribution.

7.3 Calculated Parameter Uncertainties for Noise Parameter Extraction

Having looked at the uncertainties of the basic parameter uncertainties, we now wish to look at the uncertainty of a number of calculated parameters. This work is performed to better understand how the uncertainty of the basic parameters are cumulated to obtain the uncertainty of the DUT noise parameters.

7.3.1 Uncertainty on Input Block S-Parameters

The S-parameter characterization of the input block network, which is located between the coaxial noise source and the on-wafer reference plane, is made during the calibration of our test setup. Uncertainties introduced by the 3-termination procedure result in higher uncertainty on the excess noise ratio (ENR) calculated at the on-wafer reference plane and on the gain-bandwidth constant of the receiver. We thus need to evaluate the uncertainty on the input block S-parameters.

The parameters measured are the on-wafer reflection coefficients of the input block when it is connected to each of the 3-terminations (Γ_{3term}). We also make use of the reflection coefficient of the 3 terminations at the coaxial reference plane as explained in Appendix Appendix D. The uncertainty on the input block S-parameters (S_{in11}, S_{in21}, S_{in12}, S_{in22}) can be evaluated by the simulation approach. The uncertainties obtained with the yield analysis technique are presented in Table 9. The previously defined uncertainties on reflection coefficient measurements and our measurement results at 30 GHz were used.

	S_{in11}	S_{in21}	S_{in12}	S_{in22}
Value	0.193 ∠-142°	0.735 ∠20°	0.735 ∠20°	0.0189 ∠-91°
Uncertainty	±0.05 ∠±20°	±0.03 ∠±2°	±0.03 ∠±2°	±0.001 ∠±2°
Yield	98.8% ∠97.8%	100% ∠100%	100% ∠100%	100% ∠100%

Table 9 Uncertainty on input block S-parameters at 30 GHz

The resulting uncertainties are used in a later sections to derive the uncertainty on the gain-bandwidth constant (kG_aB).

7.3.2 Uncertainties on the Coaxial Available Noise Temperature (T_h)

The uncertainties on T_h at the coaxial reference plane are obtained from the accuracy specification of the noise source used. In our case, the accuracy is specified on the ENR as 0.1 dB (2%). Thus, for a known ENR, the uncertainty on T_h can be computed from (3.1).

We have an additional uncertainty on T_h which is caused by TWIN's definition of ENR. We know that Hewlett Packard uses Eq. (3.1) as their definition of ENR. The TWIN software defines the ENR by assuming that $\Gamma_{NSh}=0$. All results presented in this thesis made use of TWIN's definition of ENR to allow direct comparison of TWIN results with our implementation. This discrepancy in the ENR definition can be regarded as an additional uncertainty on T_h.

Computation of this additional uncertainty on T_h at 30 GHz is made in this paragraph to evaluate the significance of this error. The HP346C noise source specifies an ENR of 11.87 dB with a measured reflection coefficient of $\Gamma_{NSh}=0.100\angle 175$. We calculate for TWIN T_{hTWIN}=4750K and with Eq. (3.1) T_{hHP}=4799K. Hence we may suffer from a systematic error of 48K or 1% on T_h. By looking at Figure 3.1, we view that increasing T_h causes kGaB to decrease and N_a to increase. We conclude from this that we consistently underestimate our noise figure measurement of the receiver. The impact on the resulting DUT noise parameters is looked at later with the sensitivity analysis.

7.3.3 Uncertainties Caused by the Noise Source Change of Impedance.

To make use of the cold power technique presented by Adamian in [58] one must be able to generate two distinct noise temperatures at the same source reflection coefficient. Hence the assumption was made that the noise source hot state presented the same impedance as the

noise source cold state. We present in this section a means of verifying the validity of this assumption. To do so, we calculate the error introduced on T_h by this assumption at 30 GHz. Note that the verification of the assumption with the technique presented can only be made after having measured the receiver noise parameters.

We know that an impedance change at the input of the receiver causes a change in its available gain (G_a) and a change in its added noise power (N_a). This change causes a systematic error in the hot noise power reading, which we refer to as ΔP_h. By looking at figure Figure 3.1, we relate ΔP_h to a variation in the hot noise temperature ΔT_h by $\Delta T_h = \Delta P_h / kG_aB$.

Keeping these observations in mind, we evaluate the magnitude of ΔP_h from the noise parameter and the available gain of the receiver used. The noise parameters of our setup were measured at 30 GHz and are given as: F_{mindb}=6.144 dB, R_n=35.862 Ω, Γ_{opt}=0.146∠-173.9. The receiver available gain is obtained from the kBG_0 term presented in appendix Appendix B, and measured here as kBG_0 = 13.681. At 30 GHz, we measured the noise source change of impedance from Γ_{NSOWC} = 0.06180 ∠ -75.5306 to Γ_{NSOWh} = 0.06460 ∠ -121.654 . From the measured noise parameters, we can compute the noise figure of the receiver at both impedances with Eq. (2.20). We obtain at Γ_{NSOWC}, F_{dBC} = 6.257923 dB, and at Γ_{NSOWh}, F_{dBh}=6.20159. From Eq. (2.11), we can re-write the noise figure in terms of added noise temperature of the receiver as T_{aC} = 935.1529K and T_{ah}=919.366K. It can be shown that the output noise power of a noise source and receiver chain is given by [2]:

$$P_n = T_n kG_a B + T_a kG_a B \qquad (7.1)$$

where T_n is the noise temperature of the noise source and T_a is the added noise temperature of the receiver. By applying Eq. (7.1) to both states of the noise source and taking the difference, we compute the error on the measured noise power attributed to the change of noise source impedance as:

$$\Delta P_h = T_{ah} k G_{ah} B - T_{aC} k G_{aC} B \qquad (7.2)$$

where T_{ah} and G_{ah} refer to the receiver added noise temperature and available gain when being presented with the impedance of the hot noise source, and T_{aC} and G_{aC} refer to the receiver added noise temperature and available gain when being presented with the impedance of the cold noise source.

The assumption is made at this point that the receiver is unilateral in order to make use of the kBG_0 term presented in appendix Appendix B. By replacing the available gain in Eq. (7.2) with the kBG_0 term we obtain:

$$\Delta P_h = T_{ah} kBG_0 \left(\frac{\left(1 - |\Gamma_{NSOWh}|^2\right)}{|1 - \Gamma_L \Gamma_{NSOWh}|^2} \right) - T_{aC} kBG_0 \left(\frac{\left(1 - |\Gamma_{NSOWC}|^2\right)}{|1 - \Gamma_L \Gamma_{NSOWC}|^2} \right). \qquad (7.3)$$

Recalling that $\Delta T_h = \Delta P_h / kG_a B$, where $kG_a B$ is specific to the noise source reflection coefficient in its cold state. We can write (7.3) as:

$$\Delta T_h = T_{ah} \cdot \frac{\left(\frac{\left(1 - |\Gamma_{NSOWh}|^2\right)}{|1 - \Gamma_L \Gamma_{NSOWh}|^2} \right)}{\left(\frac{\left(1 - |\Gamma_{NSOWC}|^2\right)}{|1 - \Gamma_L \Gamma_{NSOWC}|^2} \right)} - T_{aC}. \qquad (7.4)$$

Note that $\Gamma_L = 0.168\angle 141°$ at 30 GHz. After computation, we find that ΔT_h =-4.992K . This value of ΔT_h is specific to our setup at 30 GHz and should not be generalized. We can estimate a worst case error for our setup from the specified maximum change of impedance of the noise source to be $\Delta|\Gamma|=0.1$. We compute ΔT_h for a change of impedance going from $\Gamma=0$ to $\Gamma=0.1$. The noise parameters of our receiver at 30 GHz are used. The new error computed is $\Delta T_h = 10.61$ K. The assumption is made that the last value of ΔT_h found can be

said to be typical for both the on-wafer and the coaxial reference plane. It should be clear that this error is not accounted for in our setup. It is therefore added to the uncertainty on T_h in the subsequent uncertainty analysis. Correction for this error is impossible by following the procedure suggested by Davidson and al in [50]. We caution that one should be careful in correcting only for the change of available gain or only for the change in added noise power. We notice with our example that such a correction would introduce a larger systematic error then not applying the correction at all. Note as well that the error on impedance change is much more significant with the ORNS. At 30 GHz, a ΔT_h of 10 K represent an error of 0.2% with the coaxial noise source and and error of 1.7 % with the ORNS

7.3.4 Uncertainty on the Gain-Bandwidth Constant (kG_aB) and the (kBG_0) term

The computation of the gain-bandwidth constant is an intermediate step to calculate the noise factor associated with each input impedance. The kG_aB constant was introduced in Figure 3.1 as the slope of the line joining a cold and a hot power measurement. The available gain (G_a) portion of this constant is a function of the source impedance presented to the receiver. Hence, the impedance presented by the noise source needs to be specified. We have already seen that the noise source change of impedance between the cold and hot state introduces an ambiguity with regards to the source impedance at which our measurement is valid. This ambiguity was accounted for by increasing the uncertainty on T_h and by defining the source impedance to be the cold noise source reflection coefficient.

Generalization of the measured gain-bandwidth to account for different source impedances is required. This step is performed in appendix Appendix B by introducing the kBG_0 term and assuming that the receiver is unilateral (i.e. $S_{r12}=0$). The kBG_0 term is given by:

$$kBG_0 = \frac{P_h - P_c}{T_h - T_c}\left(\left|1 - \Gamma_L\Gamma_S\right|^2\right)\left(\frac{\left|1 - S_{in11}\Gamma_{NS}\right|^2}{\left(1 - \left|\Gamma_{NS}\right|^2\right)\left|S_{in21}\right|^2}\right) \quad (7.5)$$

The uncertainty on parameters found in Eq. (7.5) were estimated at 30 GHz and are given in Table 10. Note that although we define the uncertainty on T_h with an additional systematic error of +48K to reflect the comment made in Section 7.3.2, we don't take this factor into account here.

Tc	Th	Ph and Pc	Γ_L, Γ_S, Γ_{NS}	S_{in11}	S_{in21}
±1K	±120K+ 48K	0.02 dB	5% of |Γ| ∠±2°	±0.05 ∠±20°	±0.03 ∠±2°

Table 10 Uncertainty on parameters required to compute the kBG_0 term

We performed three separate yield analyses to evaluate which parameters had the most impact on the accuracy of kBG_0. We first varied the parameters T_c, T_h, P_c, and P_h and leave the other parameters to their nominal value. We obtained kBG_0=13.4696 ±0.4, yield=97.4 %, number of trials=1000. This represents a 3% uncertainty. We then incorporate the uncertainty in S_{in11} and S_{in21}. We obtained kBG_0=13.4696 ±1.3, yield=97.6 %, number of trials=1000. This represents a 10% uncertainty. Finally, we introduced the uncertainty on Γ_L, Γ_S, and Γ_{NS} with the others. The result obtain is kBG_0=13.4696 ±1.3, yield=97.2 %, number of trials=1000. This represents also a 10% uncertainty.

We conclude that the main source of uncertainty comes from the uncertainty on the input block S-parameters (S_{in11}, S_{in21}). The uncertainty on T_c, T_h, P_c, and P_h are also non-negligible but less significant. Finally, Γ_L, Γ_S, and Γ_{NS}, uncertainties seem to have little effect on the kBG_0 parameter.

7.3.5 Uncertainty on Receiver Noise Parameters

As we have seen, calculation of the receiver noise parameters is performed from the kBG_0 constant and at least four measurements of cold noise power associated with four source

reflection coefficients. The uncertainties on the four extracted receiver noise parameters ($_TF_{min}$, $_TR_n$, $_T\Gamma_{opt}$) are evaluated at 30 GHz in this section.

A constellation of nine source impedances was selected to perform the receiver noise parameter extraction with O'Callaghan's algorithm. The relative cold power measurements associated with each source impedance are presented in Table 11. The table also presents the calculated noise factor for each impedance which is obtained using:

$$F_i = \frac{P_{ci}}{kBG_0T_0}\frac{\left(|1-\Gamma_L\Gamma_{Si}|^2\right)}{\left(1-|\Gamma_{Si}|^2\right)} - \frac{T_C}{T_0} + 1 \qquad (7.1)$$

where $T_0=290$ K.

30GHz	$\lvert\Gamma_{Si}\rvert$	$\angle\Gamma_{Si}$	P_{ci}	F_i	F_{idB}
Γ_{S1}	0.033	128.2	42.205	4.24	6.27
Γ_{S2}	0.390	-96.5	42.504	4.87	6.88
Γ_{S3}	0.378	174.6	42.149	4.45	6.49
Γ_{S4}	0.293	-1.3	42.204	4.99	6.98
Γ_{S5}	0.398	93.5	41.906	5.09	7.06
Γ_{S6}	0.721	-94.7	42.696	8.38	9.23
Γ_{S7}	0.750	175.1	41.882	7.51	8.76
Γ_{S8}	0.697	90.9	41.578	8.28	9.18
Γ_{S9}	0.658	-1.3	42.122	8.67	9.38

Table 11 Relative Cold Noise Power associated with a constellation of nine source impedance for receiver calibration at 30 GHz

We make use of our implementation of O'Callaghan's algorithm and of the uncertainty previously defined on the parameters used to perform a yield analysis. Take note that uncertainty on Γ_{Si} due to the tuner repeatability and to the frequency difference between the network analyzer and the noise figure measurement system are assumed negligible compared to their uncertainty due to S-Parameter measurements.

	Nominal	Δ	Yield	trials
rFmin	4.180	±0.5	100%	1000
rRn (Ω)	36.43	±4	96.9%	1000
|rΓopt|	0.1456	±0.01	96.6%	1000
∠rGopt	-173.9	±4	97.0%	1000

Table 12 Uncertainty on receiver noise parameters at 30 GHz

The results of our analysis are presented in Table 12. In addition, we observed during the analysis that the 10% variation on kBG_0 accounts for 90% of the uncertainty on rF_{min} and rR_n but doesn't affect at all the value of Γ_{opt}.

The uncertainties obtained here are the starting point for the uncertainty analysis performed on the DUT X noise parameters presented in the next section.

7.4 Uncertainty Yield Analysis on the DUT Noise Parameters

The uncertainties on the measurement of DUT X is obtained in this section by performing a yield analysis. The analysis is performed with two different constellations: once with the cross and once with a smaller cross centered around the optimum reflection coefficient (Γ_{opt}). Note that the results obtained are specific to DUT X biased at 10 mA and measured at 30 GHz.

7.4.1 Results for DUT X at Ids = 10 mA

The results presented in Figure 7.1 were computed by making use of the previously defined uncertainties on measured parameters. The patterns shown in each graph were obtained by plotting all computed results of the 500 randomly selected set of parameters.

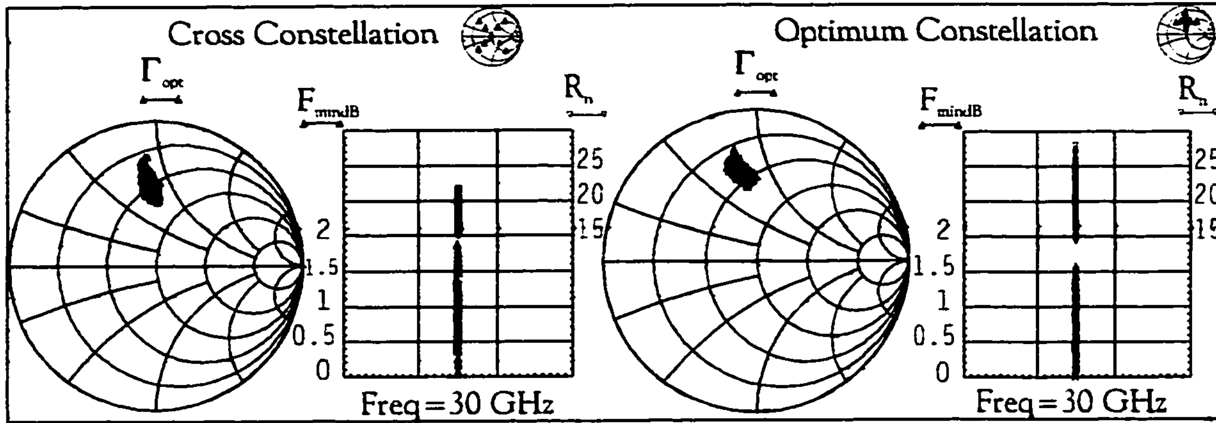

Figure 7.1 Uncertainty on DUT X Noise Parameters.

Our first observation is made on the minimum noise figure F_{mindB}. The minimum noise figure is spread over a range of ±1 dB. The nominal value for F_{mindB} is smaller for the Optimum constellation than for the Cross constellation. This results in a maximum value of F_{mindB}= 1.5 dB versus F_{mindB} = 1.9 dB for the respective constellations.

The noise resistance (R_n) shows a spread of ±4Ω with the Cross constellation and a spread of ±7Ω with the Optimum constellation.

The optimum reflection coefficient (Γ_{opt}) shows a spread of $\pm 0.09\angle\pm 9°$ for the Cross and a spread of $\pm 0.13\angle\pm 10°$ for the Optimum constellation. Hence, the Cross constellation provides a slightly better uncertainty on R_n and Γ_{opt} in this case.

The uncertainty derived by our analysis deserves a few comments at this point. We first emphasize the fact that the analysis was performed from a specific set of measured data points. As such, the results obtained can only be interpreted for a similar set of data. We can assume that this is the case for our measurements from 26 to 40 GHz of DUT X biased at 10 mA. Hence the variation observed in the frequency dependent measurements presented in Figure 6.4 can be attributed to the uncertainties on the basic parameters measured.

We can also use the uncertainty calculated to partially explain the difference between our measurements and Dr. Boudiaf 's measurements, which were summarized in Figure 6.8. We recall that a difference of 0.9 dB on F_{mindB} and of 5 Ω on R_n were observed at 26 GHz for all

bias conditions. Hence Dr. Boudiaf 's measurements are at the maximum limit specified by our uncertainty analysis. We recall that at 26 GHz, the relative error between our S-parameters and Dr.Boudiaf's $((S_{Xij}-S_{BXij})/S_{Xij})$ was 9% for DUT X S_{11}, 6% for DUT X S_{21}, 2% for DUT Y S_{11}, and 3 % for DUT Y S_{21}. To be consistent with our uncertainty analysis, we write in Table 13 the same information in terms of a variation on the magnitude and angle of the S-parameters $((\Delta|S_{D11}| = |S_{Xij}|-|S_{BXij}|)/|S_{Xij}|;\ \Delta\angle S_{D11}=\angle S_{Xij}-\angle S_{BXij})$.

ΔS_{DX511}	ΔS_{DX1011}	ΔS_{DX2011}	ΔS_{DY511}	ΔS_{DY1011}	ΔS_{DY2011}
|0.3%| ∠4.6°	|0.2%| ∠-5.0°	|-0.03%| ∠-5.0°	|-0.1%| ∠1.7°	|-0.1%| ∠1.4°	|-0.8%| ∠1.1°
ΔS_{DX521}	ΔS_{DX1021}	ΔS_{DX2021}	ΔS_{DY521}	ΔS_{DY1021}	ΔS_{DY2021}
|6.7%| ∠-0.3°	|7.3%| ∠-0.7°	|7.3%| ∠-0.6°	|0.9%| ∠1.4°	|1.4%| ∠1.2°	|1.9%| ∠1.2°

Table 13 Difference between my S-parameter and Dr Boudiaf's for DUT X and Y at 26 GHz.

We observe that the S-parameters of DUT Y fall within our range of uncertainty but not DUT X. The difference between the two noise parameter measurements can not be fully explained from this information. Having considered the uncertainty on our measurements without successfully explaining the difference in F_{mindB} and on R_n, two options are left to evaluate. The error on Dr. Boudiaf 's may be more significant than ours or there is still a source of error which has not been identified in our setup. The first one could not be further investigated due to the lack of information about the procedure that was used. The second one is addressed by bringing forward other potential reasons to explain this difference.

7.4.2 Theoretical Limit on Noise Parameters.

Pospieszalski introduced a theoretical inequality that must be satisfied by the noise parameters in [16]. It was shown that measurement systems for the extraction of noise parameters could easily violate this inequality. In fact, a widely referenced paper was even shown to violate this inequality which is given by [79]:

$$F_{min} - 1 \le 4N \quad \textit{where} \quad N = R_n G_{op} = \frac{R_n}{Z_0} \mathrm{Re}\left[\frac{1 - \Gamma_{opt}}{1 + \Gamma_{opt}}\right] \tag{7.2}$$

The computation of this inequality for our measurements was performed for all the results shown in Figure 6.4. The inequality of (7.2) was satisfied at all frequencies. We also computed the inequality while running the yield analysis on DUT X at 10 mA and again found that the inequality was always satisfied.

The inequality was also computed for the independent measurement results that were presented in Section 6.4. Again, the inequality was satisfied for every measurement.

7.4.3 Consideration of the Receiver Linearity

Throughout this thesis, the assumption was made that the receiver used was linear. We want to consider here the qualitative effect of a receiver being slightly nonlinear on the measured noise parameters. The analysis is made for both the Cold power technique and the hot/cold technique. We start our analysis from Figure 3.1 by adding to it a typical curve representing the non-linear behavior of a receiver as shown in Figure 7.2 by the *Actual* curve.

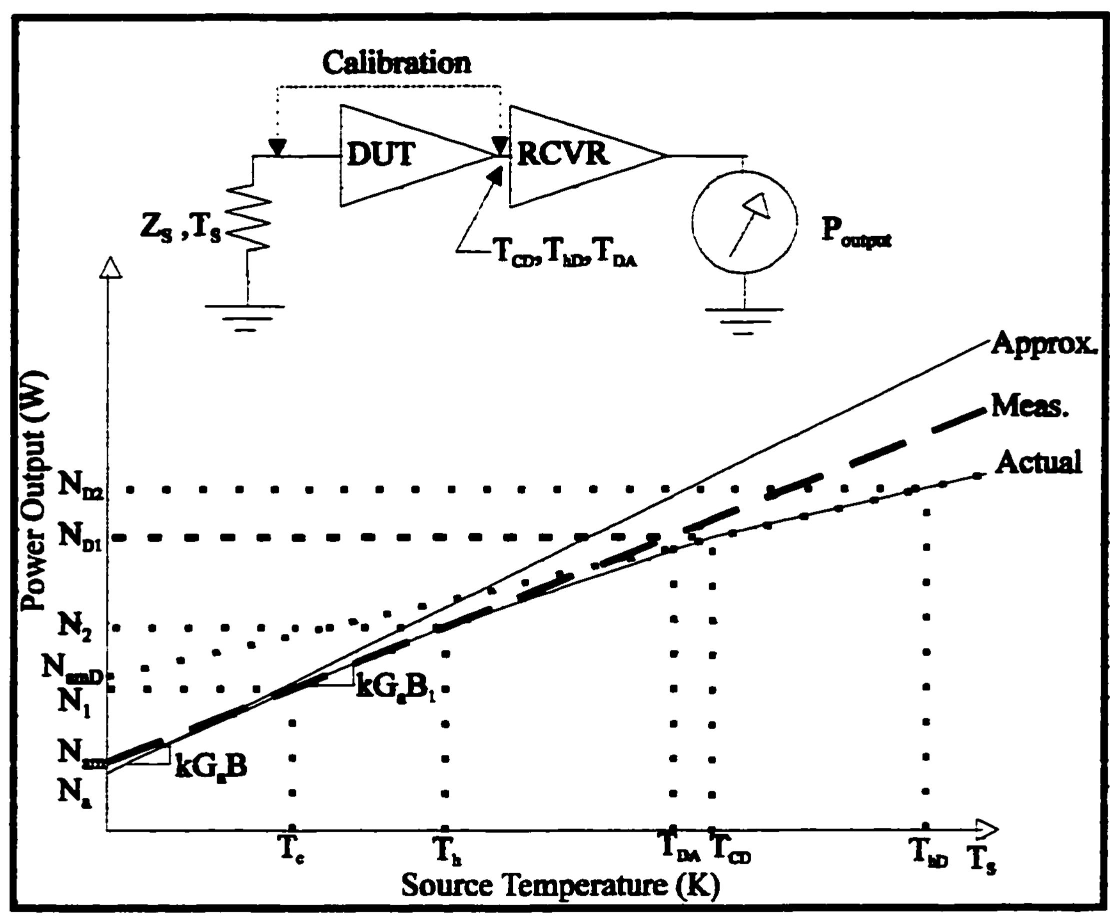

Figure 7.2 Noise Figure measurement considering a non-linear receiver.

We assume for the purpose of the following discussion that the DUT inserted between the noise source and the receiver contributes no added noise $N_{aDUT}=0$. Also, the reflection coefficient presented to the receiver (RCVR) by the noise source is assumed to be the same as the noise source and DUT combination.

We now explain the measurement procedure with the help of Figure 7.2. We first perform a calibration of the receiver by measuring N_1 and N_2 from the two known noise source temperatures T_c and T_h. The receiver being non-linear, we compute the receiver added noise N_{am} which is slightly greater than the actual added noise of the receiver N_a. Also, the gain bandwidth constant measured (kG_aB_1) is slightly smaller than the actual receiver gain-bandwidth constant (kG_aB).

We now connect the DUT between the noise source and the receiver and we make use of the hot/cold technique to measure the noise figure of the DUT. Knowing the gain of the DUT and having defined $N_{aDUT}=0$, we can compute the noise powers at the DUT's output and represent them by T_{CD} and T_{hD}. We can re-measure the receiver added noise power (N_{aDm}) from the measurement of the noise power N_{D1} and N_{D2} associated with T_{CD} and T_{hD}. By extrapolating the line joining (T_{cD},N_{D1}) to (T_{hD},N_{D2}) we observe that the newly measured added noise power (N_{amD}) of the receiver is greater then N_{am}. This measurement also represents the total added noise power of the DUT and receiver chain. Hence, making use of Friis' equation as we would normally do to compute the DUT added noise power (N_{aDUT}) would yield a value greater than zero due to a decreasing gain-bandwidth with increased input power. We can therefore conclude that using the hot/cold technique with a slightly non-linear receiver would give us a systematically greater DUT noise figure [57].

Let us now look at the same measurement using the cold power technique. After having performed the receiver calibration, we have computed the gain-bandwidth (kG_aB) and added noise (N_{am}) of the receiver from T_c, T_h, N_{a1}, and N_{a2}. The DUT is then inserted and the cold noise power N_{D1} of the DUT receiver chain is measured. To obtain the added noise power of the DUT, we compute the output noise temperature of the DUT (T_{DA}) from N_{D1} on the measured characteristic of the receiver. The result is obtained graphically in Figure 7.2 as the intersection of N_{D1} and the "*Meas.*" curve. We observe that T_{DA} is smaller then T_{DC}. Hence, the DUT noise figure computed is smaller then zero. We can conclude that with a non-linear receiver, the cold power technique results in systematically smaller DUT noise figure.

The degree of non-linearity determines how significant the error may be. We recall that an uncertainty of 0.02 dB (0.5%) on relative cold power was used for our uncertainty analysis by assuming that the receiver used was linear. Hence, for non-linearity to be negligible, the

difference between the receiver *Actual* response and its linear approximation must not exceed 0.02 dB. We previously explained that we could not evaluate this effect for our setup due to the lack of more precise information on the linear responsiveness of the amplifier used in our receiver chain. We therefore keep this hypothesis as a possible source of additional uncertainty, which may explain the difference observed with Dr. Boudiaf 's measurements.

Unfortunately, verification of this hypothesis and quantifying technique to precisely determine the receiver non-linearity is left for future work. We may just add that further studies on the hot/cold technique versus the cold power technique to measure DUT noise figure may potentially reveal a means of quantifying the receiver non-linearity since one technique overestimates and the other one underestimates the noise figure as a function of the degree of non-linearity.

7.5 Sensitivity of Selected Parameters on the DUT Noise Parameters

The sensitivity analysis helps understand the relative importance of individual parameters on the accuracy of extracted DUT noise parameters. We are particularly interested in T_h, P_{ci}, and the frequency (f) . The interest is due to the assumption made earlier about the definition of ENR, the linearity of the receiver, and the frequency discrepancies between the VNA and noise figure measurement system. We add to these parameters the DUT S_{D11} ,S_{D21} , and kBG_0 to emphasize the importance of these three parameters when making noise parameter measurements.

The sensitivity analysis is performed by computing the DUT noise parameters for the nominal case and then for the varied parameter. Our nominal case is taken as the measurements made for DUT X with Ids=10mA and f=30 GHz. Results are presented in Table 14 for the following cases:

- T_h is augmented by 48 K (T_h+48K) to evaluate the impact of the assumption $\Gamma_{NSh}=0$ made on the definition of ENR,
- the DUT cold power measurement (P_{ci}) is augmented by 0.2 dB for all source reflection coefficients (Pci+0.2dB for all Γsi) to simulate hypothetical receiver non-linearity. This simulation is hypothetical because in reality, the non-linearity would introduce different error as a function of source impedances,
- a discrepancy of 1 MHz between the VNA and the noise figure measurement system is simulated by augmenting the angle on all source impedance by 0.35° (All ∠Γsi+0.35° (or f+1MHz)). This simulation is made because we experimentally found that the angle of the tuner reflection coefficient varies by 0.35° per 1 MHz at 30 GHz. This simulation doesn't take all aspects the of frequency discrepancy into account [72],
- the DUT input reflection coefficient (S_{D11}) is varied by 3%∠2° (S_{D11}-(0.03|S_{D11}|∠2°)) to reflect the uncertainty on reflection coefficient measurements,
- the magnitude of the DUT transmission coefficient (S_{D21}) is varied by 3 % (|S_{D21}-|+0.03·|S_{D21}-|) to reflect the uncertainty of the VNA,
- the kBG_0 is varied by 10 % to reflect the uncertainty which was mainly caused by the 3 termination calibration.

	FmindB	Rn (Ω)	|Γopt|	∠Γopt
Nominal	1.06133	17.7956	0.54386	94.4716
Th+48K	1.10204	17.9768	0.54408	94.3388
Pci+0.2dB for all Γsi	1.36772	19.0549	0.54256	95.9277
All ∠Γsi+0.35° (or f+1MHz)	1.05373	17.8744	0.54521	94.3478
All ∠Γsi+2.1° (or f+6MHz)	1.01839	18.2866	0.55099	93.7116
{|S_{D11}|·(1.05);∠S_{D11}+2°}	0.75091	17.3016	0.61657	97.5726
|S_{D21}-|·(1.03)	0.78886	16.7160	0.54662	94.7645
kBG_0·(1.1)	0.70086	16.2665	0.54205	95.6860

Table 14 Impact of varied parameters on DUT X10 extracted Noise Parameters at 30 GHz.

A number of observations can be made from this analysis. We can first say that the approximation made on the ENR introduces a small error on the DUT noise parameters. The error can be considered negligible compared to other sources of error. On the other hand, the error varies with frequency and will therefore be noticeable in the noise parameters as a function of frequency.

We observe also that the effect of 0.2dB (5%) non-linearity on our receiver has a very significant impact on F_{mindB} and R_n. It is difficult to evaluate if our receiver was satisfying the linearity requirement for the noise power level obtained at the output of the DUT. We included this analysis to show that linearity of the receiver should not be just assumed but must be verified. It could not be verified in our case due to the lack of a known test procedure which would verify all possible sources of non-linearity.

The possible discrepancy of ±0.5 MHz between the VNA and the noise figure meter frequency alignment seems sufficient to avoid significant error. Increasing this uncertainty to ±6 MHz as specified by the noise figure meter introduces an error of 0.05 dB on F_{mindB} in our case. We therefore conclude that the frequency alignment procedure introduced with our setup is a good practice to keep for future measurements.

Unlike the other parameters studied here, the error on the DUT S_{D11} introduces a large error on the location of the extracted optimum reflection coefficient. The minimum noise figure (F_{mindB}) and noise resistance (R_n) are also significantly perturbed variation on S_{D11}. Also, the 3% uncertainty on $|S_{D21}|$ and the 10 % uncertainty on the kBG_0 term are both very significant on the uncertainty of F_{mindB} and R_n.

The outcome of our sensitivity analysis reveals that the uncertainty on the minimum noise figure and the noise resistance are severely affected by the uncertainty in kBG_0, S_{D21}, and S_{D11}. The combination of the uncertainty on these three parameters accounts for most of the uncertainty on our measurements. We recall that the approximation of the ENR definition

was not included in the uncertainty analysis. We showed here that this approximation which results in a small underestimation of the minimum noise figure and of the noise resistance. We note as well that if our hypothesis about the receiver non-linearity is true, it could have a significant impact on the noise parameters. The sensitivity analysis also showed that non-linearity would cause underestimation of the minimum noise figure and noise resistance.

7.6 Conclusion

The uncertainty analysis on measured noise parameters at 30 GHz was performed in this chapter. The simulation method was used. The lack of an on-wafer verification standards for on-wafer S-parameter calibration was circumvented by assuming that the worst case uncertainty could be taken as the typical instrument uncertainty. The computed uncertainties for the Cross constellation were ±0.9 dB on F_{mindB}, ±4 Ω on R_n, and $\pm 0.09\angle\pm 9°$ on Γ_{opt}. These uncertainties enclose the variation observed for the noise parameter as a function of frequency and almost includes the results of the independent measurements made at 26 GHz. The error introduced by the approximation for the ENR definition was small considering the error introduced by other parameters. The parameters introducing the largest uncertainty are kBG_0, S_{D21}, and S_{D11}. Of all the parameters, S_{D11} has the most significant impact on the optimum reflection coefficient (Γ_{opt}). Other parameters have only a small impact on Γ_{opt}. This explains the good agreement obtained with Dr. Boudiaf's measurements for Γ_{opt} at 26 GHz. Unfortunately, we cannot conclude the same thing for F_{mindB} and R_n. Although not verified, the hypothesis of non-linearity seems to be the best candidate to conciliate both measurements. The much lower noise figure extracted with the Optimum constellation seems to indicate that this hypothesis may hold true. The uncertainty on Dr. Boudiaf 's measurement should not be neglected either. Finally, future work to further enhance the accuracy of noise parameters at millimeter waves should include a verification of on-wafer S-

parameter accuracy, introduction of a more accurate input block characterization technique, uncertainty analysis with the ORNS, and the establishment of a receiver linearity verification procedure.

8. Conclusion

The main objective of this thesis, to provide noise parameter measurements from 26 to 40 GHz, has been met. An evaluation of the existing measurement techniques was performed. The design of a custom on-wafer probing station was made to provide sufficient source impedance coverage with an automated mechanical tuner. The cold power noise parameter measurement technique was then selected over the hot/cold technique for our study. The cold power technique showed extremely good repeatability at a specific frequency. This was demonstrated with the measurement of the minimum noise figure (F_{mindB}) as a function of device drain current (Ids). These measurements also showed compliance with the general trends of noise models for PHEMTs. We are therefore confident that the optimum biasing current of a device can be accurately determined. The results obtained for one device at one bias point over the 26 to 40 GHz bandwidth were satisfactory. The general trend predicted from noise models were in agreement with our measurements but the spread obtained exhibit the existence of significant errors in our measurements. This behavior is observed as well with the novel on-wafer resistive noise source (ORNS). The spread of the noise parameters over a frequency band is also seen on other measurement systems. Comparison of our measurements with an independent laboratory revealed good agreement on Γ_{opt}, but a difference in F_{mindB} of +0.9dB, and in R_N of +5 Ω was identified at 26 GHz. The same difference is consistently observed for the two devices tested. This indicates that our system provides very good repeatability but may suffer from a significant error.

An uncertainty analysis specific to our measurements at 30 GHz was performed in the hope that the spread and the observed difference with the independent system could be explained.

First, the uncertainty analysis, using a simulation technique, confirmed the importance of accurate S-parameter measurements. A strong relation between Γ_{opt} and measurement of the DUT S_{D11} was shown. In relation to their uncertainty, the sensitivity of S_{D11}, S_{D21} and kBG_0 on the minimum noise figure (F_{mindB}) and noise resistance (R_n) was shown to be equally significant. We recall that an uncertainty of $\pm3\%\angle\pm1°$ on S_{21}, $\pm5\%\angle\pm2°$on S_{11}, and $\pm10\%$ on kBG_0 were used in our analysis. The 10 % uncertainty on the kBG_0 term resulted mainly from the 3-termination calibration. The spread over a frequency band can therefore be attributed to uncertainties present in our test equipment. The difference with the independent system is not as clear. Our ability of find Γ_{opt} with a good accuracy was confirmed by the independent measurements. Unfortunately, a significant discrepancy between R_n and F_{mindB} could be only partially explained with our uncertainty analysis. Our lack of information about the independent measurements limited our analysis to evaluate possible errors, which had not been taken into account. The possible non-linearity of our receiver was identified to be the best hypothesis to explain the difference. Unfortunately, this hypothesis could not be proven nor eliminated. Nevertheless, a lot of the ground work was performed in this thesis to describes the sources of uncertainty and to evaluate their impact in a specific measurement situation.

A more detailed studies concerning the establishment of on-wafer S-parameter accuracy specifications and identification of the best constellation through more sophisticated uncertainty analysis are some examples of work still required. Future work concerning the ORNS is also encouraged. This novel noise source is believed to have the potential for simplifying the test procedure and for making more accurate measurements at millimeter waves where input block characterization is more susceptible to introduce large errors.

Appendix A Transformation Between Representations of Noise in Two-ports

This appendix presents the noise parameters of various representations for noise in two-port networks. Some equations to compute the noise factor from these parameters are also presented. Note that the same symbols are sometimes used to describe different parameters in order to remain consistent with the original definitions.

In most representations, the parameters are defined from two correlated Gaussian random processes to represent the generation of the noise voltage ($e_n(t)$) and current ($i_n(t)$) (Figure 2.2). The other two parameters required to complete the characterization of a two-port are given by the correlation coefficient ($\gamma = \gamma_r + j\gamma_i$) between these two noise sources.

A.1 Π- and T-Matrix Representation

The first representation of noise in two-ports was introduced by Rothe and Dahlke [14] with the Π- and T-Matrix. In this case, the noise generators ($e_n(t)$, $i_n(t)$) are divided in a part not correlated (u_n, i_n) and a part fully correlated (u, i) to the other generator. A correlation admittance (or impedance) is thus defined to establish $e_n(t)=u_n+iZ_{cor}$ and $i_n(t)=i_n+uY_{cor}$. From these, the Π-Matrix parameters R_n, G_n, and Y_{cor} are defined as:

$$R_n = \overline{|u|^2}/4kT_0B,\ G_n = \overline{|i_n|^2}/4kT_0B,\ Y_{cor} = \gamma\sqrt{\frac{\overline{|i|^2}}{\overline{|u|^2}}}. \qquad (A.1)$$

Note that $i_n \neq i_n(t)$ here. For the T-Matrix we have the parameters r_n, g_n, and Z_{cor} defined as:

$$r_n = \overline{|u_n|^2}/4kT_0B,\ g_n = \overline{|i|^2}/4kT_0B,\ Z_{cor} = \gamma\sqrt{\frac{\overline{|u|^2}}{\overline{|i|^2}}}. \qquad (A.2)$$

Note that the noise sourcee of the Π- and T-Matrix augment the represented noise free two-port at its input.

A.2 Wave Representation

The wave representation introduces two uncorrelated wave generators given by [17]:

$$a_n = -\frac{e_n(t) + Z_v i_n(t)}{2\sqrt{\mathrm{Re}(Z_v)}},\ b_n = \frac{e_n(t) - Z_v^* i_n(t)}{2\sqrt{\mathrm{Re}(Z_v)}} \qquad (A.3)$$

where Z_v is a normalization impedance. Note that these sources are connected to the input of a noise-free two-port with two directional couplers and a transmission line having a complex "characteristic impedance" Z_v. Thus, if the scattering matrix of the noise-free two-port is S, we obtain:

$$\begin{bmatrix} b_1 - b_n \\ b_1 \end{bmatrix} = \begin{bmatrix} S_{11} & S_{12} \\ S_{21} & S_{22} \end{bmatrix} \cdot \begin{bmatrix} a_1 + a_n \\ a_2 \end{bmatrix}. \qquad (A.4)$$

A.3 IRE Standard Representation

In 1960 , the IRE introduced a standard representation with more meaningful parameters from which the noise figure of a two port can easily be computed [13]. Before we introduce the representation, we define the equivalent noise resistance (R_n) and the noise conductance (G_n) given by:

$$R_n = \overline{|e_n(t)|^2}/4kT_0B,\ G_n = \overline{|i_n(t)|^2}/4kT_0B \qquad (A.5)$$

where T_0=290K is the standard temperature, B is the bandwidth. Note that R_n and G_n are different from those of (A.1). We also define the correlation admittance $Y_\gamma = G_\gamma + jB_\gamma$ from which the correlated noise current $i_n(t) = (i - i_u) = eY_\gamma$ is defined. Like in Section A.A.1, i and i_u

are a fully corellated and uncorrelated noise current respectively. We further define an equivalent noise conductance for the uncorrelated noise current (i_u) as:

$$G_u = \overline{|i_u)|^2} / 4kT_0B \qquad (A.6)$$

From these definitions, the IRE introduced the optimum source admittance ($Y_0=G_0+jB_0$), and the minimum noise factor (F_0) as [13] :

$$F_0 = 1 + 2R_n(G_\gamma + G_0),\ G_0 = \sqrt{\left(\frac{G_u + R_n G_\gamma^2}{R_n}\right)},\ B_0 = -B_\gamma . \qquad (A.7)$$

The set of noise parameters is therfore given from F_0, R_n, and $Y_0=G_0+jB_0$. The network noise factor (F) is then straigthforward from:

$$F = F_0 + \frac{R_n}{G_s}\left[(G_s - G_0)^2 + (B_{s-} - B_0)^2\right] \qquad (A.8)$$

where $Y_s=G_s+B_s$ is the source reflection coefficient presented to the network. Using the relation of admittance (Y), impedance (Z), and reflection coeficient (Γ), (A.8) can easily be transformed to:

$$F = F_{min} + \frac{R_n}{R_s}\left|\frac{Z_s}{Z_{opt}} - 1\right|^2 \qquad (A.9)$$

where $F_{min}=F_0$, $Z_{opt}=1/Y_0$, $Z_s=1/Y_s=R_s+X_s$. We can also get:

$$F = F_{min} + 4\left(\frac{R_n}{Z_0}\right) \frac{|\ \Gamma_s - \Gamma_{opt}|^2}{(\ 1-|\Gamma_s|^2)\ |1+\Gamma_{opt}|^2} \qquad (A.10)$$

where Z_0 is the characteristic impedance, $\Gamma_s = \left(\frac{Z_s - Z_0}{Z_s + Z_0}\right)$, and $\Gamma_{opt} = \left(\frac{Z_{opt} - Z_0}{Z_{opt} + Z_0}\right)$.

A.4 Invariant Parameters Representation

This representation seeks to determine network noise parameters which are invariant under lossless transformation of the source admittance. The minimum noise factor ($F_{0p}=F_0$) defined in Section A.A.3 is clearly invariant under the lossless aproximation and the optimum admittance $Y_{0p}=Y_0$ transforms like an ordinary admittance. However, R_n transforms in a complicated manner and should be replaced by an invariant constant. It is therefore replaced by the quantity defined by Lange [18] as:

$$N = R_n \operatorname{Re}(Y_0).$$

The invariant noise parameters are given by F_{op}, Y_{op}, *and* N. These parameters are related to the two correlated noise source ($e_n(t)$) ($i_n(t)$) with a correlation coefficient ($\gamma = \gamma_r + j\gamma_i$) by [18]:

$$\begin{aligned} F_{op} &= \frac{\sqrt{\overline{i_n^2 e_n^2}}}{2kT_0B}\left(\sqrt{1-\gamma_i^2}+\gamma_r\right) \\ Y_{op} &= \left|Y_{op}\right|\left(\sqrt{1-\gamma_i^2}+j\gamma_i\right), \left|Y_{op}\right| = \frac{\overline{i_n^2}}{\overline{e_n^2}}, \\ N &= \frac{\sqrt{\left(1-\gamma_i^2\right)\overline{i_n^2 e_n^2}}}{4kT_0B}. \end{aligned} \qquad (A.11)$$

The noise factor of a two-port network written in terms of this representation is given by:

$$F = F_{op} + \frac{N\left|Y_s - Y_{op}\right|^2}{\operatorname{Re}\left(Y_{op}\right)\operatorname{Re}\left(Y_s\right)}. \qquad (A.12)$$

A.5 Correlation Matrix Representation

The correlation matrix representation was introduced in [15] for computer aided noise analysis. The correlation matrix of two correlated noise sources s_1 and s_2 is given by:

$$\mathbf{C} = \frac{1}{2B}\begin{bmatrix} \langle s_1 s_1^* \rangle & \langle s_1 s_2^* \rangle \\ \langle s_2 s_1^* \rangle & \langle s_2 s_2^* \rangle \end{bmatrix} \qquad (A.13)$$

where $\langle s_i s_j^* \rangle = C_{s_i s_j}$ denotes the mean fluctuation product of the signal s_i and the complex conjugate of s_j. The $C_{s_i s_j}$ is equivalent to the self- and cross-power spectral densities. If we apply this representation to the two noise sources connected to the noise free two-port network, we obtain the impedance, admittance, and chain correlation matrix as shown in Figure A.1. These matrices are all representations of noise parameters with two-port network.

	admittance	impedance	chain
equivalent noise circuit	i_1 — noiseless two-port — i_2	u_1 — noiseless two-port — u_2	u, i — noiseless two-port
correlation matrix	$C_Y = \begin{bmatrix} C_{i_1 i_1} & C_{i_1 i_2} \\ C_{i_2 i_1} & C_{i_2 i_2} \end{bmatrix}$	$C_Z = \begin{bmatrix} C_{u_1 u_1} & C_{u_1 u_2} \\ C_{u_2 u_1} & C_{u_2 u_2} \end{bmatrix}$	$C_A = \begin{bmatrix} C_{uu} & C_{ui} \\ C_{iu} & C_{ii} \end{bmatrix}$
electrical matrix	$Y = \begin{bmatrix} Y_{11} & Y_{12} \\ Y_{21} & Y_{22} \end{bmatrix}$	$Z = \begin{bmatrix} Z_{11} & Z_{12} \\ Z_{21} & Z_{22} \end{bmatrix}$	$A = \begin{bmatrix} a_{11} & a_{12} \\ a_{21} & a_{22} \end{bmatrix}$

Figure A.1 Correlation Matrix of Various Representation [15].

Appendix B Noise Factor with the Cold Power Technique

The mathematical formulation for noise figure measurements using the cold power technique is presented in this appendix [2, p.178] [58]. We report the assumptions and equations for the noise figure measurement of a receiver connected to a passive two-port network as shown in Figure B.1.

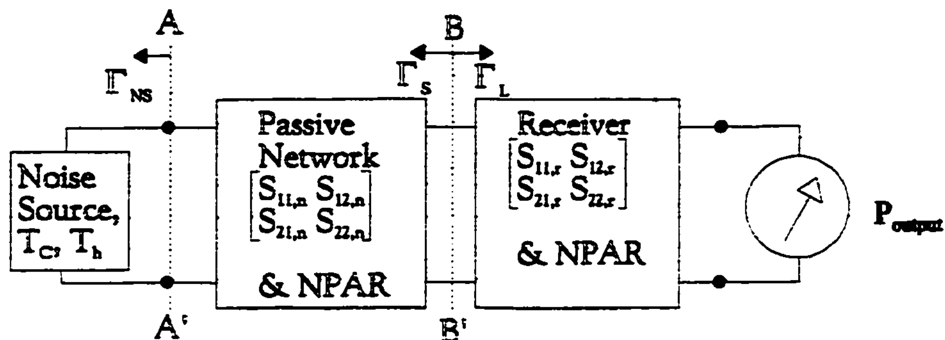

Figure B.1 The noise source, passive two-port and receiver chain.

We first recall that for any noise figure measurement, the receiver is assumed to have a linear characteristic. The assumption is also made that the reflection coefficient of the noise sources (Γ_{NS}) is the same for both hot and cold states. This assumption is not always required but it simplifies the computation of the noise figure [50] [58].

From these two assumptions, we define the kBG_0 in the following discussion. This term is required to compute the noise figure of the receiver for any source impedance. It also eliminates the requirement, in the hot/cold power technique, to measure the noise power associated with a hot noise source. Yet, the kBG_0 is computed from one hot and one cold noise power measurement at a specific source impedance (Γ_S). The measured output noise power (P_{output}) is given by:

$$P_{output} = T_{a,BB'}kBG_{tr} + T_{a,r}kBG_{tr} \qquad \text{(B.1)}$$

where k is Boltzman's constant, B is the measurement bandwidth, $T_{a,r}$ is the added noise temperature of the receiver which is computed from the receiver NPAR and Γ_S, $T_{a,BB'}$ is the available noise temperature at reference plane BB', and G_{tr} is the transducer gain of the receiver. By measuring the output noise power (P_c, P_h) associated with two known available noise temperature ($T_{c,BB'}$, $T_{h,BB'}$) at the input of the receiver, we can compute the difference between the two equations (C.1) and get

$$kBG_{tr} = \frac{P_h - P_c}{T_{h,BB'} - T_{c,BB'}} \tag{B.2}$$

where G_{tr} is given by:

$$G_{tr} = \frac{\left(1 - |\Gamma_S|^2\right)|S_{21,r}|^2\left(1 - |\Gamma_P|^2\right)}{\left|\left(1 - S_{11,r}\Gamma_S\right)\left(1 - S_{22,r}\Gamma_P\right) - S_{12,r}S_{21,r}\Gamma_S\Gamma_P\right|^2} . \tag{B.3}$$

We clearly see from (B.3) that the gain bandwidth constant is a function of the source reflection coefficient (Γ_S) presented to the receiver. If we assume that the receiver is unilateral (i.e.: $S_{12,r}=0$), then we obtain from (B.3)

$$G_{tr} = \left(\frac{1 - |\Gamma_S|^2}{|1 - S_{11,r}\Gamma_S|^2}\right)\left(\frac{|S_{21,r}|^2\left(1 - |\Gamma_P|^2\right)}{|1 - S_{22,r}\Gamma_P|^2}\right) = \left(\frac{1 - |\Gamma_S|^2}{|1 - S_{11,r}\Gamma_S|^2}\right)G_0 \tag{B.4}$$

So, (B.2) becomes:

$$kB\left(\frac{1 - |\Gamma_S|^2}{|1 - S_{11,r}\Gamma_S|^2}\right)G_0 = \frac{P_h - P_c}{T_{h,BB'} - T_{c,BB'}}.$$

This gives us the definition for the kBG_0 term of the receiver as

$$kBG_0 = \frac{P_h - P_c}{T_{h,BB'} - T_{c,BB'}} \left(\frac{\left|1 - S_{11,r}\Gamma_S\right|^2}{1 - \left|\Gamma_S\right|^2} \right). \tag{B.5}$$

In practice, this means that the receiver and the source reflection coefficient must be measured. Also, the available noise power $T_{h,BB'}$ and $T_{C,BB'}$ need to be computed. The network inserted between the noise source (AA') and the receiver (BB') is passive and it is sitting at the room temperature T_{amb}. Its noise parameters can therefore by directly computed from the network electrical parameters [15]. Hence,

$$\begin{aligned} T_{c,BB'} &= T_c G_{av,n} + T_{amb}(1 - G_{av,n}) \\ T_{h,BB'} &= T_h G_{av,n} + T_{amb}(1 - G_{av,n}) \end{aligned} \tag{B.6}$$

where $G_{av,n}$ is the available gain of the passive network. If we replace (B.6) in (C.1) and compute the difference between the two equations, we get:

$$kBG_{av,n}G_{tr} = \frac{P_h - P_c}{T_h - T_c} \tag{B.7}$$

where

$$G_{av,n} = \frac{\left|S_{21,n}\right|^2\left(1 - \left|\Gamma_{NS}\right|^2\right)}{\left(1 - \left|\Gamma_S\right|^2\right)\left|1 - S_{11,n}\Gamma_{NS}\right|^2} \quad \text{with} \quad \Gamma_S = S_{22,n} + \frac{S_{12,n}S_{21,n}\Gamma_{NS}}{1 - S_{11,n}\Gamma_{NS}} \tag{B.8}$$

We therefore obtain from (B.7),(B.8), and (B.4):

$$kB\left(\frac{\left|S_{21,n}\right|^2\left(1 - \left|\Gamma_{NS}\right|^2\right)}{\left(1 - \left|\Gamma_S\right|^2\right)\left|1 - S_{11,n}\Gamma_{NS}\right|^2} \right)\left(\left(\frac{1 - \left|\Gamma_S\right|^2}{\left|1 - S_{11,r}\Gamma_S\right|^2} \right) G_0 \right) = \frac{P_h - P_c}{T_h - T_c} \tag{B.9}$$

from which we extract the kBG_0 term:

$$kBG_0 = \frac{P_h - P_c}{T_h - T_c}\left(\left|1 - S_{11,r}\Gamma_S\right|^2\right)\left(\frac{\left|1 - S_{11,n}\Gamma_{NS}\right|^2}{\left|S_{21,n}\right|^2\left(1 - \left|\Gamma_{NS}\right|^2\right)}\right) \quad \text{(B.10)}$$

This completes the derivation and explanation regarding the kBG_0 term. The calculation of the receiver noise factor from this term is now possible. The definition of noise factor is:

$$F = \frac{N_{a,r} + kT_0BG_{tr}}{kT_0BG_{tr}}. \quad \text{(B.11)}$$

The noise power measured by the receiver of Figure B.1 is given by:

$$P = T_c kBG_{tr} + N_{a,r}. \quad \text{(B.12)}$$

By re-arranging (B.11) and (B.12), we get:

$$F = \frac{P - T_c kBG_{tr} + kT_0BG_{tr}}{kT_0BG_{tr}} = \frac{P}{kT_0BG_{tr}} - \frac{T_c}{T_0} + 1. \quad \text{(B.13)}$$

The final form of the noise factor is obtained by substituting G_{tr} with the receiver kBG_0 terms:

$$F = \frac{P_i}{kT_0BG_0}\left(\frac{\left|1 - S_{11,r}\Gamma_{S_i}\right|^2}{1 - \left|\Gamma_{S_i}\right|^2}\right) - \frac{T_c}{T_0} + 1 \quad \text{(B.14)}$$

where P_i is the cold noise power measurement associated with the source reflection coefficient Γ_{Si}. Hence, after having measured the kBG_0 term, the noise factor at the ith source reflection is computed from the cold power measurement only as expressed by (B.14). From at least four noise factor measurements, the noise parameters of the receiver can be computed.

From a similar derivation, the noise factor of a DUT ($S_{ij,D}$) inserted at reference plane BB' can be obtained and is given by:

$$F = \frac{P_i}{kT_0BG_0}\left(\frac{\left|1 - S_{11,D}\Gamma_{S_i}\right|^2\left|1 - S_{11,r}\Gamma'_{22,Di}\right|^2}{\left(1 - \left|\Gamma_{S_i}\right|^2\right)\left|S_{21,D}\right|^2}\right) - \frac{T_c}{T_0} + 1 \quad \text{(B.15)}$$

where $$S'_{22,n} = S_{22,D} + \frac{S_{12,D}S_{21,D}\Gamma_{Si}}{1 - S_{11,D}\Gamma_{Si}}$$

Appendix C Noise Parameter Extraction Algorithm

The vector formulation for noise parameter extraction proposed by O'Callaghan and Mondal in [44] is presented here. We can formulate the dependence of noise factor of a two-port on the source admittance ($Y_S = G_S + B_S$) as:

$$F = (F_{MIN} - 2R_N G_0) + R_N \frac{G_s^2 + B_s^2}{G_s} - 2R_N B_0 \left(\frac{B_s}{G_s}\right) + \left[R_N\left(G_0^2 + B_0^2\right)\right]\frac{1}{G_s} \qquad \text{(C.1)}$$

where F_{MIN}, = minimum noise figure, $Y_0 = G_0 + B_0$ = optimum source admittance, R_N = noise resistance. We now define the following vector:

$$\begin{aligned} i &= 1 \cdots n \\ \overline{F}_M &= (F_{M1}, F_{M2}, \cdots, F_{Mn},)^T \\ \overline{V}_1 &= (1, 1, \cdots, 1)^T \\ \overline{V}_2 &= \left(\frac{G_{s1}^2 + B_{s1}^2}{G_{s1}}, \frac{G_{s2}^2 + B_{s2}^2}{G_{s2}}, \cdots, \frac{G_{sn}^2 + B_{sn}^2}{G_{sn}}\right) \\ \overline{V}_3 &= \left(\frac{B_{s1}}{G_{s1}}, \frac{B_{s2}}{G_{s2}}, \cdots, \frac{B_{sn}}{G_{sn}}\right) \\ \overline{V}_4 &= \left(\frac{1}{G_{s1}}, \frac{1}{G_{s2}}, \cdots, \frac{1}{G_{sn}}\right) \end{aligned} \qquad \text{(C.2)}$$

where F_{Mi}, G_{si}, B_{si} are the measured noise figure, conductance, and susceptance, respectively, associated with ith measurement set and n is the total number of sets measured. A proper fitting of Eq. (C.1) for all n different data sets is equivalent to the following vector approximation:

$$\overline{F}_M \approx C_1\overline{V}_1 + C_2\overline{V}_2 + C_3\overline{V}_3 + C_4\overline{V}_4 \qquad \text{(C.3)}$$

where $C_1 = (F_{MIN} - 2R_N G_0)$, $C_2 = R_N$, $C_3 = -2R_N B_0$, $C_4 = R_N(G_0^2 + B_0^2)$.

The problem of finding the noise parameters for a best fit of (C.1) can now be reduced to finding the coefficients $C_1 \cdots C_4$ to minimize the error vector F_M and the linear combination of vector V_i. The magnitude of this error vector is given by

$$\varepsilon = \left[\sum_{i=1}^{n} \left(F_{Mi} - F_{fitted\,i} \right)^2 \right]^{1/2} \qquad (C.4)$$

where

$$F_{fitted\,i} = \sum_{j=1}^{4} C_j V_{ji} \qquad i = 1,2,\cdots,n$$

and V_{ij} is the ith component of $\overline{\mathbf{V}}_j$. This problem can be solved with the help of the projection theorem in Hilbert spaces, which states that the magnitude of the error vector is minimal when such a vector is orthogonal to all vectors $\overline{\mathbf{V}}_i$, i.e.,

$$\left\langle \left(F_M - \sum_{j=1}^{4} C_j V_j \right), V_i \right\rangle = 0, \qquad i = 1,\cdots,4 \qquad (C.5)$$

where < > indicates the inner product of two vectors. By using the basic properties of the inner product, (C.5) can be rearranged:

$$\sum_{j=1}^{4} \left\langle \overline{\mathbf{V}}_i, \overline{\mathbf{V}}_j \right\rangle C_j = \left\langle \overline{\mathbf{F}}_M, \overline{\mathbf{V}}_i \right\rangle, \qquad i = 1,\cdots,4. \qquad (C.6)$$

Eq. (C.6) defines a system of linear equations from which values of the C_j's can be found using standard techniques. Finally, the evaluation of linear dependence and orthogonality between the vectors $\overline{\mathbf{V}}_1, \cdots, \overline{\mathbf{V}}_4$ provides a quick means of identifying the admittance loci and a possible ill-conditionned matrix.

Appendix D The 3 Terminations Calibration Technique

The basis of the 3 termination calibration procedure can be explained from the signal flow graph shown in Figure D.1. If termination Γ_s is connected at the input of a 2 port network, then the output reflection coefficient is given by [80]:

$$\Gamma_{out} = S_{22} + \frac{S_{12}S_{21}\Gamma_S}{1 - S_{11}\Gamma_S} \qquad (D.1)$$

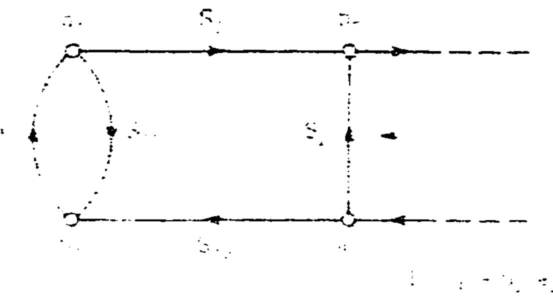

Figure D.1 Signal flow graph of a 2 port network with a termination

For the case where $S_{21}=S_{12}$, we can determine the two-port S-parameters by mesuring the output reflection coefficients Γ_{out1}, Γ_{out2}, Γ_{out3} for three known terminations presenting the reflection coefficient Γ_{S1} , Γ_{S2} , and Γ_{S3} respectivly. Computation of the S-parameters is then made by resolving the set of equations obtained from Eq. (D.1). After resolution, we obtain:

$$S_{11} = \frac{-(-g1g31g21g2 + g1g31g21g3 + g1g11g2g31 - g1g11g21g3 + g11g3g21g2 - g11g3g2g31)}{(-g1g11g31 + g1g11g21 + g2g21g31 - g21g3g31 + g11g3g31 - g11g21g2)},$$

$$S_{22} = \frac{-(-g2g31 + g11g2 - g11g3 + g21g3 + g1g31 - g1g21)}{(-g1g11g31 + g1g11g21 + g2g21g31 - g21g3g31 + g11g3g31 - g11g21g2)},$$

$$
S_{21}S_{12} = \frac{\left(\begin{array}{c}
-\mathrm{g1g31g21g21g2g2} + \mathrm{g1g21g21g2g2g11} - \mathrm{g1g11g11g2g2g21} - \mathrm{g1g1g11g11g2g31} \\
+\mathrm{g1g1g11g11g2g21} + \mathrm{g1g11g11g2g2g31} + \mathrm{g1g1g11g2g31g31} + \mathrm{g11g11g3g3g2g31} \\
-\mathrm{g3g2g2g21g21g11} + \mathrm{g1g31g31g21g2g2} + \mathrm{g11g3g2g2g31g31} - \mathrm{g11g11g3g2g2g31} \\
+\mathrm{g3g3g31g31g1g11} - \mathrm{g1g1g21g21g2g11} - \mathrm{g11g11g3g3g21g2} + \mathrm{g11g3g3g21g21g2} \\
-\mathrm{g3g31g31g1g1g11} + \mathrm{g3g3g31g31g2g21} + \mathrm{g3g2g2g21g21g31} + \mathrm{g3g1g1g11g11g31} \\
+\mathrm{g1g11g11g21g3g3} - \mathrm{g1g11g21g21g3g3} - \mathrm{g3g3g31g31g2g11} - \mathrm{g3g3g31g31g1g21} \\
-\mathrm{g3g1g1g11g11g21} - \mathrm{g3g31g31g2g2g21} - \mathrm{g1g11g11g31g3g3} - \mathrm{g2g21g21g31g3g3} \\
+\mathrm{g1g1g11g21g21g3} + \mathrm{g11g11g3g21g2g2} - \mathrm{g1g1g31g31g21g2} + \mathrm{g1g1g31g21g21g2} \\
+\mathrm{g1g31g21g21g3g3} + \mathrm{g1g1g31g31g21g3} - \mathrm{g1g1g31g21g21g3} - \mathrm{g1g11g2g2g31g31}
\end{array}\right)}{(-\mathrm{g1g11g31} + \mathrm{g1g11g21} + \mathrm{g2g21g31} - \mathrm{g21g3g31} + \mathrm{g11g3g31} - \mathrm{g11g21g2})^2}
$$

(8.2)

where g11 $=\Gamma_{S1}$, g21 $=\Gamma_{S2}$, g31 $=\Gamma_{S3}$, g1 $=\Gamma_{out1}$, g2 $=\Gamma_{out2}$, g3 $=\Gamma_{out3}$.

Appendix E Gain and Mismatch Equations

The evaluation of power transfer in mismatched systems can be done through the proper evaluation of Mason's rule of the signal flow graph representing the system of interest. We present the power transfer equation of a two-port network connected to a source and load as shown in Figure E.1[81]. The reflection coefficients are defined as Γ_g, Γ_1, Γ_2, Γ_L, and S is a 2x2 matrix representing the S-parameters between reference planes 1 and 2. P_{1d} and P_{2d} are the net power delivered to the right of plane 1 and 2. Z_M and Z_N are the characteristic line impedances, which are not necessarily identical. Γ_1 and Γ_2 are related to the matrix S, Γ_L and Γ_g in the in the same manner as expressed by Eq (D.1). The four equations of interest with regards to power transfer are the mismatch factors M and N, the efficiency η, and the ratio of the available power α [81]:

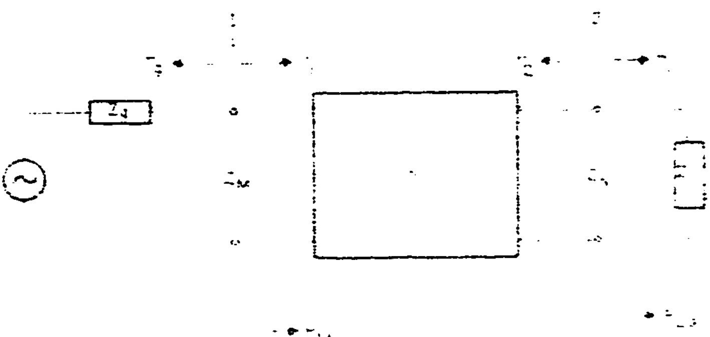

Figure E.1: Two-ports network.

$$M \equiv \frac{\left(1-|\Gamma_g|^2\right)\left(1-|\Gamma_1|^2\right)}{|1-\Gamma_g\Gamma_1|^2} \qquad (E.1)$$

$$N \equiv \frac{\left(1-|\Gamma_L|^2\right)\left(1-|\Gamma_2|^2\right)}{|1-\Gamma_L\Gamma_2|^2} \qquad (E.2)$$

$$\eta = \frac{P_{2d}}{P_{1d}} = \frac{\left(Z_M/Z_N\right)|S_{21}|^2\left(1-|\Gamma_L|^2\right)}{\left(1-|\Gamma_1|^2\right)|1-S_{22}\Gamma_L|^2} \tag{E.3}$$

$$\alpha = \frac{P_{2a}}{P_{1a}} = \frac{M\eta}{N} = \frac{\left(Z_M/Z_N\right)|S_{21}|^2\left(1-|\Gamma_g|^2\right)}{\left(1-|\Gamma_2|^2\right)|1-S_{11}\Gamma_g|^2} \tag{E.4}$$

Both η and α measure the lossiness of the two-port S in that if S is lossless, $\eta = 1 = \alpha$. As such, α will turn out to be a direct measure of how much noise the two-port will contribute to the output. From the above equation, we can evaluate the transfer of noise power in any two-port system having known S-parameters.

In the special case where a test fixture is connected to the tuner, the insertion loss of the test fixture as a function of the tuner reflection coefficient (Γ_t) is given by [82] :

$$PowerLoss = \frac{|1-\Gamma_t * S_{22}|^2 * (1-|\Gamma_1|^2)}{|S_{21}|^2 * \left(1-|\Gamma_t|^2\right)} \text{ and } \Gamma_1 = S_{11} + \frac{S_{12} * S_{21} * \Gamma_t}{1-\Gamma_t S_{22}} \tag{E.5}$$

where S_{ij} are the S-Parameters of the fixture and Γ_t is the reflection coefficient of the tuner.

Appendix F Collection of Pictures

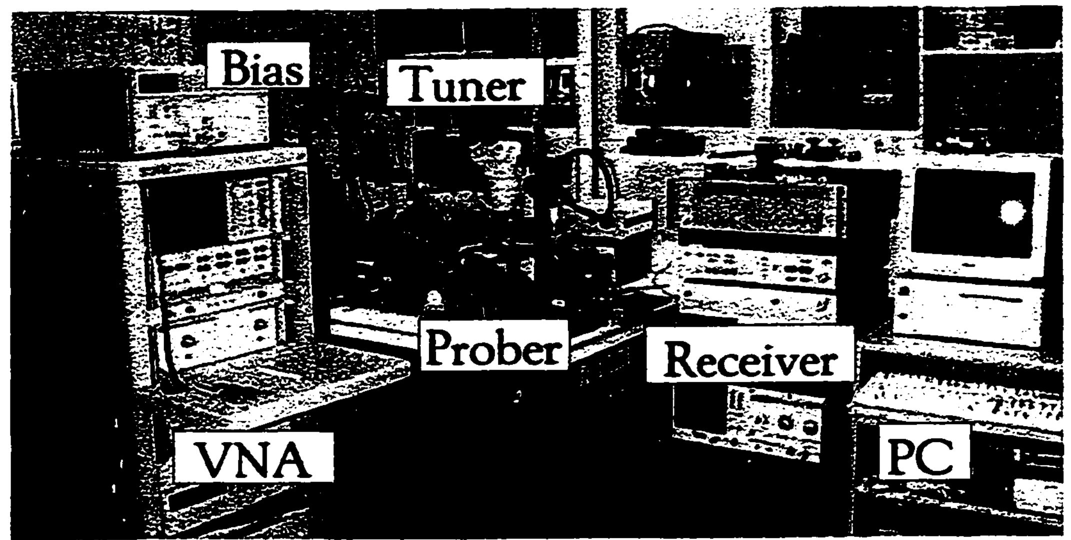

Figure F.1 Complete Measurement System

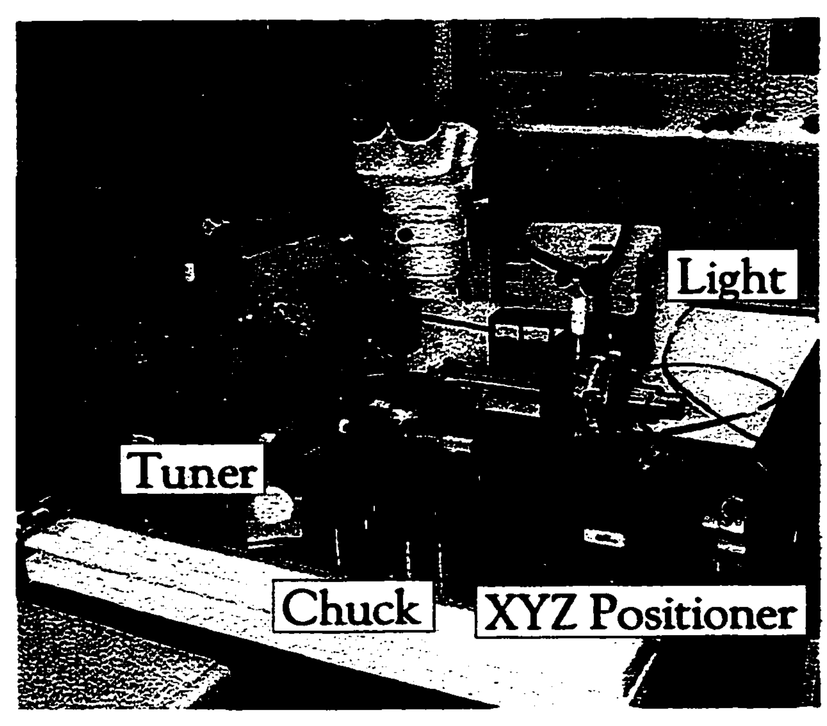

Figure F.2 Custom On-wafer Probing Station

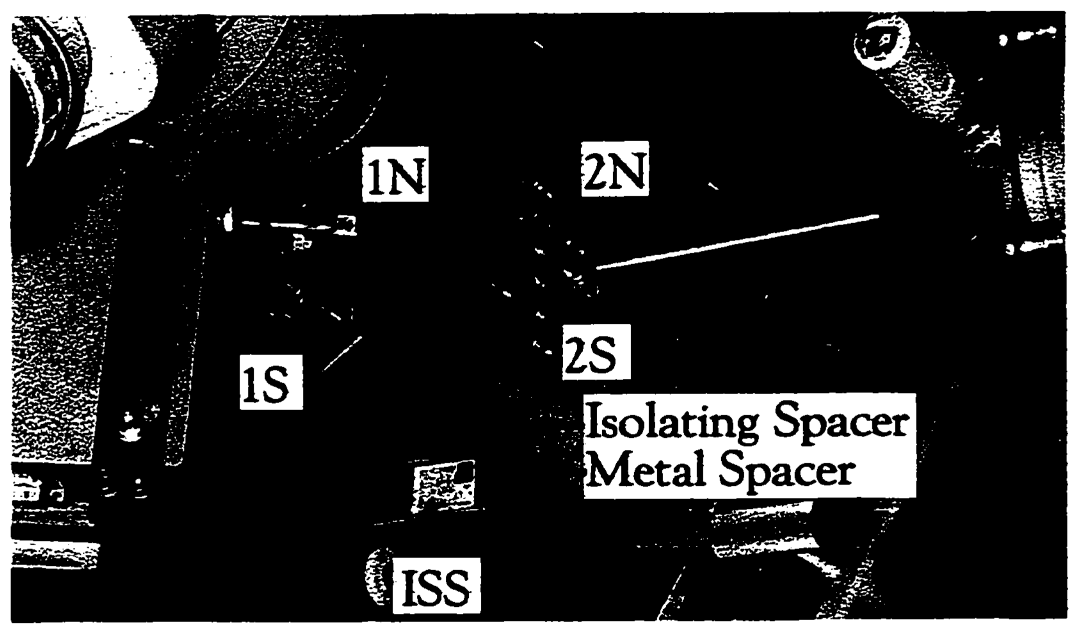

Figure F.3 Closer View of the Chuck

Figure F.4 From left to right: noise source (HP346C), two bias T, LNA, bandpass filter, double balanced mixer.

Bibliography

1 A. Van Der Ziel, "Noise in Solid-State Devices and Lasers", *Proc. IEEE*, vol. 58, pp.1178-1206, Aug. 1970. Also in Madhu S. Gupta, Electrical Noise: Fundamentals & Sources, IEEE Press, pp. 237-265, 1977.

2 M. Tutt, Low and High Frequency Noise Properties of Heterojunction Transistors, Doctoral Thesis, University of Michigan, 1994.

3 R. Pucel, H. A. Haus, and H. Statz, "Signal and Noise Properties of Gallium Arsenide Microwave Field-Effect Transistors," *Advances in Electronics and Electron Physiscs*, Academic Press, vol. 38, pp. 195-235, 1975.

4 Y. Ando, and T. Itoh, "DC, Small-Signal, and Noise Modeling for Two-Dimesional Electron GaAs Field-Effect Transistors Based on Accurate Charge-Control Characteristics", *IEEE trans. on Electron Devices*, vol. 37, no. 1, pp.67-78, Jan. 1990.

5 M. Schwartz, Information Transmission, Modulation, and Noise, 2nd edition, New York, McGraw-Hill, 1970.

6 T. T. Ha, Digital Satellite Communications, Mc Graw Hill, 1986.

7 J. S. Bendat, A. G. Piersol, Engineering Applications of Correlation and Spectral Analysis, John Wiley & Sons, Inc. 1980, pp. 33-35.

8 R. E. Collin, Foundations for Microwave Engineering, 2nd edition, McGraw-Hill, 1992.

9 J. R. Ragazzine, "Noise and Random Processes", *Proc. IRE*, vol. 50, pp.1146-1151, May 1962. Also in Madhu S. Gupta, Electrical Noise: Fundamentals & Sources, IEEE Press, pp. 25-30, 1977.

10 Hewlett Packard Application Note 57-1, Fundamentals of RF and Microwave Noise Figure Measurements, 5952-8255, July 1983.

11 Hewlett Packard Application Note, Noise Figure measurements: Principles and Applications, 5952-8266.

12 R. Goyal, " Monolithic Microwave Integrated Circuits Technology," Artech House, Inc., 1989, p.84.

13 IRE Subcommitee 7.9 on Noise, "Representation of Noise in Linear Twoports", *Proc. IRE*, vol. 48, pp. 69-74, Jan. 1960. Also in H. Fukui, "Low-noise Microwave Transistors & Amplifiers," IEEE Press, 1981, pp. 41-48.

14 H. Rothe and W. Dahlke, "Theory of Noisy Fourpoles," *Proc. IRE*, vol. 44, pp.811-818, June 1956. Also in H. Fukui, "Low-noise Microwave Transistors & Amplifiers," IEEE Press, 1981, pp.10-17.

15 H. Hillbrand and P. H. Russer, "An Efficient Method for Computer Aided Noise Analysis of Linear Amplifier Networks," *IEEE trans. on Circuits and Systems*, vol. CAS-23, no. 4, pp. 235-238, April 1976.

16 M. Pospieszalski, "On the Measurment of Noise Parameters of Microwave Two-ports," *IEEE trans. on Microwave Theory and Techniques*, vol. MTT-34, no. 4, pp.456-458, April 1986.

17 P. Penfield, "Wave Representation of Amplifier Noise", *IRE trans. on Circuit Theory*, vol. CT-9, pp. 84-86, March 1962. Also in H. Fukui, "Low-noise Microwave Transistors & Amplifiers," IEEE Press, 1981, pp.26-27.

18 J. Lange, "Noise Characterization of Linear Two-ports in Terms of Invariant Parameters," *IEEE J. Solid-State Circuits*, vol. SC-2, pp. 37-40, June 1967.

19 P. H. Ladbrooke, "MMIC Design, GaAs FETs and HEMTs", Artech House, Inc. 1989, p. 189.
20 W.-H. L. Lo, Noise Parameter Measurements of Pseudomorphic High Electron Mobility Transistors at 18-26 GHz, Master Engineering Thesis, McMaster University 1991, pp.148-157.
21 R. Plana, L. Escotte, O. Llopis, H. Amine, T. Parra, M. Gayral, J. Graffeuil, "Noise in AlGaAs/InGaAs/GaAs Pseudomorphic HEMT's from 10 Hz to 18 GHz," *IEEE trans. on Electron Devices*, vol. 40, no. 5, pp. 852-858, May 1993.
22 M. Feng, D. Scherrer, J. Kruse, P.J. Apostolakis, and J. R. Middleton, "Temperature Dependence Study of Two-Dimensional Electron Gas Effect on the Noise Performance of High Frequency Field Effect Transistors," *IEEE Electron Device Letters*, vol. 16, no. 4, pp. 139-141, April 1995.
23 R. Dingle, H. L. Stomer, A. G. Gossard, and W. Weigmann, "Electron Mobility's in Modulated-Doped Semiconductor Heterojunction Superlattices," *Appl. Phys. Lett*, vol. 33, p.1088, 1978.
24 K. L. Tan, R. M. Dia, D. C. Streit, T. Lin, T. Q. Trinh, A. C. Han, P.H. Liu, P.-M. D. Chow, and H.C. Yen, "94 GHz 0.1 um T-gate Low-noise Pseudomorphic InGaAs HEMT's," *IEEE Electron Device Lett.*, vol. 11, pp. 585-587, Dec 1990.
25 T. Brookes, "The Noise Properties of High Electron Mobility Transistors," *IEEE trans. on Electron devices*, pp. 52-57, Jan. 1986.
26 A. Van der Zeil, "Thermal Noise in Field Effect Transistors," *Proc. IRE*, vol. 50, pp. 1808-1812, 1962.
27 A. Cappy, A. Vanoverschelde, M. Schortgen, C. Versnaeyen, and G. Salmer, "Noise modeling in submicrometer-gate two-dimensional electron-gas field effect transistors," *IEEE trans. on Electron Devices*. vol. ED 32, no 12, pp.2787-2795, 1985.
28 K. Joshin, S. Asai, Y. Hirachi, M. Abe, "Experimental and Theoretical Noise Analysis of Microwave HEMT's," *IEEE trans. on Electron Devices*, vol. 36, no. 10, pp. 2274-2279, Oct. 1989.
29 M. W. Pospieszalski, "Modeling of Noise Parameters of MESFET's and MODFET's and Their Frequency and Temperature Dependence," IEEE trans. on MTT, vol. 37, no. 9, pp.1340-1350, Sept. 1989.
30 M. W. Pospieszalski, "FET Noise Model and On-Wafer Measurement of Noise Parameters," Digest of IEEE Microwave Theory and Techniques Symposium, pp. 1117-1120, 1991.
31 Y. Ando and T. Itoh, "DC, Small-Signal, and Noise Modeling for Two-Dimensional Electron Gas Field-Effect Transistors Based on Accurate Charge-Control Characteristics," *IEEE trans. on Electron Devices*, vol. 37, no. 1, pp. 67-78, Jan 1990.
32 M.T. Hickson, P. Gardner, and D.K. Paul, "A Semidistributed HEMT Model for Accurate Fitting and Extrapolation of S-Parameters and Noise Parameters," *IEEE trans. on Microwave Theory and Techniques*, vol. MTT-40, no. 8, pp. 1709-1712, August 1992.
33 A. F. M. Anwar and Kuo-Wei Liu, "Noise Properties of AlGaAs/GaAs MODFET's," *IEEE trans. on Electron Devices*, vol. 40, no. 6, pp. 1174-1176, June 1993.
34 A. F. M. Anwar and Kuo-Wei Liu, "A Noise Model for High Electron Mobility Transistors", *IEEE trans. on Electron Devices*, vol. 41, no. 11, pp. 2087-2092, November 1994.
35 T. Felgentreff, G. Olbrich, P. Russer, "Noise Parameter Modeling of HEMTs with Resistor Temperature Noise Sources," IEEE MTT-S Digest 1994, p. 853-856.
36 L. Pradell, A. Comeron, A. Ramirez, "A General Analysis of Errors in Noise Measurement Systems," pp. 924-929, Sept 1988.

37 Hessen-Schmidt B., "State of the art in solid state noise sources enhances measurement accuracy," *Microwave Journal*, pp.123-129, April 1991.
38 Hewlett Packard Application Note 57-2, Noise Figure Measurement Accuracy, 5952-3706, November 1988.
39 R. Mieirer and D. Dubouil, Private Communication.
40 IRE Standard, 59 IRE 20. S1 "IRE Standards on Methods of Measuring Noise in Linear Twoports", 1959," *Proc. IRE*, vol. 48, pp. 60-68, Jan. 1960. Also in h. Fukui, "Low-noise microwave transistors & amplifiers," IEEE Press, 1981, p.32.
41 R. Q. Lane, "The Determination of Device Noise Parameters," *Proc. IEEE*, vol. 57, pp. 1461-1462, August 1969. Also in H. Fukui, "Low-noise Microwave Transistors & Amplifiers," IEEE Press, 1981, pp. 47-48.
42 M. Sannino, "On the Determination of Device Noise and Gain Parameters", Proc. IEEE, vol. 67, pp. 1364-1366, Sept 1979. Also in Fukui H, "Low-noise Microwave Transistors & Amplifiers," IEEE Press, 1981, pp. 52-53.
43 L. Escotte, "Evaluation of Noise Parameters Extraction Method," *IEEE trans. on Microwaves Theory and Techniques*, vol MTT-41, no 3, pp. 382-387, March 1993.
44 O'callaghan and Mondal, "A Vector Approach for Noise Parameter Fitting and Selection of Source Admittance," *IEEE trans on Microwave Theory and Techniques*, vol. 39, no 8, pp. 1376-1382, August 1991.
45 M. Mitama and H. Katoh, "An Improved Computational Method for Noise Parameter Measurement", *IEEE trans. on Microwave Theory and Techniques*, vol. MTT-27, pp. 612-615., June 1979. Also in H. Fukui, "Low-noise microwave transistors & amplifiers", IEEE Press, 1981, pp. 54-57.
46 G. Vasilescu, G. Alquie, and M. Krim, "Exact Computation of Two-port Noise Parameter", *Electron Lett.*, vol. 25, no.4, Feb 16, 1989.
47 M. Boudiaf and M. Laporte, "Evaluation des methode d'extraction des parameters de bruit", *IEEE French Chapter Meeting*, Carcassonne, Nov. 22-23, 1990.
48 L. Chusseau, M. Parisot, and N. Jousseaume, "Mesure automatique des parameters de bruit des MESFET hyperfrequence", *Annales des Telecommunications*, vol. 43, no 5-6, 1988.
49 M. S. Gupta, "Determination of the Noise Parameters of a Linear 2-port", *Electron. Lett.*, vol. , no. 17, Aug. 20, 1970.
50 A. C. Davidson, B. W. Leake E. Strid, "Accuracy Improvements in Microwave Noise Parameter Measurements", *IEEE trans. on Microwaves Theory and Techniques*, vol. 37, no. 12, December 1989, 1973-1977.
51 B. Hughes and P. Tasker, "Improvements to On-wafer Noise Parameter Measurement." *36th ARFTG*, pp.16-25, Fall 1990.
52 R. Q. Lane, "A Microwave Noise and Gain Parameter Test Set", *IEEE Int. Solid-State Circuits Conf.*, pp. 172, 173 and 274, 1978,. Also in H. Fukui, "Low-noise microwave transistors & amplifiers, " IEEE Press, 1981, pp. 49-51.
53 G. Martines and M. Sannino, "Simultaneous Determination of Transistor Noise, Gain, and Scattering Parameters for Amplifier Design Through Noise Figure Measurement Only", *IEEE trans. on Instrumentation and Measurement*, vol. IM-34, no. 1, March 1985.
54 A. Fraser, E. Strid, B. Leake, T. Burcham, "Repeatability and Verification of On-wafer Noise Parameter Measurement", *Microwave Journal*, pp. 172-176, November 1988.
55 G. R. Simpson and W. E. Pastori, "Using a Load Tuner to Improve the Accuracy of Noise Characterization", *33 rd Conferrence of the Automatic RF Techniques Group*, June 1989.

56 A. Caddemi, G. Martines and M Sannino, "Automatic Characterization and Modeling of Microwave Low-Noise HEMT's", *IEEE trans. on Instrumenttation and Measurmement*, vol. 41, no. 6, pp. 946-950, December 1992.
57 G. Martines and M Sannino, "The Determination of the Noise, Gain, and Scattering Parameters of Microwave Transistors (HEMT's) using Only an Automatic Noise Figure Test-Set", *IEEE trans. on Microwaves Theory and Techniques*, vol. 42, no. 7, pp. 1105-1113, July 1994.
58 Vaheh Adamian, Arthur Uhlir, "A Novel Procedure for Receiver Noise Characterisation," *IEEE trans on Instrumentation and Measurement*, pp. 181-182, June 1973.
59 R. Meierer and C. Tsironis, "An On-wafer Noise Parameter Measurement Technique with Automatic Receiver Calibration", *Microwave Journal*, pp. 22-37, March 1985.
60 E. Strid, "Measurement of Losses in Noise Matching Networks," *IEEE trans. on Microwave Theory and Techniques*, vol. MTT-29, pp.247-252, March 1981.
61 Student Guide for Basic Network Measurements Using the HP8510A Network Analyser System, HP Course Number HP 8510A+24D, Edition 2.0, December 1986.
62 Workshop Notes: "Making Accurate On-wafer Measurement", Workshop given at the Microwave Theory and Techniques Conference, San Fransisco, June 1996
63 R. Fenton, "Noise Parameter Data Comparaison While Varying the On-wafer S-parameter Calibration Technique," *36th ARFTG*, Fall 1990.
64 Brian Hughes and Paul Tasker, "Improvements to On-wafer Noise Parameter Measurements", *36th ARFTG Conference Digest*, p. 16-25, Fall 1990
65 Cascade Microtech specifications on their impedance standard substrate Family, ISSFAM-0495.
66 Chapman and Hall, Thin film microelectronics, Edited by L.Holland, pp. 6-17, 1967.
67 Tuner Control Software for Windows Manual, Revision 1.05, August 1995, Focus Microwaves Inc., 277 Lakeshore Road, Pointe-Claire, Québec, Canada, H9S 4L2.
68 L. P. Dunleavy, "A Ka-Band on-wafer S-parameters & N.F. measurement system", *34 th ARFTG conf. Digest*, pp. 127-137.
69 Hughes and Tasker, "Improvements to On-wafer Noise Parameters Measurements", *36th ARFTG*, p.16-25, Fall 1990.
70 Focus Microwaves Inc. Application Note 1-90 "Noise Measurement Using the Computer Controlled Microwave Tuner (CCMT) system," 277 Lakeshore Road, Pointe-Claire, Que, H9S 4L2, 8 p.
71 Operating Manual of the HP8970B Noise Figure Meter Including the HP8970S/T Noise Figure Measurement System, Hewlett Packard, June 1988.
72 E. C. Valk, D. Routledge, J. F. Vaneldik, and T. L. Landeckeer, "Microwave Noise Measurement Errors Caused by Frequency Discrepencies and Nonzero Bandwidth," *IEEE trans. on Intrumentation and Measurment*, vol. 42, no.5, pp. 983-989, December 1993.
73 Hewlett Packard, "Vector Measurments of High Frequency Networks", Seminar notes.
74 Hewlett Packard Application Note 8510 5A.
75 Hewlett Packard Product Note 8970B/S-2 "Applications and Operating of the HP8970B Noise Figure Meter and HP8970S Microwave Noise Figure Measurement System", 5954-8896, August 1987.
76 R. Pucel, D. Massé, C. Krum, "Noise performance of Gallium Arsenide Field-Effect Transistos", *IEEE J. Solid-State Circuits*, vol.-SC-11, pp.243-255, April 1976. Also in H. Fukui "Low-Noise Microwave Transistor & Amplifiers," IEEE Press 1981.

77 F.-I. Buchholz, W. Kessel, and F. Melchert, "Noise Power Measurements and Measurement Uncertainties", *IEEE trans. on Instrumentation and Measurement*, vol. 41, no. 4, August 1992, pp. 476-481.
78 Operation Manual, HP 8970B Noise Figure Meter Including the HP8970S/T Noise Figure Measurement System, Hewlett Packard, June 1988, Part No. 08970-90033.
79 M. W. Pospieszalski and W. Wiatr, "Comments on "Design of Microwave GaAs MESFET's for Broad-Band, Low-Noise Amplifier," *IEEE trans. on Microwave Theory and Techniques*, vol. MTT-34, no. 1, p.194, Jan. 1986.
80 Gonzalez, Microwave Transistor Amplifiers, Analysis and Design, Prentice-Hall, 1984, p. 85.
81 C. K. S. Miller, W. C. Daywitt, and M. G. Arthur, "Noise Standards, Measurements, and Receiver Noise Definitions", *Proc. IEEE*, vol. 55, pp.865-877, June 1967. Also in Madhu S. Gupta, Electrical Noise: Fundamentals & Sources, IEEE Press 1977, pp. 297-309.
82 Focus Microwaves Inc. Application Note 18 "Accuracy and Verification of Load Pull Measurements," 277 Lakeshore Road, Pointe-Claire, Que, H9S 4L2, 12 p, Eq. (4).

IMAGE EVALUATION TEST TARGET (QA-3)

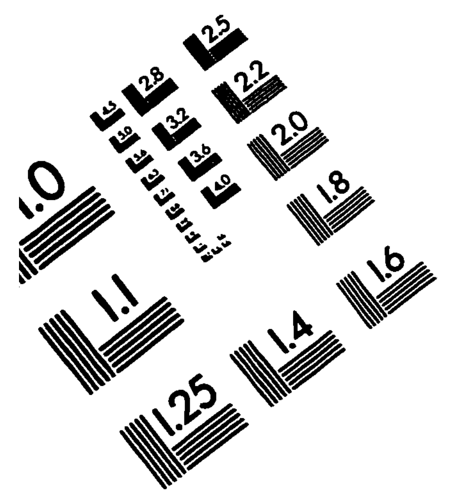

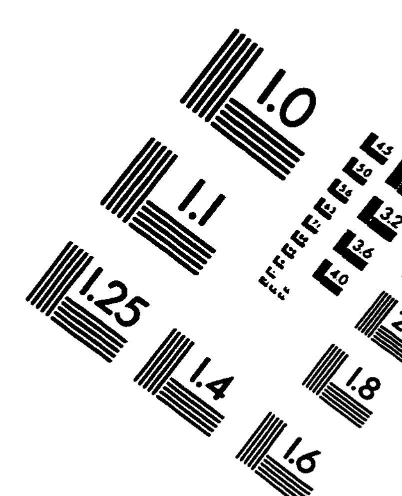

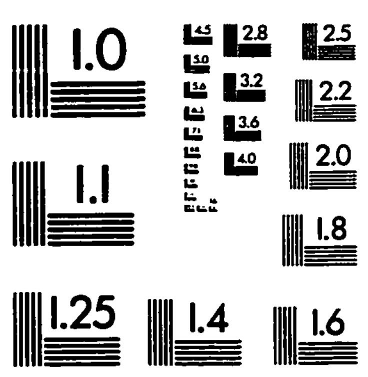

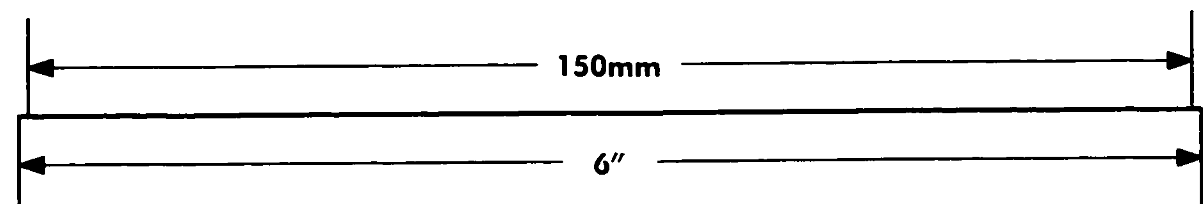

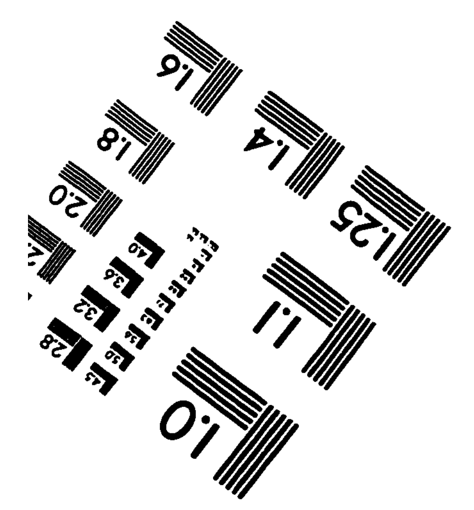

© 1993, Applied Image, Inc., All Rights Reserved